

Probing the hyperfine structure of Fe-based water-gas shift catalysts

Ariëns, M.I.

DOI

[10.4233/uuid:9a32a2ae-0ba7-4686-87df-24cb8be66133](https://doi.org/10.4233/uuid:9a32a2ae-0ba7-4686-87df-24cb8be66133)

Publication date

2023

Document Version

Final published version

Citation (APA)

Ariëns, M. I. (2023). *Probing the hyperfine structure of Fe-based water-gas shift catalysts*.
<https://doi.org/10.4233/uuid:9a32a2ae-0ba7-4686-87df-24cb8be66133>

Important note

To cite this publication, please use the final published version (if applicable).
Please check the document version above.

Copyright

Other than for strictly personal use, it is not permitted to download, forward or distribute the text or part of it, without the consent of the author(s) and/or copyright holder(s), unless the work is under an open content license such as Creative Commons.

Takedown policy

Please contact us and provide details if you believe this document breaches copyrights.
We will remove access to the work immediately and investigate your claim.

Probing the hyperfine structure of Fe-based water-gas shift catalysts

Proefschrift

ter verkrijging van de graad van doctor aan de Technische Universiteit Delft,
op gezag van de Rector Magnificus, prof. dr. ir. T.H.J.J. van der Hagen,
voorzitter van het College voor Promoties,
in het openbaar te verdedigen op vrijdag 27 januari 2023 om 10:00 uur

door

Maxim Ismaële ARIËNS

Master of Science in Chemistry,
Vrije Universiteit Amsterdam, Nederland
geboren te Utrecht, Nederland

Dit proefschrift is goedgekeurd door de promotoren.

Promotor: prof. dr. E.H. Brück

Promotor: prof. dr. ir. E.J.M. Hensen

Copromotor: dr. A.I. Dugulan

Samenstelling promotiecommissie:

Rector Magnificus voorzitter

Prof. dr. E.H. Brück Technische Universiteit Delft, NL

Prof. dr. ir. E.J.M. Hensen Technische Universiteit Eindhoven, NL

Dr. A.I. Dugulan Technische Universiteit Delft, NL

Onafhankelijke leden:

Dr. S. Beaumont Durham University, UK

Prof. dr. P.P. Pescarmona Rijksuniversiteit Groningen, NL

Prof. dr. ir. A. Urakawa Technische Universiteit Delft, NL

Prof. dr. E.A. Pidko Technische Universiteit Delft, NL

Overig lid:

Dr. L.G.A. van de Water Johnson Matthey, UK

This research was partially funded by the Dutch Research Council (NWO) via the research programme LIFT (project number 731.015.419), and partially funded by Johnson Matthey.

Printed by: Gildeprint, Enschede, The Netherlands.

Cover: Gildeprint.

Keywords: Water-gas shift, Fe-based catalysts, industrially relevant conditions, doped magnetite, (*in situ*) Mössbauer spectroscopy, (NAP)-XPS

Copyright © 2023 by M.I. Ariëns

ISBN: 978-94-6419-713-6

An electronic version of this thesis is available at:

<http://repository.tudelft.nl/>.

*Equipped with his five senses, man explores the universe around him and calls
the adventure science*

Edwin Hubble

Contents

Chapter 1: Introduction	7
Chapter 2: Chromium doping	23
Chapter 3: Copper doping	59
Chapter 4: Alternative dopants	91
Chapter 5: <i>In situ</i> Mössbauer spectroscopy	125
Chapter 6: Summary & Samenvatting	153
Acknowledgements	167
List of publications	171
Curriculum Vitae	173

1

INTRODUCTION

1.1 CATALYSIS

Catalysis is essential to ensure our current standard of living. The synthesis of fertilisers ¹, polymers ², commodity chemicals ^{1,3,4}, gas to liquid fuels ⁵, and foodstuffs like hydrogenated vegetable oils ⁶ are examples of products obtained by catalysed processes. Probably the most well-known example of a catalyst to the public is the three-way catalytic converter, which facilitates the removal of harmful CO, NO_x, and unburned hydrocarbons from the exhaust gases of internal combustion engines ⁷. Also, the petroleum refining industry relies heavily on catalysed processes. The low molecular weight hydrocarbon yield of crude oil is significantly increased by cracking processes ⁸, while contaminants like sulphur are removed from transportation fuels by hydrodesulfurisation ⁹. Many other processes in the chemical industry, such as base chemicals and fine chemicals including medicine, often hinge on the use of one or more catalytic transformations.

A catalyst facilitates the chemical reaction by lowering its activation energy without being consumed itself in the process. The thermodynamic equilibrium

of the reaction is not affected by the catalyst¹⁰. Catalysis can be divided into three categories: (i) heterogeneous catalysis, where the catalyst exists in a different phase as the reactants and products. Usually, the catalyst is a solid and reactants are in the liquid or gas phase. Most industrial chemical processes use heterogeneous catalysts because of the ease of separation; (ii) Homogeneous catalysis, where the catalyst exists in the same phase as the reactants and products, usually in the liquid phase; (iii) Bio-catalysis, where enzymes are used as catalysts. The elementary steps of a heterogeneously catalysed surface-reaction are shown in Figure 1: (1) adsorption, where the reactants adsorb to the catalysts surface, (2) surface reaction, and finally (3) desorption, where the product is released from the surface and the catalyst remains for a subsequent cycle. It should be noted that these elementary steps exclude the diffusion of reactants and products in and out of a shaped catalyst, which is an important step in industrial catalysis. As is illustrated in Figure 1, the activation energy of the surface reaction is lower compared to the uncatalysed reaction.

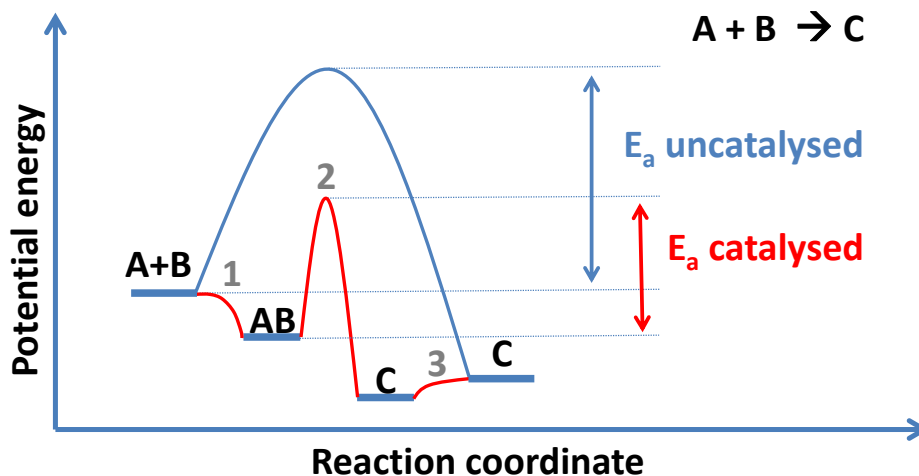
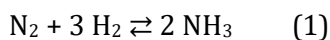


Figure 1. Potential energy scheme of a heterogeneously catalysed reaction of substrates A and B to product C.

One of the most important innovations in the chemical industry in the 20th century is the Haber-Bosch process, where nitrogen and hydrogen gas are combined to ammonia (1)^{1,11}.

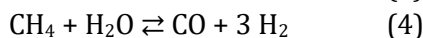
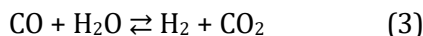


Ammonia derivatives such as nitrates and urea can be used as fertiliser ^{1,10,12}. Before the availability of synthetic nitrogen fertilisers, nitrates were mined in the form of saltpetre. When these natural resources ran out at the turn of the 19th century, alternative resources were in high demand to prevent a major famine, which would result from a lack of available nitrogen-based fertilisers ^{1,10}. The availability of synthetic nitrates by the Haber-Bosch process not only solved this problem, it also facilitated global population growth. It has been estimated that, by 2008, nearly half of the world's population was fed by crops grown with nitrogen-based fertilisers ¹². This means that from a statistical point of view, approximately every other person reading this text owes their existence to the Haber-Bosch process. The immense scale at which ammonia is produced today requires an energy consumption responsible for 1-2% of global CO₂ emissions ¹³. Considering that the Haber-Bosch process is only one of many catalytic processes, the impact of catalysis on the world's economy is evident. Approximately 80-90% of chemical processes rely on catalysis, resulting in an estimated impact on the global gross domestic product of 30-40% ¹⁰.

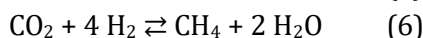
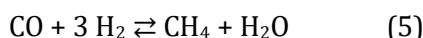
1.2 HYDROGEN GAS AND THE WATER-GAS SHIFT REACTION

Hydrogen is required in a 3:1 ratio to nitrogen for ammonia synthesis (1). One of the major challenges in initial ammonia synthesis was to provide large quantities of cheap hydrogen gas ¹. Initially, hydrogen was produced from coal by steam gasification (2). CO was subsequently removed by liquefaction and scrubbing with hot caustic soda. As this process was unsuitable for large-scale operations, the water-gas shift (WGS) reaction (3) was added to convert CO with steam into CO₂ and additional H₂. Bosch and Wild developed an iron/chromium-oxide catalyst in 1912, which was first implemented in a coal-based ammonia plant in 1915 ¹. Today, most industrial hydrogen gas is obtained via natural gas reforming (4), which is also combined with the WGS reaction (3) ¹⁴⁻¹⁸. The WGS reaction of coal-derived water-gas is however still used to increase the H₂/CO ratio in Fischer-Tropsch (FT) synthesis ¹⁹. The 1:1 H₂/CO ratio of coal-derived syngas is shifted using an iron-based FT catalyst, leading to H₂ production at the expense of CO. When syngas is obtained from natural gas, the WGS step can be omitted and typically cobalt-based catalysts replace iron-based ones for catalysing FT synthesis ²⁰.





Nowadays, the industrial WGS reaction is performed in two stages ^{1,14,16-18}. The high-temperature shift (HTS) stage is typically performed at 350-450 °C, using an iron-oxide-based catalyst. The catalyst is similar to the original iron/chromium oxide catalyst developed over a century ago by Bosch and Wild with the inclusion of CuO in the precursor to enhance activity ^{18,21-23}. To achieve high CO conversion of this equilibrium-limited reaction, a second low-temperature step is included. This low-temperature shift (LTS) step is typically performed in the range of 190-250 °C using (more expensive) copper-based catalysts ^{14,16,24}. Copper-based catalysts have high WGS activity and no activity for CO (5) and CO₂ (6) methanation side reactions which are thermodynamically favoured under LTS conditions ¹. Methanation is highly undesired at this stage since methane is formed at the expense of the desired H₂. The copper-based catalysts can only be used at relatively low temperatures because of their susceptibility to sintering. The first copper-based WGS catalysts were developed in the late 1920s and suffered from poisons present in the used process streams. When much purer hydrocarbon-derived syngas became available, the use of copper-based catalysts became possible, leading to the first commercial adaptation of a copper-based WGS catalyst in 1963 ¹. In the HTS-LTS configuration, the bulk of CO is converted during HTS with exit CO concentrations typically in the range of 2-4% CO. The residual CO is then largely removed by LTS, lowering the final CO concentration to 0.1-0.3% ^{1,17}. In an ammonia plant, the WGS reaction is combined with a CO methanation (5) step. This ensures CO removal down to 5 ppm ¹, which is necessary since CO is a poison to the Haber-Bosch catalyst, which consists of metallic Fe.



The active phase of iron-based HTS catalysts is magnetite, which is a mixed Fe²⁺/Fe³⁺-oxide phase (Fe₃O₄) ^{14,17,25}. It is formed under process conditions by partial reduction of Fe³⁺-oxide or -oxyhydroxide precursors ^{15,17,18}. Magnetite has an inverse spinel AB₂O₄ structure (Fig. 2). The tetrahedral A-sites are occupied by Fe³⁺ and the octahedral B-sites by an equimolar mixture of Fe²⁺ and Fe³⁺ ¹⁷. The most accepted reaction mechanism of the HTS reaction on magnetite catalysts involves the Fe²⁺/Fe³⁺ redox couple at octahedral sites ^{15,26}

(7-8). Associative mechanisms have been proposed also. Here the CO and H₂O form a surface intermediate before the surface intermediate disintegrates into CO₂ and H₂ (9) ¹⁴. Associative mechanisms are mainly criticised by the lack of observable surface intermediates under HTS conditions. Observing such intermediates can be difficult however if their lifetime is short.

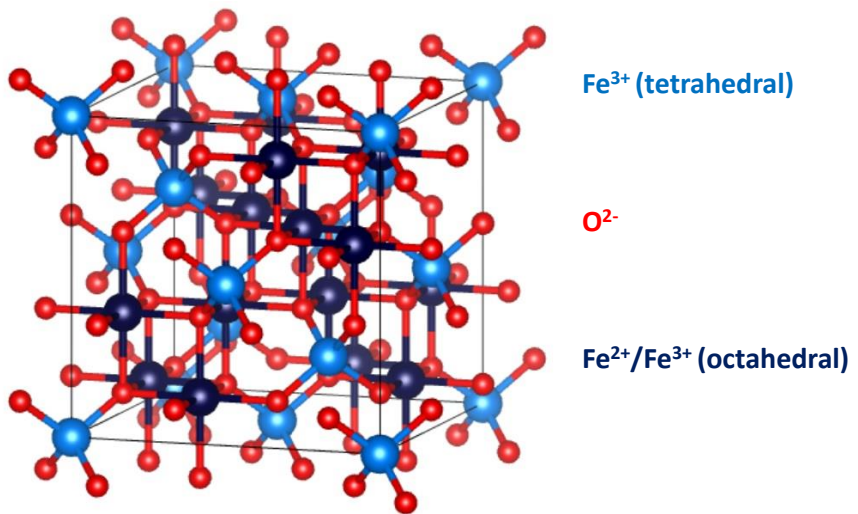


Figure 2. Ball and stick model of the magnetite unit cell produced with ²⁷.

Magnetite as such is prone to thermal agglomeration and over-reduction under WGS process conditions ^{14,16,24,28}. Chromium is added to the catalyst to mitigate these effects. The Fe³⁺-oxide and -oxyhydroxide precursors of the magnetite catalyst are typically prepared via co-precipitation of Fe³⁺ precursors followed by calcination of the resulting precipitates ^{17,18}. Chromium is added during the precipitation procedure as Cr³⁺ salts and typically exists as a mixture of Cr³⁺ and Cr⁶⁺ (hydr)oxides in the fresh catalyst upon calcination ¹⁴. Cr⁶⁺ is subsequently reduced to Cr³⁺ during the formation of the active magnetite phase and is simultaneously incorporated into the octahedral B-sites of the inverse spinel structure ¹⁷. The presence of chromium in the active magnetite catalyst results in higher CO conversion by preventing extensive sintering of the active phase. It also prevents reduction of the active magnetite phase to

lower oxidation state iron-species such, as Wüstite (FeO), metallic iron (α -Fe), and iron carbides¹⁴⁻¹⁷. The over-reduction of magnetite to these species is irreversible and the formation of metallic iron and iron carbides are especially undesired because they catalyse methanation and Fischer-Tropsch side-reactions¹. Despite the consensus on octahedral chromium incorporation, different and often opposing effects of chromium doping on the Fe²⁺/Fe³⁺ redox couple have been reported. Three suggested incorporation mechanisms are currently known; (i) Cr³⁺ replaces an equal amount of Fe³⁺ and Fe²⁺ in the octahedral sites, partially displacing Fe²⁺ to tetrahedral positions in order to maintain a neutral structure²⁹, (ii) chromium replaces octahedral Fe³⁺¹⁴, and (iii) chromium hinders Fe²⁺ formation during the formation of magnetite resulting in a partially oxidised magnetite structure³⁰. Commercial iron-oxide based HTS catalysts also contain small amounts of CuO to enhance CO conversion¹⁴⁻¹⁶. Copper is added during the precipitation procedure as Cu²⁺ salts and is reduced to metallic Cu during the activation procedure. The copper is dispersed as metallic nanoparticles, which are thought to be partially covered by an iron-oxide layer, enhancing CO conversion by providing additional active sites²²⁻²³.

1.3 ALTERNATIVE DOPANTS

Tightening regulations³¹ on the use of Cr⁶⁺ have led to exploration of alternative dopants to stabilise iron-based HTS catalysts¹⁶⁻²⁵⁻³². A rational design approach to achieve this goal is hampered by a lack of understanding of the exact role of chromium and copper dopants under industrially relevant conditions. An important limitation of previous works is that catalysts were typically not investigated after use under industrially relevant HTS conditions, for which three aspects are relevant¹⁻¹⁷. First, activity evaluation should involve gas mixtures containing H₂, CO, CO₂, and H₂O, representative of gas compositions used in an industrial plant. Second, stability should be evaluated using dedicated accelerated testing protocols, because HTS catalysts typically operate for 3-5 years. Third, catalyst testing should include the use of elevated pressure, as HTS is typically performed at pressures up to 80 bar in an industrial plant. Comprehensive reviews on the effects of alternative dopants to chromium on the catalysts' activity can be found in literature¹⁶⁻²⁵⁻³². Many elements have been tested in iron based HTS catalysts, such as aluminium³³⁻³⁴, cerium³⁴⁻³⁷, cobalt³⁴⁻³⁸, copper²¹, gadolinium³⁹⁻⁴⁰, magnesium⁴¹, manganese³⁴⁻⁴², molybdenum⁴³, nickel⁴⁴⁻⁴⁵, niobium⁴⁶, ruthenium⁴⁷, silica⁴¹, thorium⁴⁸,

vanadium ⁴⁹, and zinc ⁵⁰. Aluminium is often identified as a promising dopant in terms of high CO conversion ^{33,34,41,42}. Co-doping of a second dopant with promising dopants like aluminium ⁵¹ and cerium ³⁶ also received attention and co-doping additional elements to nickel was investigated to suppress methanation side reactions ⁴⁴. A direct comparison of the potential of these alternative dopants is however difficult, because the catalyst preparation methods and specific preparation details, such as the calcination temperature, doping levels, as well as test conditions (temperature, pressure, feed gas composition, and test duration) vary among such investigations ^{16,32}. Further, more detailed, discussion on promising alternative dopants is provided in chapter 4.

1.4 MÖSSBAUER SPECTROSCOPY

The most useful information regarding a catalyst working mechanism is arguably found on the surface, since this is where the reaction occurs. However, bulk studies can provide useful information about catalysts as well ^{17,35}. Mössbauer spectroscopy is a powerful bulk technique to study complex iron structures. It is based on the effect discovered by Rudolf Mössbauer in 1958, i.e. the recoilless emission and resonant absorption of gamma radiation, ⁵² awarding him the Nobel Prize in physics in 1961 ⁵³. Despite the availability of almost 50 Mössbauer active elements ⁵⁴, most studies are performed on iron-containing materials because of the abundance and the reasonable half-life of the ⁵⁷Co parent nucleus of ~270 days ⁵³. Studies of tin-based materials are also prevalent because of the reasonable life-time of the parent nucleus ⁵⁴. It should be mentioned however that all Mössbauer active elements can readily be investigated using synchrotron radiation ⁵³. Mössbauer spectroscopy simultaneously provides information on oxidation states, site symmetry, and magnetic properties of the material under investigation ^{53,54}. Besides 'fingerprinting' different materials, the effects of dopants and the distribution of particle sizes can be studied in detail, because they affect the magnetic properties of the material. The versatility of Mössbauer spectroscopy results in its employment in a variety of fields, including geoscience, material science, and catalysis ^{5,17,18,55,56}. An exceptional tour de force of the technique is found in the MIMOS II (Miniaturized MOssbauer Spectrometer, Figure 3) ⁵⁷ on board of both the Spirit and Opportunity Mars rovers. In 2004, the Opportunity rover measured a sample containing Jarosite ($(\text{K,Na})\text{Fe}_3(\text{SO}_4)_2(\text{OH})_6$) *in situ*. The

identification of a Jarosite phase presented evidence of aqueous processes on the planet⁵⁷.



Figure 3. Photograph showing the MIMOS II Mössbauer instrument (pointing towards the sky) attached to the robotic arm of NASA's Opportunity Mars Rover taken on the western rim of Endeavour Crater, Mars (image reprinted from NASA).

Other applications of Mössbauer spectroscopy can be found in catalysis research^{5,17,35,55,58}. The sensitivity for bulk iron structures allows for the deconvolution of the Mössbauer spectrum of the magnetite AB_2O_4 structure into separate sub-spectra for the tetrahedral A-sites and the octahedral B-sites^{29,59}. In this way, the position of chromium and alternative dopants in the catalysts' structure can be compared. Furthermore, the effect of the different dopants on the Fe^{2+}/Fe^{3+} redox couple, which is believed to catalyse the water-gas shift reaction, can be investigated. Since the gamma rays used in Mössbauer spectroscopy are largely unaffected by process gas, it is also an excellent technique for *in situ* investigations. The over-reduction of metal-oxides described in 1.3 is typically investigated by measuring either gas consumption

or evolution in temperature programmed reduction (TPR) experiments³³⁻³⁵. CO- or H₂-TPR conditions however differ significantly from realistic HTS conditions where over-reduction of the active catalyst is often attributed to an imbalance between the reducing (CO, H₂) and oxidising (CO₂, H₂O) gasses present in HTS feeds^{1,16}. *In situ* Mössbauer spectroscopy will allow for a more detailed investigation of the products of over-reduction i.e. α -Fe and FeC_x obtained under industrially relevant HTS conditions.

1.5 THESIS SCOPE

The aim of this work is to expand our understanding of iron-based HTS catalysts towards the replacement of chromium by an alternative dopant. To this end, the effect of chromium- and chromium/copper-doping was investigated in detail. The effect of alternative dopants was then investigated, aiming at the replacement of chromium. Special emphasis was placed on industrial relevance of the prepared and aged catalysts. To underpin the position of chromium and other dopants in the inverse spinel AB₂O₄ structure of the active magnetite catalyst, Mössbauer spectroscopy was employed. Other characterisation methods include x-ray diffraction (XRD), x-ray photoelectron spectroscopy (XPS), Near ambient pressure x-ray photoelectron spectroscopy (NAP-XPS), transmission electron microscopy (TEM), N₂-physisorption, and temperature programmed reduction (CO-TPR). Although, characterisation of the active magnetite catalysts was the main focus, freshly calcined catalysts were also characterised.

In **chapter 2** the effect of chromium doping on HTS catalysts is discussed. Catalysts with different chromium loadings were investigated. Catalysts were prepared via a single step co-precipitation/calcination route and aged under industrially relevant gas compositions for 4 days at 2 and 25 bar. In addition to “standard” characterisation techniques such as XRD, N₂-physisorption, TEM, and CO-TPR, Mössbauer spectroscopy was employed to gain insights into the proposed incorporation mechanisms discussed in this introductory chapter. Mössbauer spectra of aged catalysts were supported by hyperfine parameters obtained from DFT calculations. XPS analysis provided surface analysis of the aged catalysts.

The effect of copper doping on chromium-doped catalysts was investigated in detail in **chapter 3**. Catalysts with different copper loadings were prepared by

a co-precipitation/calcination route. Mössbauer spectroscopy was employed to study in detail the effect of copper doping on freshly calcined catalysts and on chromium-doped magnetite, obtained after ageing the catalyst for 4 days under industrially relevant HTS conditions. In addition to *ex situ* XPS analysis of samples aged under industrially relevant conditions, lab-based NAP-XPS was employed to investigate the copper dopant under working WGS conditions.

In **chapter 4**, a suite of catalysts with alternative dopants was prepared and compared to the chromium- and chromium/copper-doped catalysts. Catalysts containing aluminium, gallium, indium, manganese, zinc, and niobium were prepared, both with and without the copper promoter. Aluminium and aluminium-copper doped catalysts have been identified as promising catalysts in literature, however these catalysts were not tested under industrially relevant HTS conditions before. Mössbauer spectroscopy was employed to reveal the incorporation mechanism of the alternative dopants into the magnetite structure.

In **chapter 5** the effect of aluminium and chromium doping on the undesirable over-reduction of iron-based WGS catalysts under industrially relevant HTS conditions was investigated. *In situ* Mössbauer spectroscopy is explored for the first time to investigate the effect of different dopants on over-reduction of the active catalyst. The gamma rays used in Mössbauer spectroscopy are mostly unaffected by process gas, making it an excellent technique for *in situ* measurements. Furthermore, the sensitivity of Mössbauer spectroscopy for iron species allows for detailed investigation of small particle and amorphous phases typically invisible to standard techniques such as XRD.

REFERENCES

- [1] M.V. Twigg *Catalyst handbook*; 2 ed.; **1989**.
- [2] H.R. Kricheldorf *Handbook of polymer synthesis*; CRC Press: **1991**.
- [3] J.H. Jones The cativa™ process for the manufacture of acetic acid. *Platinum Metals Review* **2000**, *44*, 94-105.
- [4] V.M. Zakoshansky The Cumene Process for Phenol–Acetone Production. *Petroleum Chemistry* **2007**, *47*, 273-284.
- [5] V.P. Santos; T.A. Wezendonk; J.J. Delgado Jaén; A.I. Dugulan; M.A. Nasalevich; H. Islam; A. Chojecki; S. Sartipi; X. Sun; A.A. Hakeem; A. C.J. Koeken; M. Ruitenbeek; T. Davidian; G.R. Meima; G. Sankar; F. Kapteijn; M. Makkee; J. Gascon Metal organic framework-mediated synthesis of highly active and stable Fischer-Tropsch catalysts. *Nature Communications* **2015**, *6*, 6451.
- [6] G.R. List; J.A. Kenar; B.R. Moser History of Fatty Acids Chemistry. **2017**; pp 1-22.
- [7] J. Kašpar; P. Fornasiero; Neal Hickey Automotive catalytic converters: current status and some perspectives. *Catalysis Today* **2003**, *77*, 419-449.
- [8] H.S. Cerqueira; G. Caeiro; L. Costa; F. Ramôa Ribeiro Deactivation of FCC catalysts. *Journal of Molecular Catalysis A: Chemical* **2008**, *292*, 1-13.
- [9] P. Grange Catalytic Hydrodesulfurization. *Catalysis Reviews-Science and Engineering* **1980**, *21*, 135-181.
- [10] U. Hanefeld; L. Lefferts Catalysis: an integrated textbook for students; **2018**.
- [11] R. Schlögl Ammonia synthesis. In *Handbook of heterogeneous catalysis*, **2008**; pp 2501-2575.
- [12] J.W. Erisman; M.A. Sutton; J. Galloway; Z. Klimont; W. Winiwarter How a century of ammonia synthesis changed the world. *Nature geoscience* **2018**, *1*, 636-639.
- [13] J. Humphreys; R. Lan; S. Tao Development and Recent Progress on Ammonia Synthesis Catalysts for Haber–Bosch Process. *Advanced Energy and Sustainability Research* **2021**, *2*, 2000043.
- [14] M. Zhu; I.E. Wachs Iron-Based Catalysts for the High-Temperature Water-Gas Shift (HT-WGS) Reaction: A Review. *ACS catalysis* **2016**, *6*, 722-732.

- [15] C.J. Keturakis; M. Zhu; E.K. Gibson; M. Daturi; F. Tao; A.I. Frenkel; I.E. Wachs Dynamics of $\text{CrO}_3\text{-Fe}_2\text{O}_3$ Catalysts during the High-Temperature Water-Gas Shift Reaction: Molecular Structures and Reactivity. *ACS catalysis* **2016**, *6*, 4786-4798.
- [16] D.W. Lee; M.S. Lee; J.Y. Lee; S. Kim; H.J. Eom; D.J. Moon; K.Y. Lee The review of Cr-free Fe-based catalysts for high-temperature water-gas shift reactions. *Catalysis Today* **2013**, *210*, 2-9.
- [17] M.I. Ariëns; V. Chlan; P. Novák; L.G.A. van de Water; A.I. Dugulan; E. Brück; E.J.M Hensen The role of chromium in iron-based high-temperature water-gas shift catalysts under industrial conditions. *Applied Catalysis B: Environmental* **2021**, *297*, 120465.
- [18] M.I. Ariëns; L.G.A. van de Water; A.I. Dugulan; E. Brück; E.J.M Hensen Copper promotion of chromium-doped iron oxide water-gas shift catalysts under industrially relevant conditions. *Journal of Catalysis* **2022**, *405*, 391-403.
- [19] E. de Smit; B.M. Weckhuysen The renaissance of iron-based Fischer-Tropsch synthesis: on the multifaceted catalyst deactivation behaviour. *Chemical Society Reviews* **2008**, *37*, 2758-2781.
- [20] E. Iglesia Design, synthesis, and use of cobalt-based Fischer-Tropsch synthesis catalysts. *Applied Catalysis A: General* **1997**, *161*, 59-78.
- [21] M. Zhu; T.C.R. Rocha; T. Lunkenbein; A. Knop-Gericke; R. Schlogl; I.E. Wachs Promotion Mechanisms of Iron Oxide-Based High Temperature Water-Gas Shift Catalysts by Chromium and Copper. *ACS catalysis* **2016**, *6*, 4455-4464.
- [22] M. Zhu; P. Tian; R. Kurtz; T. Lunkenbein; J. Xu; R. Schlogl; I.E. Wachs; Y.F. Han Strong Metal-Support Interactions between Copper and Iron Oxide during the High-Temperature Water-Gas Shift Reaction. *Angewandte chemie* **2019**, *131*, 9181-9185.
- [23] M. Zhu; P. Tian; J. Chen; M.E. Ford; J. Xu; I.E. Wachs; Y.F. Han Activation and deactivation of the commercial-type $\text{CuO-Cr}_2\text{O}_3\text{-Fe}_2\text{O}_3$ high temperature shift catalyst. *American Institute of Chemical Engineers* **2019**, *66*, 1-6.
- [24] C. Rhodes; G.J. Hutchings; A.M. Ward Water-gas shift reaction: finding the mechanistic boundary. *Catalysis Today* **1995**, *23*, 43-58.
- [25] D. Damma; P.G. Smirniotis Recent advances in iron-based high-temperature water-gas shift catalysis for hydrogen production. *Current Opinion in Chemical Engineering* **2018**, *21*, 103-110.

- [26] G.K. Boreskov; T.M. Yurieva; A.S. Sergeeva Mechanism of the Conversion of Carbon Monoxide on Iron-Chromium Catalyst. *Kinet. Catal.* **1970**, *11*, 374-381.
- [27] K. Momma; F. Izumi VESTA 3 for three-dimensional visualization of crystal, volumetric and morphology data. *Journal of applied crystallography* **2011**, *44*, 1272-1276.
- [28] D.S. Newsome The Water-Gas Shift Reaction. *Catalysis Reviews Science and Engineering* **1980**, *21*, 275-318.
- [29] M. Robbins; G.K. Wertheim; R.C. Sherwood; D.N.E. Buchanan MAGNETIC PROPERTIES AND SITE DISTRIBUTIONS IN THE SYSTEM $\text{FeCr}_2\text{O}_4\text{-Fe}_3\text{O}_4(\text{Fe}^{2+}\text{Cr}_{2-x}\text{Fe}^{3+x}\text{O}_4)$. *J. Phys. Chem. Solids* **1971**, *32*, 717-729.
- [30] M. do Carmo Rangel; R. Massami Sasaki; F. Galembek Effect of chromium on magnetite formation. *Catalysis Letters* **1995**, *33*, 237-254.
- [31] C. Pellerin; S.M. Booker Reflections on hexavalent chromium: health hazards of an industrial heavyweight. *Environmental Health Perspectives* **2000**, *108*, 402-407.
- [32] M. Zhu; I.E. Wachs A perspective on chromium-free iron oxide-based catalysts for high temperature water-gas shift reaction. *Catalysis Today* **2018**, *311*, 2-7.
- [33] S. Natesakhawat; X. Wang; L. Zhang; U.S. Ozkan Development of chromium-free iron-based catalysts for high-temperature water-gas shift reaction. *Journal of Molecular Catalysis A: Chemical* **2006**, *260*, 82-94.
- [34] F. Meshkani; M. Rezaei Preparation of nanocrystalline metal (Cr, Al, Mn, Ce, Ni, Co and Cu) modified ferrite catalysts for the high temperature water gas shift reaction. *Renewable Energy* **2015**, *74*, 588-589.
- [35] G.K. Reddy; K. Gunasekara; P. Boolchand; P.G. Smirniotis Cr- and Ce-Doped Ferrite Catalysts for the High Temperature Water-Gas Shift Reaction: TPR and Mössbauer Spectroscopic Study. *Journal of Physical Chemistry C* **2011**, *115*, 920-930.
- [36] G.K. Reddy; S. Jhin Kim; J. Dong; P.G. Smirniotis; J.B. Jasinski Long-term WGS stability of Fe/Ce and Fe/Ce/Cr catalysts at high and low steam to CO ratios—XPS and Mössbauer spectroscopic study. *Applied Catalysis A: General* **2012**, *415-416*, 101-110.
- [37] D. Devaiah; P.G. Smirniotis Effects of the Ce and Cr Contents in Fe-Ce-Cr Ferrite Spinels on the High-Temperature Water-Gas Shift Reaction. *Industrial & Engineering Chemistry Research* **2017**, *56*, 1772-1781.

- [38] A.L.C. Pereira; N.A. dos Santos; M.L.O. Ferreira; A. Alborno; M. do Carmo Rangel Effect of cobalt on the activity of iron-based catalysts in water gas shift reaction. *Studies in Surface Science and Catalysis* **2007**, *167*, 225-230.
- [39] C.L. Santos Silva; S.G. Marchetti; A. da Costa Faro Júnior; T. de Freitas Silva; J.M. Assaf; M. do Carmo Rangel Effect of gadolinium on the catalytic properties of iron oxides for WGS. *Catalysis Today* **2013**, *213*, 127-134.
- [40] J. Tsagaroyannis; K.J. Haralambous; Z. Loizos; G. Petroustos; N. Spyrellis Gadolinium-iron ferrites: catalytic effect on the water-gas shift reaction. *Materials Letters* **1996**, *28*, 393-400.
- [41] M. Zhu; Ö. Yalçın; I.E. Wachs Revealing structure-activity relationships in chromium free high temperature shift catalysts promoted by earth abundant elements. *Applied Catalysis B: Environmental* **2018**, *232*, 205-212.
- [42] M.I. Ariëns; L.G.A. van de Water; A.I. Dugulan; E. Brück; E.J.M Hensen Substituting Chromium in Iron-Based Catalysts for the High-Temperature Water-Gas Shift Reaction. *ACS catalysis* **2022**.
- [43] C. Martos; J. Dufour; A. Ruiz Synthesis of Fe₃O₄-based catalysts for the high-temperature water gas shift reaction. *International Journal of Hydrogen Energy* **2009**, *34*, 4475-4481.
- [44] F. Meshkani; M. Rezaei Preparation of mesoporous nanocrystalline alkali promoted chromium free catalysts (Fe₂O₃-Al₂O₃- NiO) for a high temperature water gas shift reaction. *RSC Advances* **2015**, *5*, 9955-9964.
- [45] J.Y. Lee; D.W. Lee; Y.K. Hong; K.Y. Lee The CO removal performances of Cr-free Fe/Ni catalysts for high temperature WGS under LNG reformat condition without additional steam. *International Journal of Hydrogen Energy* **2011**, *36*, 8173-8180.
- [46] D. Damma; D. Jampaiah; A. Welton; P. Boolchand; A. Arvanitis; J. Dong; P.G. Smirniotis Effect of Nb modification on the structural and catalytic property of Fe/Nb/M (M = Mn, Co, Ni, and Cu) catalyst for high temperature water-gas shift reaction. *Catalysis Today* **2019**, *355*, 921-931.
- [47] A. Basinska; F. Domka Iron-ruthenium catalyst for the water-gas shift reaction. *Catalysis Letters* **1993**, *17*, 327-332.
- [48] J.L. Rangel Costa; G.S. Marchetti; M. do Carmo Rangel A thorium-doped catalyst for the high temperature shift reaction. *Catalysis Today* **2002**, *77*, 205-213.

- [49] I.L. Júnior; J.M.M. Millet; M. Aouine; M. do Carmo Rangel The role of vanadium on the properties of iron based catalysts for the water gas shift reaction. *Applied Catalysis A: General* **2005**, *283*, 91-98.
- [50] D.G. Rethwisch; J.A. Dumesic The effects of metal-oxygen bond strength on properties of oxides: II. Water-gas shift over bulk oxides. *Applied Catalysis* **1986**, *21*, 97-109.
- [51] F. Meshkani; M. Rezaei High-temperature water-gas shift reaction over nanostructured Cr-free Fe₂O₃-Al₂O₃-CuO-MO (M: Ba, Ca, Mg and Sr) catalysts for hydrogen production. *Journal of Industrial and Engineering Chemistry* **2015**, *30*, 353-358.
- [52] R.L. Mössbauer Kernresonanzfluoreszenz von Gammastrahlung in Ir¹⁹¹. *Zeitschrift für Physik* **1958**, *151*, 124-143.
- [53] Y. Yoshida; G. Langouche General introduction to Mössbauer spectroscopy. In *Mössbauer spectroscopy tutorial book*, **2013**.
- [54] E. Murad; J. Cashion Theory and Characteristics of the Mössbauer Effect. In *Mössbauer Spectroscopy of Environmental Materials and their Industrial Utilization*, **2004**.
- [55] J. Xie; H.M. Torres Galvis; A.C.J. Koeken; A. Kirilin; A.I. Dugulan; M. Ruitenbeek; K.P. de Jong Size and Promoter Effects on Stability of Carbon-Nanofiber-Supported Iron-Based Fischer-Tropsch Catalysts. *ACS catalysis* **2016**, *6*, 4017-4024.
- [56] E. Murad; J. Cashion Mössbauer Spectroscopy of Environmental Materials and their Industrial Utilization; **2004**.
- [57] G. Klingelhöfer; R.V. Morris; P.A. De Souza Jr.; D. Rodionov; C. Schröder Two earth years of Mössbauer studies of the surface of Mars with MIMOS II. In *NASSAU 2006*, **2007**.
- [58] G.K. Reddy; P. Boolchand; P.G. Smirniotis Sulfur tolerant metal doped Fe/Ce catalysts for high temperature WGS reaction at low steam to CO ratios – XPS and Mössbauer spectroscopic study. *Journal of Catalysis* **2011**, *282*, 258-269.
- [59] H. Topsøe; M. Boudart Mössbauer Spectroscopy of CO Shift Catalysts promoted with Lead. *Journal of Catalysis* **1973**, *31*, 346-359.

2

CHROMIUM DOPING

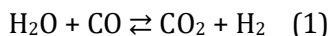
ABSTRACT

Chromium promotion of iron oxide based water-gas shift (WGS) catalysts prepared via co-precipitation/calcination was investigated. Mössbauer spectroscopy and XRD evidence that chromium is incorporated in the calcined hematite ($\alpha\text{-Fe}_2\text{O}_3$) precursor irrespective of the doping level (0-12 wt.%). CO-TPR shows chromium delays the reduction of hematite and the active magnetite (Fe_3O_4) phase. WGS activity was evaluated under realistic conditions for 4 days. Enhanced CO conversion was observed with increased chromium doping. Mössbauer spectra indicate that chromium incorporates into octahedral sites of magnetite and prevents reduction of Fe^{3+} to Fe^{2+} during formation of the active phase. The higher $\text{Fe}^{3+}/\text{Fe}^{2+}$ ratio did not affect the high CO conversion associated with the structural stabilisation mechanism of Cr-doping. Interpretation of the Mössbauer spectra was supported by computational modelling of various chromium and vacancy-doped magnetite structures. The bulk structure of an *in situ* prepared chromium-doped high-temperature WGS catalyst is best described as a partially oxidised chromium-doped magnetite phase. No surface effects of Cr-doping were found.

This chapter was published as: M.I. Ariëns, V. Chlan, P. Novák, L.G.A. van de Water, A.I. Dugulan, E. Brück, E.J.M. Hensen, *Applied Catalysis B: Environmental*, 2021, 297, 120465.

2.1 INTRODUCTION

Hydrogen is an important reagent used mainly in industrial ammonia synthesis^{1,2}. Traditionally, hydrogen is produced by the steam methane reforming (SMR) process, which involves the water-gas shift (WGS) reaction to maximise hydrogen production (1)¹⁻³. As the WGS reaction is mildly exothermic ($\Delta H = -40.6$ kJ/mol), high CO conversion is favoured at low temperature¹. In practice, the WGS section is divided into two steps: (i) a high-temperature shift (HTS) step, which is typically performed at 350-450 °C over an iron-chromium-copper-oxide catalyst and removes the bulk of CO from the synthesis gas product stream from the SMR step, and (ii) a low-temperature shift (LTS) step, performed at temperatures in the range of 190-250 °C on a more active copper-zinc-alumina catalyst³⁻⁶. In the HTS step, the CO concentration is typically decreased from 10-15% CO to 2-4 % CO⁴.



The active phase of HTS catalysts, magnetite, is formed *in situ* by partial reduction of hematite or other bulk Fe³⁺-oxide precursors such as maghemite ($\gamma\text{-Fe}_2\text{O}_3$)^{5,7}. Magnetite has an inverse spinel structure with the formula AB₂O₄⁷. In stoichiometric magnetite the tetrahedral A-sites are occupied by Fe³⁺ and the octahedral B-sites by an equimolar mixture of Fe²⁺ and Fe³⁺⁸. The activity of iron-based WGS catalysts is often linked to the Fe²⁺/Fe³⁺ redox couple in the octahedral sites^{1,9}. Boreskov *et al.*¹⁰ showed that Fe²⁺ can be oxidised by H₂O to Fe³⁺ and Fe³⁺ can be reduced to Fe²⁺ by CO. More recently, Keturakis *et al.*⁵ confirmed that the HTS reaction follows a redox mechanism and that oxygen atoms at the surface are the most abundant reactive intermediates. Magnetite as such is prone to thermal agglomeration and over-reduction under practical WGS conditions^{1,2}. The addition of chromium to the Fe³⁺-oxide precursor typically increases the stability of magnetite towards sintering and reduction of the active phase to Wüstite (FeO), metallic iron, and iron carbides. Metallic iron and iron carbides are highly undesired, because they catalyse methanation and Fischer-Tropsch side-reactions. Keturakis *et al.*⁵ recently showed that hexavalent chromium, which is present on the surface of freshly calcined catalysts, is reduced to Cr³⁺ upon exposure to WGS feed mixtures. Chromium is typically incorporated into the bulk of the magnetite structure to form a Fe_{3-x}Cr_xO₄ solid solution. According to Keturakis *et al.*, the main role of chromium is that of a structural promoter, decreasing sintering and over-reduction. Khan

and Smirniotis ⁷ showed that hematite is converted into magnetite under atmospheric pressure HTS conditions and that chromium stabilises the active phase against sintering. Another proposed role of chromium is that of a chemical promoter, enhancing the WGS activity of magnetite by involvement of the Cr⁶⁺/Cr³⁺ redox couple ^{2,11}. This view is not supported by more recent findings however ¹². Robbins *et al.* ¹³ and Topsøe and Boudart ¹⁴ showed by Mössbauer spectroscopy that chromium is incorporated in octahedral sites of magnetite. The exact position of chromium in the octahedral sites is however still unknown. Robbins *et al.* ¹³ reported that chromium replaces an equal amount of Fe²⁺ and Fe³⁺ in the octahedral sites, while Topsøe and Boudart ¹⁴ could not confirm this for their WGS catalysts. A difference between these studies is that only the work of Topsøe and Boudart involved Mössbauer spectroscopy characterisation of samples after exposure to WGS reaction conditions. A literature review by Zhu and Wachs ¹ mentioned that Cr³⁺ replaces Fe³⁺ at octahedral sites of magnetite, which is the active phase for the HTS reaction. Nevertheless, these authors recently referred to the Robbins model as the correct model of chromium incorporation ¹². Rangel *et al.* ¹⁵ showed that chromium-doped magnetite, prepared by heating chromium-containing iron(III)hydroxyacetates, resulted in a lower Fe²⁺/Fe³⁺ ratio compared to stoichiometric magnetite. This was explained by the preference of Cr³⁺ to occupy octahedral sites, which prevents Fe²⁺ formation. More Fe²⁺ was observed upon use of their catalysts in the WGS reaction. Commercial HTS catalysts also contain small amounts of CuO to enhance CO conversion ¹⁶. Copper is known to form a separate metallic phase, which may be partially covered by an iron oxide over-layer during HTS conditions. These partially covered Cu⁰ nanoparticles enhance CO conversion by providing additional active sites ^{17,18}.

Concerns about the presence of Cr⁶⁺ in the fresh catalyst ¹⁹ have resulted in the search for novel compositions in which chromium is replaced by other dopants ^{6,12}. Rational design of such a catalyst is hindered by a lack of clear understanding of the working mechanism of Cr stabilisation and the local structure of Cr in magnetite. The recent insights discussed above for chromium-doped iron oxide catalysts were mostly obtained under conditions different from industrial HTS conditions, *i.e.*, atmospheric pressure and/or non-representative WGS reaction feed mixtures. A thorough characterisation study of such catalysts aged for a prolonged time under industrially relevant HTS conditions is still lacking.

The aim of this study is to understand better the role of chromium in Fe-based HTS catalysts with a focus on the location of chromium in the active magnetite phase obtained when the catalyst precursor is exposed to industrially relevant WGS conditions ⁴. A range of Fe-Cr mixed oxide catalysts were prepared via a single step co-precipitation/calcination route. Dedicated ageing protocols were used including prolonged exposure to HTS conditions, industrially relevant gas feed compositions, and high pressure. Catalysts were aged at 2 and 25 bar to investigate the influence of the reaction pressure.

The bulk and surface properties of the aged catalysts were investigated by XRD, XPS and Mössbauer spectroscopy. XRD, Mössbauer spectroscopy, CO-TPR, N₂-physisorption, and TEM were also applied to gain insight into the chromium in the catalyst precursors. Mössbauer spectroscopy is a highly sensitive bulk technique based on the effect discovered by Mössbauer in 1958, involving the nearly recoil-free emission and absorption of nuclear X-rays in solids ²⁰. This technique is extremely useful for the study of iron catalysts ^{21,22}. Its sensitivity for iron allows for deconvolution of Mössbauer spectra of the active magnetite phase into separate sub-spectra for the tetrahedral and octahedral Fe sites from which detailed information on local dopant incorporation and oxidation state can be obtained. The interpretation of experimental Mössbauer parameters for chromium-doped magnetite catalysts was supported by computing hyperfine parameters of a range of magnetite structures containing iron vacancies or chromium in octahedral sites. Chromium-doping in tetrahedral positions was not considered based on existing experimental evidence ¹³⁻¹⁵. The formal composition of magnetite is [Fe³⁺]_A[Fe²⁺Fe³⁺]_B[O²⁻]₄ where cations in A and B sites are tetrahedrally and octahedrally coordinated by oxygen, respectively ^{8,23}. The B sublattice exhibits mixed-valence character. The structure of magnetite depends on the temperature: the inverse cubic spinel of magnetite above the Verwey phase transition at 120 K, characterised by equivalency of all A and B sites, transforms in the monoclinic *Cc* structure with 8 different groups of crystallographically equivalent A sites and 16 different groups of crystallographically equivalent B sites.

2.2 EXPERIMENTAL

2.2.1 CATALYST PREPARATION

Catalysts were prepared by a single-step co-precipitation/calcination method described elsewhere ²⁴. Briefly, appropriate amounts of chromium and iron nitrates were dissolved in deionised water and precipitated by addition of an aqueous NaOH solution. The resulting slurry was aged at 60 °C and pH 10 for 1 hour, after which it was filtered and washed before drying at 150 °C for 3 hours and calcination at 400 °C for 4 hours in air. A total of 5 catalysts with compositions of x wt.% Cr₂O₃ ($x = 0, 1, 4, 8, \text{ and } 12$) in α -Fe₂O₃ were prepared in this way. Catalysts were denoted as Cr(x) in the following.

2.2.2 CATALYST CHARACTERISATION

XRD patterns were recorded on a PANalitical X'pert pro diffractometer between $10^\circ < 2\theta < 100^\circ$, step size 0.008° , using Cu-K α radiation. The HighScore Plus software was used for spectral fitting. The aged catalysts were stored under argon before characterisation.

CO-TPR experiments were performed in a quartz tube suspended in a tubular oven. In a typical experiment, 50 mg freshly calcined catalyst was diluted with 200 mg SiC and placed in between quartz wool plugs in a quartz reactor tube. The samples were pre-treated at 400 °C under 10% O₂/He flow (50 ml min⁻¹) for 1 h. The reactor was then purged with He and cooled to room-temperature. The temperature was subsequently ramped to 650 °C under a constant flow of 10% CO/He (50 ml min⁻¹). A heating rate of 5 °C min⁻¹ was maintained during pre-treatment and the TPR experiment. Product formation was monitored by an online mass spectrometer (ESS, GeneSys Evolution), different reduction temperatures were determined by the shift in CO₂ evolution peak.

Transmission ⁵⁷Fe Mössbauer spectra were recorded in constant-acceleration and sinusoidal velocity spectrometers using a ⁵⁷Co(Rh) source. The sample and the ⁵⁷Co(Rh) source were kept at the same temperature during the Mössbauer measurements. Velocities are reported relative to α -Fe at room-temperature. The Mosswin 4.0 software was used for spectral fitting ²⁵. Samples were stored under argon atmosphere prior to and during characterisation.

N₂ physisorption experiments were performed on a Micromeritics 2420 ASAP instrument. Samples were degassed with nitrogen at 140 °C for at least 1 hour prior to characterisation.

TEM images were recorded on a FEI Tecnai 20 (type Sphera) TEM. Samples were suspended in acetone by sonication, and subsequently dispersed over a Cu grid containing holey carbon film. Particle size averages were obtained by counting 200 particles per sample using ImageJ software.

XPS were recorded on a Thermo Scientific K-Alpha spectrometer using an aluminium anode (Al K α = 1486.6 eV). Binding energy calibration was performed relative to adventitious carbon at BE = 285 eV. The CasaXPS software (version 2.3.19PR1.0) was used for spectral fitting. Samples were transferred to the spectrometer under vacuum.

2.2.3 CATALYTIC ACTIVITY MEASUREMENTS

Catalytic activity measurements were performed in a parallel high-throughput setup at 2 or 25 bar. In a typical experiment, the reactor tubes were charged with 100 mg catalyst diluted with 500 mg α -Al₂O₃. The reactors were purged with nitrogen after which the temperature was raised to 250 °C at a rate of 2 °C min⁻¹. Steam was added followed by the addition of reaction gas to reach the desired composition (37% H₂, 9% CO, 4% CO₂, 17% N₂, 33% H₂O). The temperature was subsequently ramped to 450 °C at a rate of 1 °C min⁻¹ and maintained for 24 hours while CO conversion was recorded. The temperature was then lowered to 360 °C and the activity was measured for 24 hours. A second thermal ageing step was carried out at 450 °C for 24 hours followed by additional activity measurement at 360 °C for 24 hours. The temperature was then lowered to 250 °C and the H₂, CO, and CO₂ flows were switched to N₂. When no more CO was observed in the effluent stream, steam addition was stopped and the catalysts were cooled to room-temperature in nitrogen flow. The reactors were then closed off and transferred to a glovebox where the catalysts were removed under inert atmosphere to ensure no air exposure occurred. The catalysts were finally stored under an argon atmosphere prior to characterisation.

2.2.4 COMPUTATIONAL MODELLING

Hyperfine parameters required for simulating Mössbauer spectra were calculated based on spin-polarised density functional theory (DFT) using WIEN2k ²⁶, which employs full-potential augmented plane-wave method to describe the ion-electron interactions. The size of the basis set and the number of k -points in reciprocal space were carefully converged. Electron-exchange correlation was represented by the generalised gradient approximation (GGA) with the Perdew-Burke-Ernzerhof (PBE) exchange-correlation functional. Radii of the atomic spheres for Fe, Cr, and O atoms were chosen as 2.0, 1.85, and 1.5 Bohr units (1 Bohr unit, $a_0 = 5.29 \times 10^{-11}$ m).

The isomer shift (IS) in Mössbauer spectra scales linearly with the electron charge density at the Fe nucleus relative to a reference, which is typically metallic bcc α -Fe. The charge density at a particular Fe site was determined by DFT as the charge within a uniformly charged Thomson sphere with radius $R_0 = 5 \times 10^{-5} a_0$. The computed charge difference $\Delta\rho$ with the reference obtained in this way was converted to the IS using $IS = \alpha * \Delta\rho$, where α was obtained by calibration using a set of 11 experimental IS values of Fe reference compounds ²⁷. The original set of 11 compounds was extended to 16 reference materials in this work, yielding $\alpha = -0.32 \pm 0.02 \text{ mm s}^{-1} e^{-1} a_0^3$.

The total local magnetic field at Fe nucleus was calculated by DFT as a sum of all relevant contributions. The hyperfine fields induced by electron orbital moment and due to interaction with the electron spin (within the dipole limit) were obtained straightforwardly from the occupation matrices of the Fe 3d electrons. To compute the contact part of the hyperfine field, the method of Novák and Chlan was used ²⁸, involving calculation of the spin magnetic moments of the Fe 3d and 4s electrons. Additionally, the dipolar field from the neighbouring atomic moments in the lattice was evaluated by direct summation of moments within a sufficiently large Lorentz sphere (radius = 250 a_0).

Table 1. Fe-oxide reference structures used to determine hyperfine parameters of Fe nuclei using DFT.

Structure ^a	Name ^b	Cr content (%)	Content of Fe vacancies (%)	Space group	Lattice parameters (Å)
Fe ₃ O ₄	Fe ₃ O ₄ (magnetite)	0	-	Fd-3m	a = 8.424
(Fe ₈)[CrFe ₁₅]O ₃₂	Cr-1	4.2	-	R-3m	a = 11.901 c = 14.574 γ = 120°
(Fe ₈)[Cr ₂ Fe ₁₄]O ₃₂	Cr-2 (I)	8.3	-	C2	a = 11.932 b = 25.377 c = 11.853 γ = 160.6°
	Cr-2 (II)			Cm	a = 11.933 b = 8.410 c = 11.854 γ = 89.5°
	Cr-2 (III)			C2/m	
(Fe ₂)[CrFe ₃]O ₈	Cr-4	16.7	-	R-3m	a = 5.870 c = 14.883 γ = 120°
(Fe ₂)[Cr ₂ Fe ₂]O ₈	Cr-8	33.3	-	Fm-3	a = 8.395
(Fe ₁₆)[□Fe ₃₁]O ₆₄	Vac-0.5	-	2.1	R-3m	a = 11.914 c = 29.183 γ = 120°
(Fe ₂₄)[□ ₈ Fe ₄₀]O ₉₆	Vac-8/3 (maghemite)	-	11.1	P4 ₁ 2 ₁ 2	a = 8.503 c = 25.456
(Fe ₂)[□Fe ₃]O ₈	Vac-4	-	16.7	R-3m	a = 5.876 c = 14.394 γ = 120°

^a Fe ions in tetrahedral positions are shown in parentheses (), Fe ions in octahedral position in brackets []. Octahedral metal vacancies are indicated by a square □.

^b Cr-x refers to chromium-doped models with x indicating the number of octahedral Fe ions being replaced by Cr³⁺ per unit cell. Vac-x refers to structures containing octahedral vacancies with x referring the number of such vacancies per unit cell.

Various structural models of magnetite were employed to determine the total hyperfine magnetic field and the isomer shift at the Fe nuclei including magnetite, octahedral-vacancy-containing magnetite ($\text{Fe}_{3(1-\delta)}\text{O}_4$), and chromium-doped magnetite ($\text{Fe}_{3-x}\text{Cr}_x\text{O}_4$) where Fe in octahedral positions was replaced by Cr. The structures, their space groups and optimised lattice parameters are listed in Table 1. All structural models were considered within one conventional spinel unit cell (or its equivalent for cases with different symmetry). For the lowest Cr concentrations the number of possible models is reasonable (one for 4 % Cr and three for 8 % Cr), however, for larger Cr concentrations the number of variants would be unfeasible, and thus only the most symmetric models were selected. In addition to investigating the impact of chromium content, the three different Cr-2 models allow to estimate the impact of Cr arrangement on the observed quantities. The Cr arrangement in all these DFT model structures is fixed and repeated infinitely by periodic boundary conditions and, therefore, cannot represent the complete structural variation of the experimental sample. Hence, we used parameters that were the weighted averages within each Fe sublattice (A or B sites in the AB_2O_4 structure of magnetite).

2.3 RESULTS AND DISCUSSION

2.3.1 CALCINED CATALYSTS

Chromium-doped iron oxide catalysts were prepared using a co-precipitation/calcination method adapted from Meshkani and Rezaei ²⁴. Routine physico-chemical properties of the calcined catalysts are shown in Table 2. XRD patterns of freshly calcined catalysts are presented in Figure 1. The main reflections in the XRD patterns belong to hematite, irrespective of chromium doping level. The position of the (110) reflection of hematite shifts to higher 2θ values with increasing chromium content in comparison to non-doped Cr(0). The values for Cr(8) and Cr(12) are, however, similar. The shift of the hematite diffraction lines to higher 2θ values points to contraction of the unit cell, which can be explained by the incorporation of chromium cations (Cr^{3+}) with a smaller radius (62 pm) than iron cations (Fe^{3+} , 65 pm) in the host structure. No other phases were observed, indicating that pure hematite was formed. This, however, does not exclude the presence of small (< 3 nm) or amorphous oxides of iron or chromium ²⁹.

XRD line broadening analysis shows a decreasing crystallite size with increased chromium content from 44 nm for Cr(0) to 25 nm for Cr(8) (Table 2). The average crystallite sizes of the Cr(8) and Cr(12) samples were similar. Average particle sizes obtained by TEM analysis (Fig. 2) show a similar trend. The average particle size decreased from 28 ± 17 nm for Cr(0) to 12 ± 4 nm for Cr(8). The average particle size of the Cr(8) and Cr(12) sample as judged from TEM analysis were again similar. The trends in particle size established by TEM and XRD analysis are confirmed by the surface areas determined by N_2 physisorption (Table 2), showing a higher surface area with increasing chromium content.

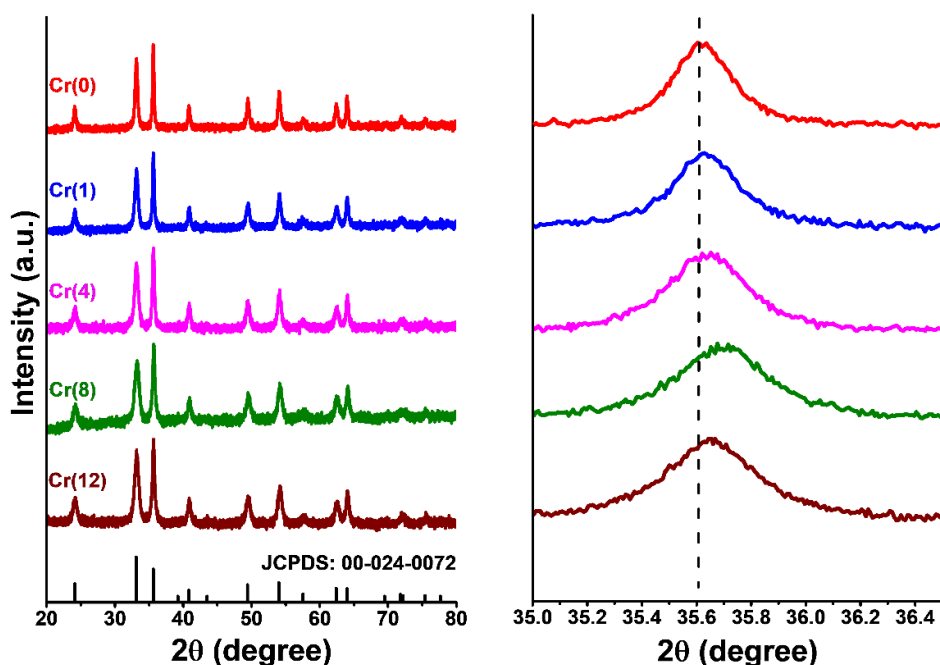


Figure 1. XRD patterns of freshly calcined catalysts (right panel shows magnified region around the (110) reflection of hematite).

Table 2. Selected physico-chemical properties of the calcined catalysts.

Sample	d (nm)		BET SA (m ² g ⁻¹)	V _{tot} (cm ³ g ⁻¹)	Average d _{pore} (nm)	Cr ₂ O ₃ ^b (wt. %)	Na ₂ O ^b (wt. %)
	TEM	XRD ^a					
Cr(0)	28 ± 17	44	45	0.22	19.9	0.0	0.6
Cr(1)	18 ± 11	38	56	0.22	15.7	0.8	0.6
Cr(4)	17 ± 7	29	81	0.23	11.2	3.9	0.7
Cr(8)	12 ± 4	25	110	0.25	9.2	7.5	1.6
Cr(12)	12 ± 4	24	125	0.31	9.9	11.3	2.1

^a Calculated from XRD line broadening analysis using the Scherrer equation.

^b Obtained by XRF analysis. The Cr₂O₃ content is slightly lower than intended, possibly due to the presence of some residual Na₂O³⁰.

^c Surface area (SA) determined by the Brunauer-Emmett-Teller (BET) method, pore volume (V_{tot}), and pore diameter (d_{pore}) using the BJH (Barrett-Joyner-Halenda) method.

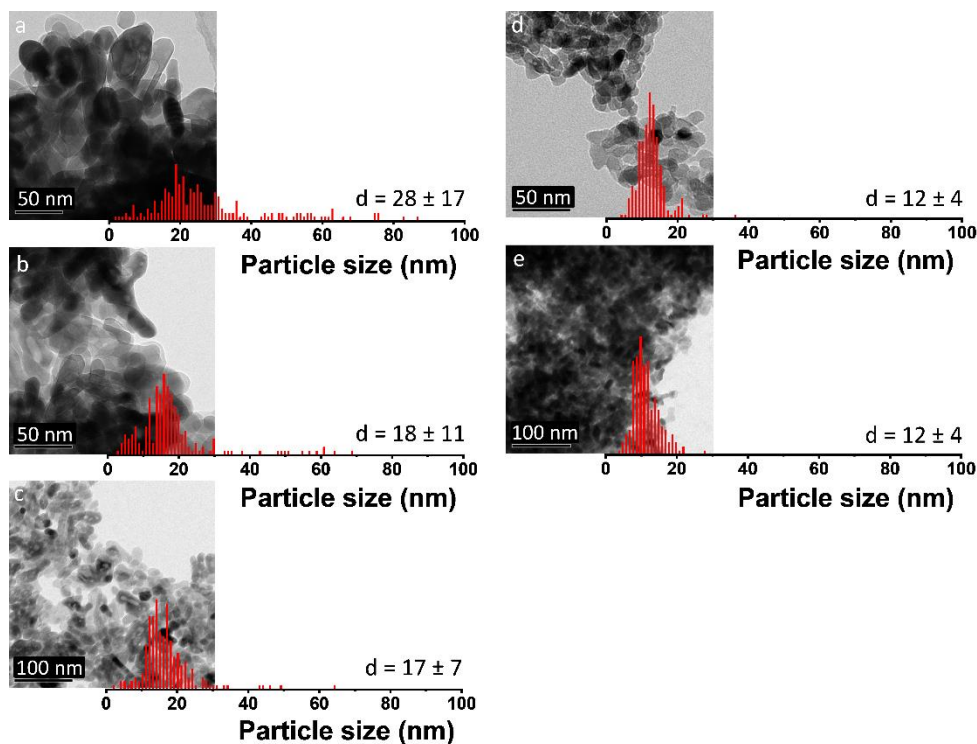


Figure 2. Particle sizes of calcined catalysts as determined by TEM analysis: (a) Cr(0), (b) Cr(1); (c) Cr(4); (d) Cr(8), and (e) Cr(12).

Room-temperature Mössbauer spectra are shown in Figure 3. These spectra contain a magnetically split sextet with isomer shift (IS) values of $\sim 0.38 \text{ mm s}^{-1}$ and quadrupole splitting (QS) values of $\sim -0.22 \text{ mm s}^{-1}$, irrespective of the chromium content (Table 3). These parameters, in combination with an average hyperfine magnetic field between 50.5 T and 47.3 T, confirm that the sample consists of hematite^{31,32}, in agreement with the XRD analysis. The hyperfine magnetic field distribution as displayed in Figure 4 becomes broader with increasing chromium content. Such broadening can arise from a decrease in hematite particle size and/or the incorporation of a dopant in hematite³³. We already discussed that the average particle size of the hematite phase decreased with increasing chromium content (Table 2). Therefore, we cannot unequivocally assign the broadening in the hyperfine magnetic field distribution to increasing levels of chromium doping. The similar particle sizes determined for the Cr(8) and Cr(12) samples provide a strong indication that the broadening of the hyperfine magnetic field distribution with increasing chromium content from Cr(8) to Cr(12) is the result of the incorporation of additional chromium into hematite. The superparamagnetic (SPM) phase with an isomer shift of 0.38 mm s^{-1} (Table 3), which is observed in the Mössbauer spectrum of the Cr(12) sample, points to a fraction of small particles of an Fe-oxide phase with high-spin Fe^{3+} ions in octahedral positions²². Based on the Mössbauer parameters of the SPM phase alone, it cannot be established what bulk Fe^{3+} -oxide phase is present.

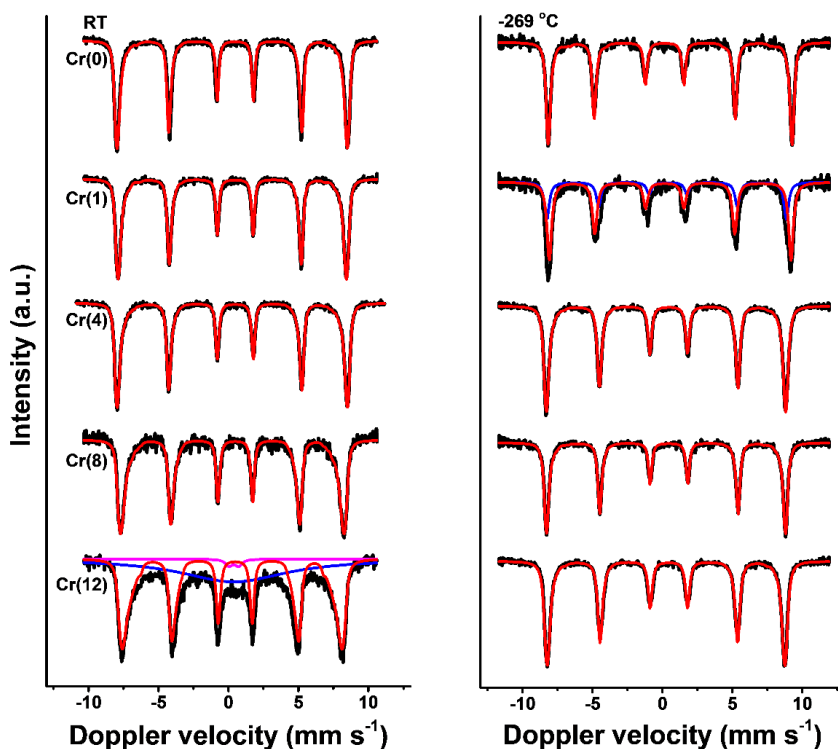


Figure 3. Mössbauer spectra calcined of catalysts recorded at room-temperature (left) and -269 °C (right).

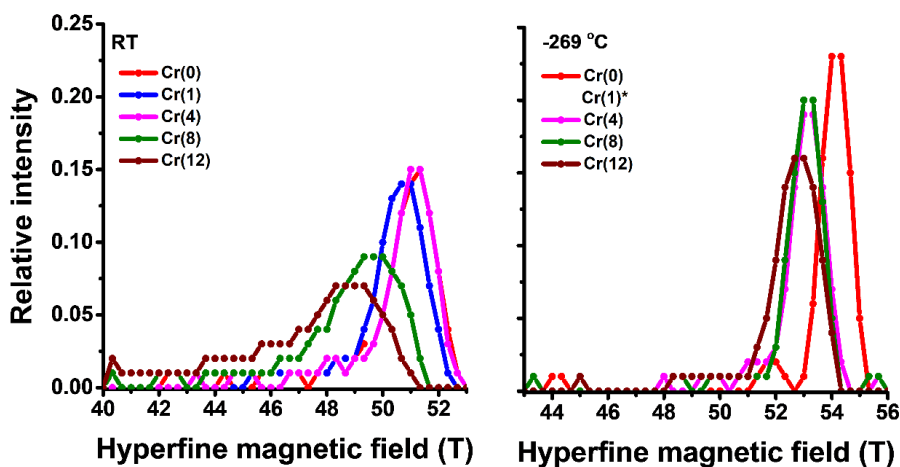


Figure 4. Hyperfine magnetic field distributions obtained by fitting of the Mössbauer spectra recorded at room-temperature (left) and -269 °C (right) (* No hyperfine magnetic field distribution was fitted for the spectrum Cr(1) recorded at -269 °C because of a partial Morin transition, cf. Fig. 3, Table 3).

Table 3. Mössbauer parameters of freshly calcined samples obtained at room-temperature (RT) and -269 °C.

T (°C)	Sample	IS (mm s ⁻¹)	QS (mm s ⁻¹)	Hyperfine field (T)	Γ (mm s ⁻¹)	Phase	(%) ^d
RT	Cr(0)	0.38	-0.23	50.5†	0.23	α-Fe ₂ O ₃	100
	Cr(1)	0.38	-0.21	50.1†	0.23	α-Fe ₂ O ₃	100
	Cr(4)	0.38	-0.22	50.5†	0.24	α-Fe ₂ O ₃	100
	Cr(8)	0.38	-0.21	48.5†	0.25	α-Fe ₂ O ₃	100
	Cr(12)	0.37 0.38* 0.38*	-0.22 0.69 -	47.3† - -	0.32 0.60 9.28	α-Fe ₂ O ₃ Fe ³⁺ SPM Fe ³⁺ SPM	54 2 44
-269 °C	Cr(0)	0.35	0.40	53.6†	0.28	α-Fe ₂ O ₃ AF ^c	100
	Cr(1)	0.36	0.39	53.7†	0.40	α-Fe ₂ O ₃ AF	68
		0.35	-0.10	53.2†	0.40	α-Fe ₂ O ₃ WF ^c	32
	Cr(4)	0.35	-0.19	52.8†	0.30	α-Fe ₂ O ₃	100
	Cr(8)	0.36	-0.21	52.7†	0.26	α-Fe ₂ O ₃	100
Cr(12)	0.36	-0.20	52.4†	0.33	α-Fe ₂ O ₃	100	

^a Fixed values are marked with an asterisk (*), average values with a dagger (†).

^b Experimental uncertainties: Isomer shift: IS ± 0.01 mm s⁻¹, quadrupole splitting: QS ± 0.01 mm s⁻¹, line width: Γ ± 0.01 mm s⁻¹, hyperfine magnetic field: ± 0.1 T, spectral contribution: ± 3%.

^c AF (antiferromagnetic), WF (weakly ferromagnetic) ³².

^d Spectral contribution.

To investigate the SPM fraction observed for Cr(12) in the room-temperature Mössbauer spectrum in more detail, a Mössbauer spectrum was recorded at -269 °C to regain magnetic splitting. The low-temperature Mössbauer spectra (Fig. 3) and the deconvolution results (Table 3) confirm the presence of a single hematite phase in Cr(12), indicating that the SPM fraction observed in the room-temperature Mössbauer spectra is hematite. In the Mössbauer spectrum of Cr(0) measured at -269 °C, a hyperfine magnetic field of 53.6 T was observed with a QS value of 0.40 mm s⁻¹ (Table 3). The higher hyperfine magnetic field of Cr(0) compared to the Cr(4)-Cr(12) samples (~52.7 T) and the QS value of ~0.40 mm s⁻¹ indicate that hematite underwent the Morin transition ³⁴. The Morin transition occurs for hematite particles larger than 20 nm ³². This transition is observed for Cr(0), which is the only sample containing hematite particles larger than 20 nm (Table 2). In the Cr(1) sample, two spectral contributions of hematite can be distinguished (Fig. 3). For the antiferromagnetic phase, the occurrence of the Morin transition indicates that this sample contains a fraction of particles with a size larger than 20 nm. The

Mössbauer spectra of Cr(4), Cr(8), and Cr(12) show a single sextet belonging to hematite (Fig. 3, Table 3). As mentioned above, the broadening of the hyperfine magnetic field distribution from Cr(8) to Cr(12) points to chromium incorporation into hematite. Thus, the low-temperature Mössbauer measurements provide strong evidence that the superparamagnetic Fe³⁺-oxide phase observed in the Cr(12) sample at room temperature belongs to chromium-doped hematite.

The influence of chromium on the reducibility of the calcined catalysts was determined by CO-TPR (Fig. 5). The TPR patterns consist of two main reduction peaks, representing the reduction of hematite to magnetite (Fe₃O₄), and the further reduction of magnetite to metallic Fe, possibly followed by carburisation. A Mössbauer spectrum recorded after quenching a TPR experiment of Cr(0) at 411 °C (Fig. 5) revealed the nearly complete transformation to Hägg-carbide (χ -Fe₅C₂) with only a small amount of α -Fe (3.6%) remaining. This shows that the chromium-free hematite phase can be easily reduced to metallic Fe, which is then rapidly carburised in the presence of CO. The reduction feature of hematite to magnetite (Fe₃O₄) shifted from 270 °C to 330 °C with increasing chromium content. The start of the reduction of magnetite was delayed from 280 °C for Cr(0) to 360 °C for Cr(12). Small reduction features between 150 °C and 230 °C relate to the reduction of a small amount of hexavalent chromium, which is most likely present at the surface in chromium-containing samples³⁵. This reduction feature is indeed absent in the CO-TPR pattern of the chromium-free Cr(0) (Fig 5). CO₂ evolution observed at ~500 °C, prevalent in all reduction patterns, can be attributed to the Boudouard reaction. These results show that chromium doping delays the formation and over-reduction of magnetite, which is considered the active phase in the WGS reaction.

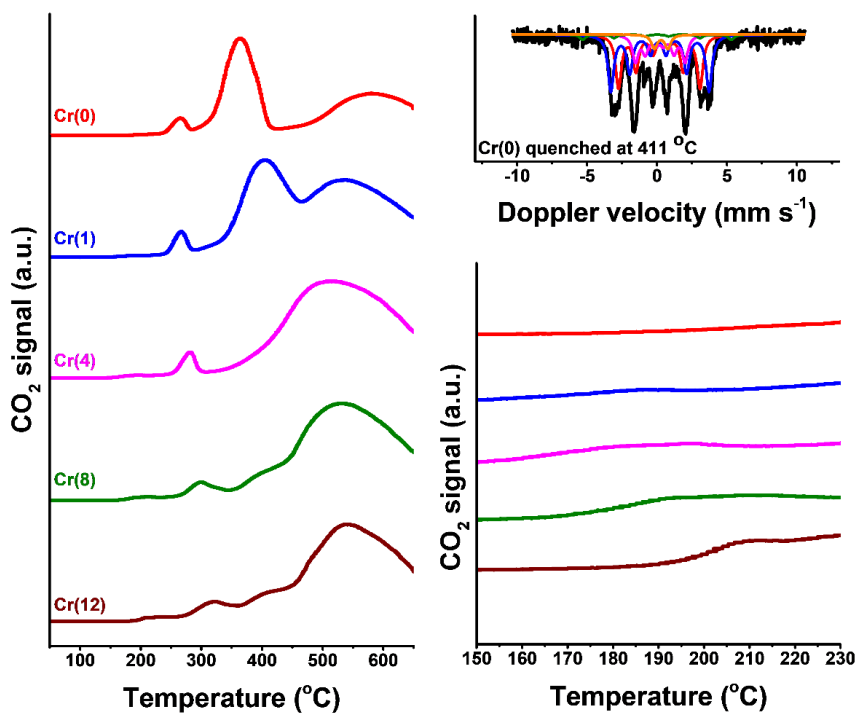


Figure 5. CO-TPR patterns from 50 °C to 650 °C (left) and from 150 °C to 230 °C (right) of calcined catalysts. Mössbauer spectrum recorded after quenching Cr(0) at 411 °C. Sub-spectra of χ -Fe₅C₂(I), χ -Fe₅C₂(II), and χ -Fe₅C₂(III) are indicated in red, blue, and magenta, respectively. The sub-spectrum of α -Fe is shown in green, SPM Fe_xC in orange.

2.3.2 CATALYTIC ACTIVITY

Figure 6 shows the CO conversion of the catalysts under industrially relevant HTS conditions. After activation and ageing for 24 hours at 450 °C at 25 bar, the catalytic performance was compared at 360 °C, away from equilibrium conditions. Clearly, the activity increased with chromium content. The trend was similar after a second 24 hour ageing step at 450 °C with slightly higher activities for all samples at 360 °C. The promoting effect of chromium on the CO conversion is usually attributed to a higher surface area^{1,5}, which is in line with the textural properties of the calcined catalyst precursors (Table 2). The catalysts exposed to industrially relevant conditions for 4 days at 2 bar show a similar increasing CO conversion with increasing chromium content after the

first and second thermal ageing step. The higher activities observed for chromium-doped catalysts at both reaction pressures indicate that the structural stabilisation by chromium doping is independent of pressure.

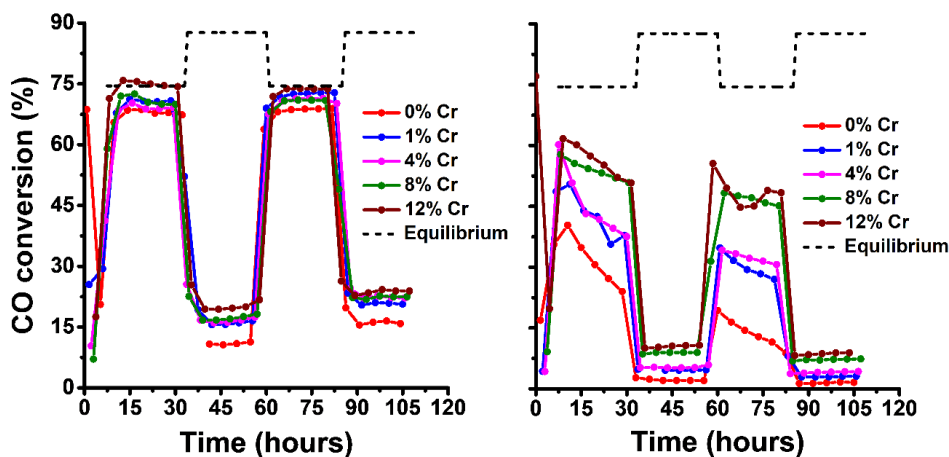


Figure 6. CO conversion chromium-doped catalysts with time on stream during HTS at (left) 25 bar and (right) 2 bar, (37% H₂, 9% CO, 4% CO₂, 17% N₂, 33% H₂O). The temperature was varied between 360 °C and 450 °C.

2.3.3 USED CATALYSTS

After the HTS reaction, the catalyst samples were stored and transported under argon to prevent oxidation of the active magnetite catalysts to maghemite. The used catalysts were investigated with XRD, Mössbauer spectroscopy, and XPS. Mössbauer parameters computed by DFT using various magnetite structural models were used to interpret the experimental Mössbauer spectra.

The XRD patterns of the used catalysts, after exposure to industrially relevant HTS conditions for 4 days at 25 and 2 bar, show reflections that can be attributed to either magnetite or maghemite (Fig. 7). The presence of maghemite is, however, unlikely because it will typically convert into magnetite under WGS conditions⁵. These findings also show that the formation of magnetite does not depend on the reaction pressure.

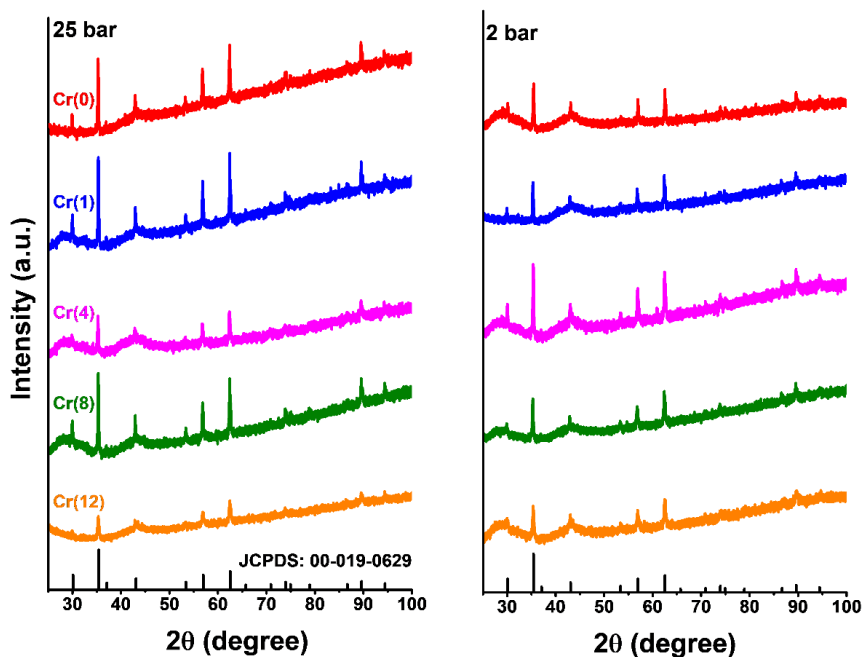


Figure 7. XRD patterns of discharged catalysts after treatment under HTS conditions for 4 days at 25 bar (left) and 2 bar (right). Magnetite reference: JCPDS no. 00-019-0629

Decreasing crystallite sizes were observed with increasing chromium content (Table 4), independent of the reaction pressure, which is in line with the proposal that chromium prevents sintering of the magnetite phase^{1,2}.

Table 4. Average crystallite size of calcined hematite in fresh and activated magnetite phase in used catalysts.

Sample	d_{XRD} (nm) ^a		
	Calcined	25 bar	2 bar
Cr(0)	44	74	71
Cr(1)	38	89	85
Cr(4)	29	55	52
Cr(8)	25	64	41
Cr(12)	24	30	27

^a Determined using the Scherrer equation.

Before discussing the Mössbauer spectra of the used catalysts primarily consisting of magnetite, we first discuss the results of the calculations of hyperfine parameters for different magnetite structures, *i.e.*, magnetite,

magnetite with octahedral Fe vacancies ($\text{Fe}_{3(1-\delta)}\text{O}_4$), and chromium-doped magnetite ($\text{Fe}_{3-x}\text{Cr}_x\text{O}_4$) where Fe^{3+} in octahedral positions is replaced by Cr^{3+} .

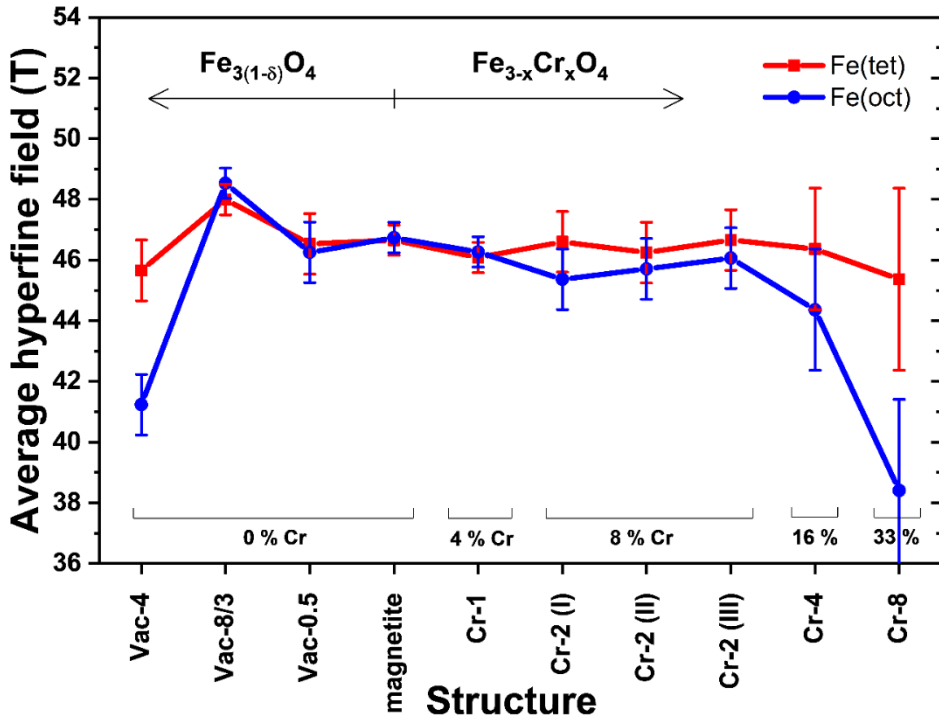


Figure 8. Hyperfine magnetic field values for tetrahedral and octahedral Fe in various magnetite reference structures calculated by DFT. The Vac-8/3 structure represents maghemite.

The calculated hyperfine magnetic field values are displayed in Figure 8, with error bars reflecting the dispersion of values in a given Fe sublattice and the estimated overall uncertainty due to the computational setup. Slightly higher octahedral and tetrahedral hyperfine magnetic field values are predicted for maghemite (Vac-8/3) in comparison to the non-doped magnetite structure. This is in line with experimental data for these two structures³¹. Vacancy doping has a negligible effect on the hyperfine magnetic field values when the vacancy content was low (Vac-0.5), whereas a significant decrease in the octahedral hyperfine magnetic field was observed for the $\text{Fe}_{3(1-\delta)}\text{O}_4$ structure with a higher vacancy content (Vac-4). It should be pointed out, however, that the Vac-4 structure will likely not occur in practice, because its vacancy content

is higher than that of maghemite (Vac-8/3). Maghemite can be regarded as fully oxidised magnetite. Therefore, it can be concluded that the influence of vacancy doping on the hyperfine magnetic field values is small. On the other hand, the octahedral hyperfine magnetic field value decreases with increasing substitution of octahedral Fe by Cr. This substitution in octahedral sites did not affect the tetrahedral hyperfine magnetic field values as much.

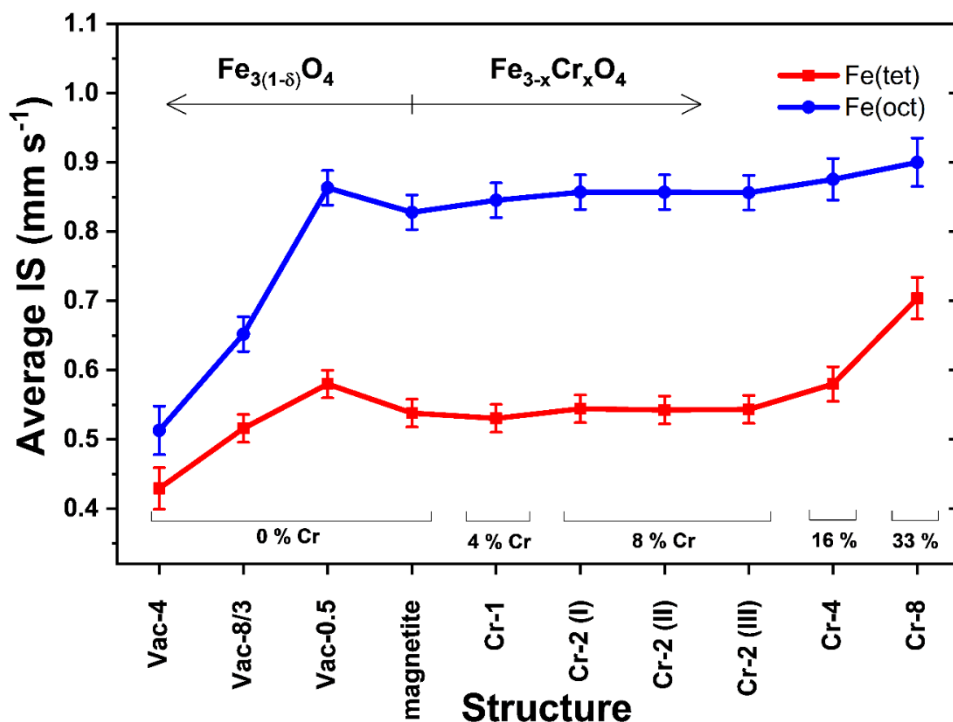


Figure 9. IS values for tetrahedral and octahedral Fe of various magnetite reference structures determined by DFT calculations. The Vac-8/3 structure represents maghemite.

The IS values computed for the tetrahedral and octahedral Fe sites in reference structures are shown in Figure 9. The IS values of the octahedral sites are typically higher than those of the tetrahedral sites. The higher octahedral IS values can be explained by the presence of both Fe³⁺ and Fe²⁺ in these sites, whereas the tetrahedral sites are only occupied by Fe³⁺. For the vacancy-doped Vac-8/3 and Vac-4 structures, a significant decrease of the octahedral IS values is predicted, which demonstrates that the absence of Fe²⁺ results in a lower IS

compared to the mixed-valence ($\text{Fe}^{3+}/\text{Fe}^{2+}$) octahedral sites in stoichiometric magnetite. Introducing chromium results in higher octahedral IS values in the $\text{Fe}_{3-x}\text{Cr}_x\text{O}_4$ structures. The higher IS values can be explained by the replacement of octahedral Fe^{3+} by Cr^{3+} , resulting in a lower $\text{Fe}^{3+}/\text{Fe}^{2+}$ ratio of the octahedral B sites. The computed tetrahedral IS values for the Cr-4 and Cr-8 structures are higher than those of the Cr-1 and Cr-2 structures. This trend is in line with the high IS value observed for chromite (FeCr_2O_4) where the tetrahedral sites are completely occupied by Fe^{2+} ions³⁶.

In summary, modelling shows that incorporation of chromium in octahedral sites results in a decrease of the hyperfine magnetic field for the octahedral Fe sites, whereas the hyperfine magnetic field of tetrahedral Fe remains unaffected. The influence of octahedral vacancies on the hyperfine magnetic field is negligible. The data also show a significant effect of chromium doping on octahedral IS values due to a change in the $\text{Fe}^{3+}/\text{Fe}^{2+}$ ratio. The following trends can be discerned: when Fe^{3+} is replaced by Cr^{3+} , the octahedral IS value increases with Cr content. In structures where Cr^{3+} replaces an equal amount of Fe^{3+} and Fe^{2+} in the octahedral sites, the octahedral isomer shift is unaffected by chromium doping. In a structure where the presence of octahedral Cr^{3+} prevents the reduction of Fe^{3+} to Fe^{2+} , the octahedral IS will decrease with increased chromium content.

The computed hyperfine parameters will be used to discuss the experimentally obtained parameters with a focus on the impact of chromium incorporation. Room-temperature Mössbauer spectra of used catalysts after treatment for 4 days at 2 and 25 bar are shown in Figure 10. These spectra were fitted with two sub-spectra representing Fe^{3+} in tetrahedral sites and mixed valence $\text{Fe}^{2+}/\text{Fe}^{3+}$ in octahedral sites. A decreasing trend in the hyperfine magnetic field values of the octahedral sites from 45.7 T to 44.1 T was observed with increasing chromium content for the used catalysts after treatment at 25 bar (Table 5). The hyperfine magnetic field values of the tetrahedral sites did not vary significantly (48.6 T +/- 0.1 T) for the used Cr(0)–Cr(8) catalysts with a slightly lower value of 48.4 T being observed for the used Cr(12) catalyst. A decrease in the hyperfine magnetic field can be the result of chromium incorporation or smaller crystallites³³. The finding that the hyperfine magnetic fields of the tetrahedral sites did not change much with chromium content shows that a particle size effect is unlikely. Together with the modelling results, it can be concluded that chromium is incorporated in the octahedral sites of

magnetite. The octahedral components were fitted with a hyperfine magnetic field distribution (Fig. 11). The hyperfine magnetic field distribution was seen to broaden as the chromium content increases. This trend confirms that chromium is incorporated into octahedral sites of the active magnetite phase in HTS catalysts³³.

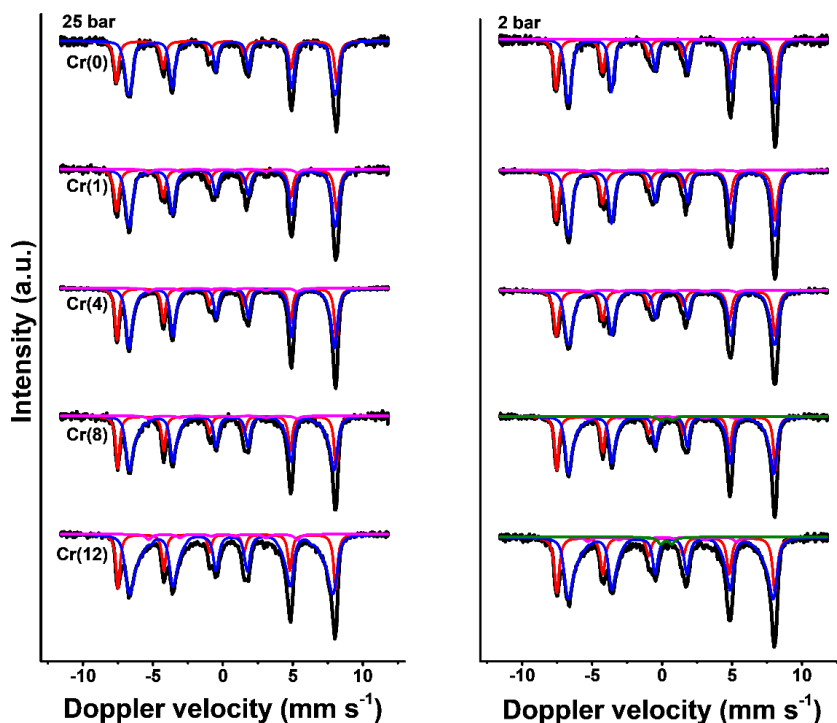


Figure 10. Mössbauer spectra of used catalysts at 25 bar (left) and 2 bar (right).

The octahedral IS values decreased with increasing chromium content in the used catalysts after treatment at 25 bar (Table. 6, Fig. 12). The IS value, which is 0.68 mm s^{-1} for the non-doped Cr(0) sample, decreases with increasing chromium content to 0.63 mm s^{-1} for the Cr(12) sample. The IS provides information about the oxidation state of Fe³⁷. The bulk IS value of the octahedral sites of magnetite of $\sim 0.67 \text{ mm s}^{-1}$ at room temperature is the average of fast electron hopping between Fe²⁺ and Fe³⁺ ions in octahedral sites³⁸. As this electron hopping is faster than the lifetime of an excited nuclear state in the Mössbauer experiment, the bulk IS value of $\sim 0.67 \text{ mm s}^{-1}$ represents an average 2.5+ state of the Fe ions in octahedral sites³⁸. IS values of $\sim 0.3 \text{ mm s}^{-1}$ are common for Fe³⁺-oxide species. Thus, the lower IS value observed upon

chromium doping indicates a higher than unity $\text{Fe}^{3+}/\text{Fe}^{2+}$ ratio in the octahedral sites^{39,40}.

Table 5. Catalysts after exposure to HTS conditions for 4 days at 25 bar.

Sample	Phase	IS (mm s ⁻¹)	QS (mm s ⁻¹)	H (T)	Γ (mm s ⁻¹)	Spectral contribution (%)
Cr(0)	$\text{Fe}_3\text{O}_4(\text{tet})$	0.26	-0.03	48.7	0.38	38
	$\text{Fe}_3\text{O}_4(\text{oct})$	0.68	-0.03	45.7† ^a	0.32	62
	$\alpha\text{-Fe}$	0.00*	0.00*	33.0* ^a	0.50*	1
Cr(1)	$\text{Fe}_3\text{O}_4(\text{tet})$	0.27	-0.03	48.6	0.43	37
	$\text{Fe}_3\text{O}_4(\text{oct})$	0.67	0.03	45.6†	0.37	62
	$\alpha\text{-Fe}$	0.00*	0.00*	33.0*	0.50*	1
Cr(4)	$\text{Fe}_3\text{O}_4(\text{tet})$	0.27	-0.02	48.6	0.43	37
	$\text{Fe}_3\text{O}_4(\text{oct})$	0.66	0.01	45.3†	0.38	62
	$\alpha\text{-Fe}$	0.00*	0.00*	33.0*	0.50*	2
Cr(8)	$\text{Fe}_3\text{O}_4(\text{tet})$	0.28	0.00	48.6	0.34	34
	$\text{Fe}_3\text{O}_4(\text{oct})$	0.64	-0.01	44.6†	0.32	61
	$\alpha\text{-Fe}$	0.00*	0.00*	33.0*	0.50*	2
	SPM	0.30*	0.86	-	0.50*	2
Cr(12)	$\text{Fe}_3\text{O}_4(\text{tet})$	0.28	-0.01	48.4	0.41	31
	$\text{Fe}_3\text{O}_4(\text{oct})$	0.63	-0.02	44.1†	0.40	64
	$\alpha\text{-Fe}$	0.00*	0.00*	33.0*	0.50*	3
	SPM	0.30*	0.80*	-	0.50*	2

^a Fixed values are marked with an asterisk (*), average values with a dagger (†).

^b Experimental uncertainties: IS \pm 0.01 mm s⁻¹, QS \pm 0.01 mm s⁻¹, line width: Γ \pm 0.01 mm s⁻¹, hyperfine magnetic field: \pm 0.1 T, spectral contribution: \pm 3%.

^c Small amounts of $\alpha\text{-Fe}$ were observed in all catalysts with no clear correlation to Cr content. The small SPM fraction present in some of the catalysts represents small particle magnetite.

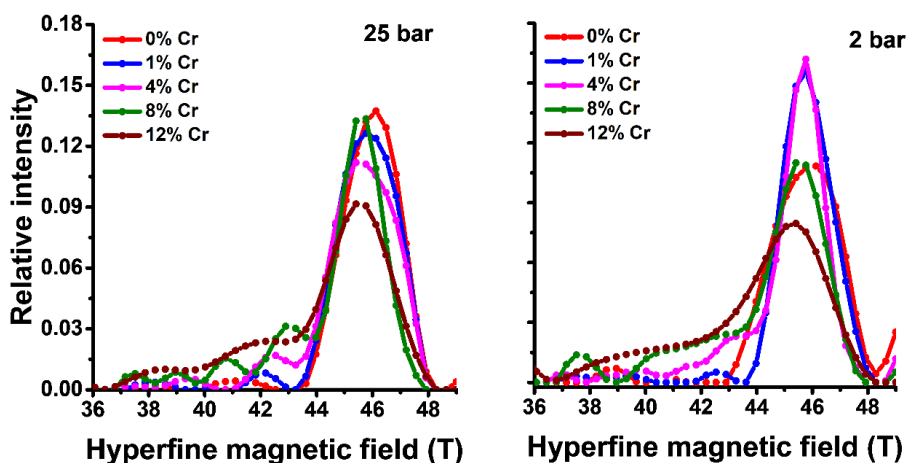


Figure 11. Hyperfine magnetic field distributions of the octahedral sites of magnetite fitted for Mössbauer spectra in Figure 10, 25 bar (left), 2 bar (right).

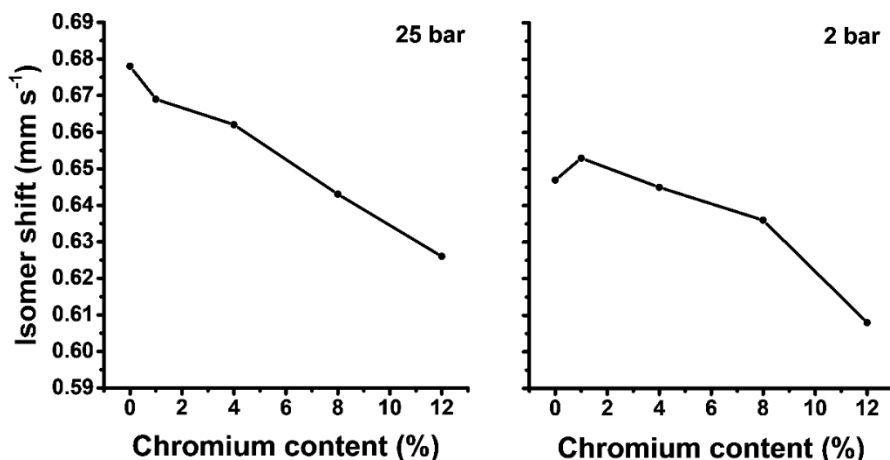


Figure 12. IS values of the octahedral sites of magnetite compared to chromium doping fitted for Mössbauer spectra in Figure 10, 25 bar (left), 2 bar (right).

Mössbauer spectra of catalysts treated for 4 days at 2 bar also show the presence of a magnetite phase (Fig. 10). A similar decreasing trend in IS values with chromium content (Fig. 12) was observed, indicating that chromium results in a higher $\text{Fe}^{3+}/\text{Fe}^{2+}$ ratio in octahedral sites of magnetite also at a relatively low reaction pressure. Although Figure 12 may suggest that the octahedral sites of catalysts treated at 2 bar contain a higher $\text{Fe}^{3+}/\text{Fe}^{2+}$ ratio than those treated at 25 bar, the differences are within the accuracy of the IS measurement ($\pm 0.01 \text{ mm s}^{-1}$). The broadening hyperfine magnetic field

distributions of the octahedral sites evident from Fig. 11 confirm the incorporation of chromium into the structure. Different from the 25 bar results, a decrease of the hyperfine magnetic fields of the tetrahedral sites with increasing chromium content can be observed. This decrease is however much smaller (0.7 T) compared to the decrease in hyperfine magnetic fields of octahedral sites (2.0 T). As discussed before, this difference indicates that particle sizes effects can most likely be excluded. An alternative explanation for the high tetrahedral hyperfine magnetic fields in the Cr(0) and Cr(1) samples is that some accidental oxidation occurred to maghemite, which typically has a hyperfine magnetic field of ~ 50 T³¹. Partially oxidised magnetite can explain the IS value of the Cr(0) sample below the bulk value of 0.67 mm s⁻¹ (Table 6).

Table 6. Hyperfine parameters determined by fitting Mössbauer spectra of used catalysts after exposure to HTS conditions for 4 days at 2 bar.

Sample	Phase	IS (mm s ⁻¹)	QS (mm s ⁻¹)	H (T)	Γ (mm s ⁻¹)	Spectral contribution (%)
Cr(0)	Fe ₃ O ₄ (tet)	0.28	-0.04	49.0	0.38	35
	Fe ₃ O ₄ (oct)	0.64	-0.00	45.6†	0.29	63
	α -Fe	0.00*	0.00*	33.0*	0.50*	2
Cr(1)	Fe ₃ O ₄ (tet)	0.28	-0.03	48.9	0.41	35
	Fe ₃ O ₄ (oct)	0.65	0.01	45.6†	0.39	62
	α -Fe	0.00*	0.00*	33.0*	0.50*	4
Cr(4)	Fe ₃ O ₄ (tet)	0.28	-0.03	48.7	0.34	35
	Fe ₃ O ₄ (oct)	0.65	-0.03	45.1†	0.32	61
	α -Fe	0.00*	0.00*	33.0*	0.50*	4
Cr(8)	Fe ₃ O ₄ (tet)	0.29	-0.01	48.5	0.33	33
	Fe ₃ O ₄ (oct)	0.64	-0.02	44.3†	0.33	65
	α -Fe	0.00*	0.00*	33.0*	0.50*	3
Cr(12)	Fe ₃ O ₄ (tet)	0.28	-0.01	48.3	0.34	27
	Fe ₃ O ₄ (oct)	0.61	-0.03	43.6†	0.41	70
	α -Fe	0.00*	0.00*	33.0*	0.50*	4

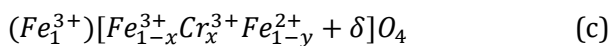
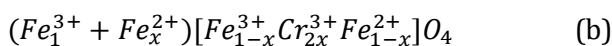
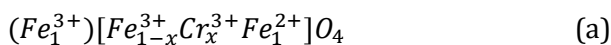
^a Fixed values are marked with an asterisk (*), average values with a dagger (†).

^b Experimental uncertainties: IS ± 0.01 mm s⁻¹, QS ± 0.01 mm s⁻¹, line width: $\Gamma \pm 0.01$ mm s⁻¹, hyperfine magnetic field: ± 0.1 T, spectral contribution: $\pm 3\%$.

^c Small amounts of α -Fe were observed in all catalysts with no clear correlation with the Cr content.

The modelled hyperfine parameters combined with the experimental data allow us to revisit the chromium incorporation models discussed in the introduction. Zhu and Wachs¹ conclude in their recent review on HTS catalysts

that Cr^{3+} replaces octahedral Fe^{3+} in structure a (see below). Robbins *et al.*¹³ suggested that Cr replaces an equal amount of octahedral Fe^{2+} and Fe^{3+} , which after charge compensation leads to structure b. Rangel *et al.*¹⁵ proposed that the octahedral site preference of Cr^{3+} prevents Fe^{3+} reduction during formation of the active phase. This structure is best represented as structure c. Based on the calculated hyperfine parameters discussed above, it can be concluded that the incorporation of chromium in octahedral positions, suggested in all models, will decrease the octahedral hyperfine magnetic field. The decreasing octahedral hyperfine magnetic field confirmed the incorporation of chromium into octahedral sites in our catalysts obtained after the HTS reaction at 2 and 25 bar. For structure a, the computed octahedral IS values predict an increasing trend with Cr doping. In contrast, these octahedral IS value should remain unaffected for structure b. The experimentally observed decreasing trend in octahedral IS values shows that these models do not accurately describe the cation distribution in the octahedral sites for our catalysts. Instead, the decreasing experimental octahedral IS values show that chromium incorporation in the octahedral sites results in an increased $\text{Fe}^{3+}/\text{Fe}^{2+}$ ratio as is the case in structure c. Since the tetrahedral sites are unaffected by Cr incorporation, structure c can be simplified as $\text{Fe}_{3-x(1-\delta)}\text{Cr}_x\text{O}_4$, where x describes the octahedral Cr content and δ the octahedral Fe vacancy content. Thus, chromium incorporation prevents Fe^{2+} formation during magnetite formation. The presence of such a $\text{Fe}_{3-x(1-\delta)}\text{Cr}_x\text{O}_4$ structure has not been demonstrated before in *in situ* formed HTS catalysts. The resulting partially oxidised chromium-doped magnetite structure had no negative effect on the high CO conversion typically associated with chromium doping.



The surface of the used catalysts was investigated by XPS analysis. The Fe 2p region of the catalysts after exposure to HTS conditions for 4 days at 2 and 25 bar is shown in Figure 13. The Fe $2\text{p}_{3/2}$ peak of Fe^{3+} -oxide containing hematite is typically found at a BE between 710.6 and 711.2 eV, while the Fe $2\text{p}_{3/2}$ peak of Wüstite Fe^{2+} -oxide appears at a slightly lower BE of 709.5 eV. The Fe $2\text{p}_{3/2}$

peak for the mixed valence $\text{Fe}^{3+}/\text{Fe}^{2+}$ -oxide containing magnetite usually appears between these values at BE = 710.6 eV ⁴¹. This makes identification of these Fe-oxides difficult from spectral fitting alone. Pure Fe^{3+} -phases like hematite can also be identified from the satellite peak in the Fe 2p region at BE = 719 eV, while Fe^{2+} -phases like Wüstite are characterised by a satellite peak at BE = 715.5 eV. A unique property of the Fe 2p region of magnetite is the absence of these Fe^{3+} and Fe^{2+} satellite peaks. The absence of satellite features at BE = 719 eV and 715.5 eV indicates that the surface is dominated by magnetite ⁴¹. This implies that there are no structural differences between the surface and the bulk.

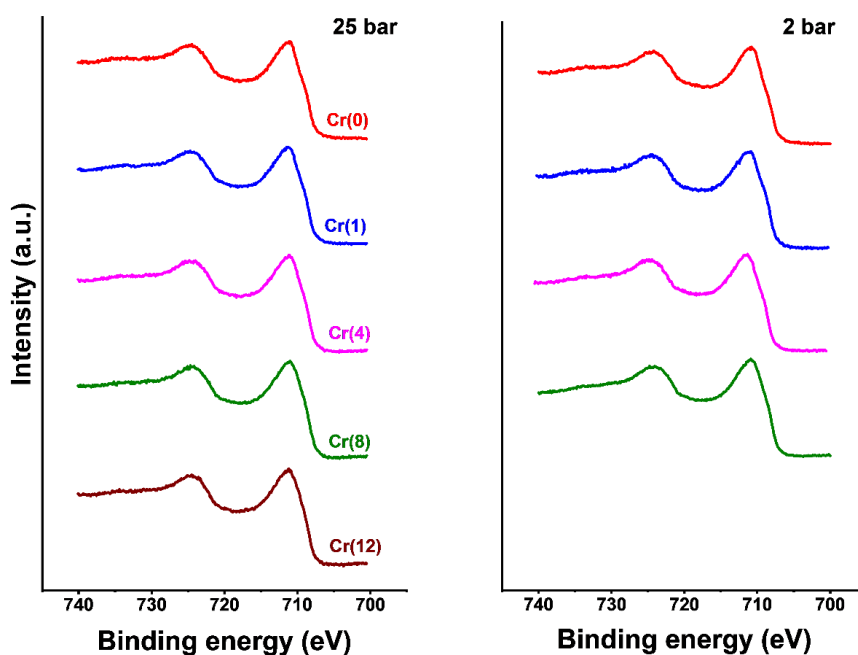


Figure 13. Fe 2p region of used catalysts after treatment for 4 days at 25 bar (left) and 2 bar (right).

The XPS spectra of the Cr 2p region are shown in Figure 14. Spectral fitting following a procedure from literature ⁵ revealed the presence of Cr^{3+} species with the Cr $2p_{3/2}$ peak at BE = 576.5-577 eV. A simple fitting model was chosen to prevent over-interpretation of the complex Cr 2p region. The absence of a sharp peak at BE = ~580 eV indicates that no Cr^{6+} is present on the catalysts surface after 4 days on stream, indicating the complete conversion of Cr^{6+} in the catalyst precursor to Cr^{3+} species. Chromium is present as Cr^{3+} in the activated catalysts.

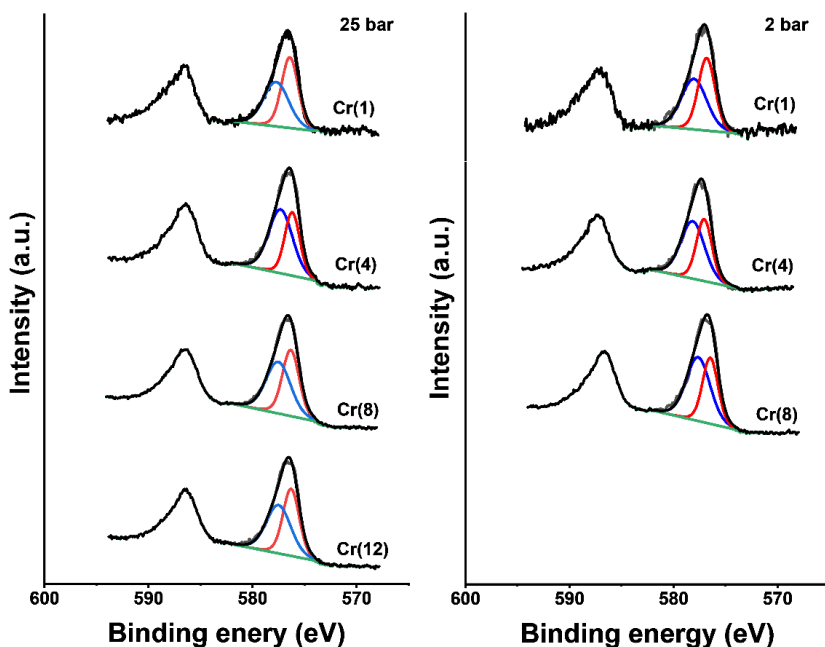


Figure 14. Cr 2p region of used catalysts after treatment for 4 days at 25 bar (left) and 2 bar (right).

2.4 CONCLUSIONS

HTS catalysts prepared via co-precipitation and calcination consist of hematite in which chromium can be doped ($\alpha\text{-Fe}_{2-x}\text{Cr}_x\text{O}_3$). Magnetite formation and over-reduction of the active magnetite phase to $\alpha\text{-Fe}$ occur at higher temperatures in chromium-containing samples. Chromium-doped magnetite was formed after exposure of the calcined samples to industrially relevant HTS conditions. The presence of chromium led to higher activity, irrespective of the reaction pressure (2 or 25 bar). Chromium doping led to smaller crystallite sizes, confirming its role as a structural promoter. Mössbauer spectra showed that chromium incorporates in octahedral sites of magnetite, preventing reduction of Fe^{3+} ions during magnetite formation. Interpretation of Mössbauer spectra was supported by DFT calculation of hyperfine parameters of various chromium and Fe-vacancy doped magnetite structures. The variations in the $\text{Fe}^{3+}/\text{Fe}^{2+}$ ratio due to Cr doping had no measurable effect on the CO conversion levels associated with Cr-doping. The structural characterisation shows that the active phase under industrial HTS conditions is best described by $\text{Fe}_{3-x}(1-$

$\delta\text{Cr}_x\text{O}_4$ structure, in which Cr^{3+} is doped in the octahedral sites and its presence during the formation of the active phase prevents Fe^{2+} formation, resulting in a partially oxidised structure compared to stoichiometric magnetite.

REFERENCES

- [1] M. Zhu; I.E. Wachs Iron-Based Catalysts for the High-Temperature Water-Gas Shift (HT-WGS) Reaction: A Review. *ACS catalysis* **2016**, *6*, 722-732.
- [2] D.W. Lee; M.S. Lee; J.Y. Lee; S. Kim; H.J. Eom; D.J. Moon; K.Y. Lee The review of Cr-free Fe-based catalysts for high-temperature water-gas shift reactions. *Catalysis Today* **2013**, *210*, 2-9.
- [3] D.S. Newsome The Water-Gas Shift Reaction. *Catalysis Reviews Science and Engineering* **1980**, *21*, 275-318.
- [4] M.V. Twigg *Catalyst handbook*; 2 ed.; 1989.
- [5] C.J. Keturakis; M. Zhu; E.K. Gibson; M. Daturi; F. Tao; A.I. Frenkel; I.E. Wachs Dynamics of CrO₃-Fe₂O₃ Catalysts during the High-Temperature Water-Gas Shift Reaction: Molecular Structures and Reactivity. *ACS catalysis* **2016**, *6*, 4786-4798.
- [6] D. Damma; P.G. Smirniotis Recent advances in iron-based high-temperature water-gas shift catalysis for hydrogen production. *Current Opinion in Chemical Engineering* **2018**, *21*, 103-110.
- [7] A. Khan; P.G. Smirniotis Relationship between temperature-programmed reduction profile and activity of modified ferrite-based catalysts for WGS reaction. *Journal of Molecular Catalysis A: Chemical* **2008**, *280*, 43-51.
- [8] G.S. Parkinson Iron oxide surfaces. *Surface Science Reports* **2016**, *71*, 272-365.
- [9] J.E. Kubsh; J.A. Dumesic In situ gravimetric studies of the regenerative mechanism for water-gas shift over magnetite: Equilibrium and kinetic measurements in CO₂/CO and H₂O/H₂ gas mixtures. *American Institute of Chemical Engineers* **1982**, *28*, 793-800.
- [10] G.K. Boreskov; T.M. Yurieva; A.S. Sergeeva Mechanism of the Conversion of Carbon Monoxide on Iron-Chromium Catalyst. *Kinet. Catal.* **1970**, *11*, 374-381.
- [11] S. Natesakhawat; X. Wang; L. Zhang; U.S. Ozkan Development of chromium-free iron-based catalysts for high-temperature water-gas shift reaction. *Journal of Molecular Catalysis A: Chemical* **2006**, *260*, 82-94.

- [12] M. Zhu; I.E. Wachs A perspective on chromium-Free iron oxide-based catalysts for high temperature water-gas shift reaction. *Catalysis Today* **2018**, *311*, 2-7.
- [13] M. Robbins; G.K. Wertheim; R.C. Sherwood; D.N.E. Buchanan MAGNETIC PROPERTIES AND SITE DISTRIBUTIONS IN THE SYSTEM $\text{FeCr}_2\text{O}_4\text{-Fe}_3\text{O}_4(\text{Fe}^{2+}\text{Cr}_{2-x}\text{Fe}^{3+x}\text{O}_4)$. *J. Phys. Chem. Solids* **1971**, *32*, 717-729.
- [14] H. Topsøe; M. Boudart Mössbauer Spectroscopy of CO Shift Catalysts promoted with Lead. *Journal of Catalysis* **1973**, *31*, 346-359.
- [15] M. do Carmo Rangel; R.M. Sassaki; F. Galembek Effect of chromium on magnetite formation. *Catalysis Letters* **1995**, *33*, 237-254.
- [16] M. Zhu; T.C.R. Rocha; T. Lunkenbein; A. Knop-Gericke; R. Schlögl; I.E. Wachs Promotion Mechanisms of Iron Oxide-Based High Temperature Water-Gas Shift Catalysts by Chromium and Copper. *ACS catalysis* **2016**, *6*, 4455-4464.
- [17] M. Zhu; P. Tian; R. Kurtz; T. Lunkenbein; J. Xu; R. Schlögl; I.E. Wachs; Y.F. Han Strong Metal-Support Interactions between Copper and Iron Oxide during the High-Temperature Water-Gas Shift Reaction. *Angewandte chemie* **2019**, *131*, 9181-9185.
- [18] M. Zhu; P. Tian; J. Chen; M.E. Ford; J. Xu; I.E. Wachs; Y.F. Han Activation and deactivation of the commercial-type $\text{CuO-Cr}_2\text{O}_3\text{-Fe}_2\text{O}_3$ high temperature shift catalyst. *American Institute of Chemical Engineers* **2019**, *66*, 1-6.
- [19] C. Pellerin; S.M. Booker Reflections on hexavalent chromium: health hazards of an industrial heavyweight. *Environmental Health Perspectives* **2000**, *108*, 402-407.
- [20] R.L. Mössbauer Kernresonanzfluoreszenz von Gammastrahlung in Ir^{191} . *Zeitschrift für Physik* **1958**, *151*, 124-143.
- [21] J. Xie; H.M. Torres Galvis; A.C.J. Koeken; A. Kirilin; A.I. Dugulan; M. Ruitenbeek; K.P. de Jong Size and Promoter Effects on Stability of Carbon-Nanofiber-Supported Iron-Based Fischer-Tropsch Catalysts. *ACS catalysis* **2016**, *6*, 4017-4024.
- [22] V.P. Santos; T.A. Wezendonk; J.J. Delgado Jaén; A.I. Dugulan; M.A. Nasalevich; H.U. Islam; A. Chojecki; S. Sartipi; X. Sun; A.A. Hakeem; A. C.J.Koeken; M. Ruitenbeek; T. Davidian; G.R. Meima; G. Sankar; F. Kapteijn; M. Makkee; J. Gascon Metal organic framework-mediated synthesis of highly active and stable Fischer-Tropsch catalysts. *Nature Communications* **2015**, *6*, 6451.

- [23] Ř. Rezníček; V. Chlan; H. Štěpánková; P. Novák Hyperfine field and electronic structure of magnetite below the Verwey transition. *PHYSICAL REVIEW B* **2015**, *15*, 125-134.
- [24] F. Meshkani; M. Rezaei Preparation of Mesoporous Chromium Promoted Magnetite Based Catalysts for High Temperature Water Gas Shift Reaction. *Industrial & Engineering Chemistry Research* **2015**, *45*, 1236-1242.
- [25] Z. Klencsár Mössbauer spectrum analysis by Evolution Algorithm. Nuclear Instruments and Methods in Physics Research Section B: Beam Interactions with Materials and Atoms **1997**, *129*, 527-533.
- [26] P. Blaha; K. Schwarz; G.K.H. Madsen; D. Kvasnicka; J. Luitz Wien2K. *Technische Universitat Wien* **2001**.
- [27] R. Řezníček; V. Chlan; H. Štěpánková; P. Novák; J. Żukrowski; A. Kozłowski; Z. Kałkol; Z. Tarnawski; J.M. Honig Understanding the Mössbauer spectrum of magnetite below the Verwey transition: *Ab initio* calculations, simulation, and experiment. *PHYSICAL REVIEW B* **2017**, *96*, 195124.
- [28] P. Novák; V. Chlan Contact hyperfine field at Fe nuclei from density functional calculations. *PHYSICAL REVIEW B* **2010**, *81*, 174412.
- [29] M. Zhu; Ö. Yalçın; I.E. Wachs Revealing structure-activity relationships in chromium free high temperature shift catalysts promoted by earth abundant elements. *Applied Catalysis B: Environmental* **2018**, *232*, 205-212.
- [30] T. Popa; G. Xu; T.F. Barton; M.D. Argyle High temperature water gas shift catalysts with alumina. *Applied Catalysis A: General* **2010**, *379*, 15-23.
- [31] R.M. Cornel; U. Schwertmann The Iron Oxides: Structures, Properties, Reacions, Occurences and Uses; 2003.pp. 155-156.
- [32] Ö. Özdemir; D.J. Dunlop; T.S. Berquó Morin transition in hematite: Size dependence and thermalhysteresis. *Geochemistry Geophysics Geosystems* **2008**, *9*, 1-12.
- [33] E. Murad; J. Cashion Mössbauer Spectroscopy of Environmental Materials and their Industrial Utilization; 2004.
- [34] G. Doppler; A.X. Trautwein; H.M. Ziethen Physical and Catalytic Properties of High-Temperature Water-Gas Shift Catalysts Based upon Iron-Chromium oxides. *Applied Catalysis* **1988**, *40*, 119-130.
- [35] G.K. Reddy; K. Gunasekara; P. Boolchand; P.G. Smirniotis Cr- and Ce-Doped Ferrite Catalysts for the High Temperature Water-Gas Shift

- Reaction: TPR and Mössbauer Spectroscopic Study. *Journal of Physical Chemistry C* **2011**, *115*, 920-930.
- [36] S. Nakamura; A. Fuwa Spin Order in FeCr_2O_4 Observed by Mössbauer Spectroscopy. *Physics Procedia* **2015**, *75*, 747-754.
- [37] F. is Menil Systematic trends of the ^{57}Fe Mössbauer isomer shifts in (FeO_n) and (FeF_n) polyhedra. Evidence of a new correlation between the isomer shift and the inductive effect of the competing bond T-X ($\rightarrow \text{Fe}$) (where X is O or F and T any element with a formal positive charge). *Journal of Physics and Chemistry of Solids* **1984**, *46*, 763-789.
- [38] C.A. Gorski; M.M. Scherer Influence of Magnetite Stoichiometry on Fe^{II} Uptake and Nitrobenzene Reduction. *Environmental Science and Technology* **2009**, *43*, 3675-3680.
- [39] Z. Klencsár; A. Ábrahám; L. Szabó; E.G. Szabó; S. Stichleutner; E. Kuzmann; Z. Homonnay; G. Tolnai The effect of preparation conditions on magnetite nanoparticles obtained via chemical co-precipitation. *Materials Chemistry and Physics* **2019**, *223*, 122-132.
- [40] C.E. Johnson; J.A. Johnson; H.Y. Hah; M. Cole; S. Gray; V. Kolesnichenko; P. Kucheryavy; G. Goloverda Mössbauer studies of stoichiometry of Fe_3O_4 : characterization of nanoparticles for biomedical applications. *Hyperfine Interactions* **2016**, *237*, 27-1-27-10.
- [41] T. Yamashita; P. Hayes Analysis of XPS spectra of Fe^{2+} and Fe^{3+} ions in oxide materials. *Applied Surface Science* **2008**, *254*, 2441-2449.

3

COPPER DOPING

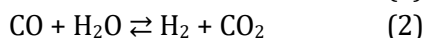
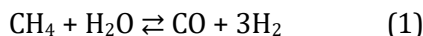
ABSTRACT

Copper promotion of chromium-doped iron oxide prepared via coprecipitation for high-temperature water-gas shift (WGS) catalysis is investigated. Low-temperature Mössbauer spectra demonstrate that copper doping delays hematite ($\alpha\text{-Fe}_2\text{O}_3$) formation in the fresh catalyst, favouring the formation of small crystallites of ferrihydrite ($\text{Fe}_5\text{HO}_8 \cdot 4 \text{H}_2\text{O}$). Catalysts are treated under industrial WGS conditions at 360 °C (activity evaluation) and 450 °C (ageing) at 2 and 25 bar. Mössbauer spectra show that chromium is incorporated in octahedral sites of the active magnetite (Fe_3O_4) phase, resulting in a partially oxidised structure. Copper doping did not affect the bulk magnetite structure of the activated catalyst, which points to the presence of a separate copper phase. Near-ambient pressure XPS shows that copper is in the metallic state. XPS of discharged catalysts evidenced that reaction at elevated pressure resulted in the surface reduction of Fe^{3+} to Fe^{2+} . Copper promotion enhances CO conversion under high-temperature WGS conditions.

This chapter was published as: M.I. Ariëns, L.G.A. van de Water, A.I. Dugulan, E. Brück, E.J.M. Hensen, *Journal of Catalysis*, 2022, 405, 391-403.

3.1 INTRODUCTION

Hydrogen is widely used in the production of bulk chemicals such as ammonia¹⁻². The International Energy Agency (IEA) estimates the global annual (2018) hydrogen production at 70 million tonnes³. Approximately 80% of hydrogen is produced from natural gas reforming (1), which is typically combined with a water-gas shift (WGS) step (2)^{1,4}.



In industry, the WGS reaction is usually performed in two stages⁴⁻⁹. High-temperature WGS (high-temperature shift, HTS) is typically performed at 350-450 °C using iron-oxide based catalysts. To achieve high CO conversion of this equilibrium-limited reaction, a second low-temperature step is included. This low-temperature shift (LTS) step is typically performed in the range of 190-250 °C using copper-based catalysts. In this configuration, the bulk of CO is removed during HTS with exit CO concentrations typically around 2-4% CO, while the residual CO is removed by LTS lowering the final CO concentration to 0.1-0.3%⁵.

Magnetite, the active phase of the iron-based HTS catalyst, is formed *in situ* via partial reduction of the hematite precursor^{6,10}. The dominant mechanism for the HTS reaction is of a regenerative redox type,¹¹ involving a Fe²⁺/Fe³⁺ redox couple which occupies octahedral sites in the bulk and at the surface of the inverse spinel structure of magnetite^{12,13}. In industrial catalysts, magnetite is promoted by chromium and copper to enhance CO conversion^{1,2}. Chromium is added for structural stabilisation of the catalyst, which forms upon activation a solid solution with magnetite. Chromium is known to incorporate into octahedral sites of magnetite. Robbins *et al.* showed that chromium is incorporated into the octahedral sites of magnetite prepared by heating a mixture of Fe₂O₃ and Cr₂O₃ to 1100 °C in a CO/CO₂ mixture, chromium replacing an equal amount of Fe²⁺ and Fe³⁺^{14,15}. Topsøe and Boudart confirmed that chromium incorporates into the octahedral sites of magnetite after treatment of chromium doped hematite structures under HTS conditions¹⁶. The authors suggested that replacement of equal amounts of Fe²⁺ and Fe³⁺ in octahedral sites, as indicated by Robbins *et al.*, is unlikely. We recently confirmed that chromium incorporation occurs in the octahedral sites of

magnetite, and showed that its presence results in a partially oxidised structure ($\text{Fe}_{3-x(1-\delta)}\text{Cr}_x\text{O}_4$)³². While earlier chemical promotion by chromium via the $\text{Cr}^{3+}/\text{Cr}^{6+}$ redox couple has also been postulated,^{2,17} a recent study has clearly demonstrated that the $\text{Cr}^{3+}/\text{Cr}^{6+}$ redox couple is not operative during WGS¹⁸. Copper acts as a chemical promoter and exists as Cu^{2+} in the fresh catalyst. Upon activation in a $\text{CO}/\text{H}_2\text{O}$ mixture Cu^{2+} segregates from the bulk to form Cu^0 nanoparticles⁶. The presence of metallic copper on activated catalysts was observed by several authors^{19,20} both in $\text{H}_2\text{O}/\text{CO}$ mixtures and under HTS conditions at ambient pressure. Zhu *et al.* showed that 30% of the Cu^0 surface is covered by an iron oxide layer due to strong metal-support interactions⁶. The iron oxide layer stabilises Cu^0 nanoparticles against aggregation and provides new active sites that facilitate CO adsorption and H_2O dissociation²¹. Recently, Zhu *et al.* discovered that Cu^0 nanoparticles are prone to deactivation via sintering in accelerated ageing tests at 600 °C under reverse WGS conditions.²²

Tightening regulations on the use of Cr^{6+} ²³ have led to exploration of alternative dopants to stabilise iron-based HTS catalysts^{2,18}. A rational design approach to achieve this goal is hampered by a lack of understanding of the exact role of chromium and copper dopants under industrially relevant conditions. An important limitation of previous works is that catalysts are typically not investigated after use under industrially relevant HTS conditions, for which three aspects are relevant. First, activity evaluation should involve gas mixtures containing H_2 , CO , CO_2 , and H_2O , representative of gas compositions used in an industrial plant⁵. Second, stability should be evaluated using dedicated accelerated testing protocols, because WGS catalysts typically operate for 3-5 years⁵. Third, catalyst testing should include the use of elevated pressure, as HTS is typically performed at pressures up to 80 bar in an industrial plant⁵.

The physico-chemical and catalytic properties of WGS catalysts are strongly determined by the preparation procedure²⁴. Popa *et al.* compared the long term stability of iron-chromium-copper catalysts prepared via ammonia-assisted co-precipitation of iron and chromium nitrates followed by copper impregnation to catalysts prepared by a single NaOH co-precipitation step²⁵. A separate impregnation step is usually used for loading copper, because copper forms water-soluble complexes with ammonia^{25,26}. Catalysts prepared by co-precipitation/impregnation exhibited more than two times higher initial

reaction rates than catalysts prepared via a single-step NaOH-assisted co-precipitation. However, after 100 hours at 400 °C and 16 hours at 500 °C in a H₂O/CO mixture at atmospheric pressure, the activity of the initially more active ammonia-precipitated catalyst was substantially lower than that of the NaOH-precipitated catalyst. Enhanced deactivation was explained by stronger copper sintering in the catalyst prepared by ammonia-assisted preparation, which contained a larger amount of copper nanoparticles at the surface²⁵. Meshkani and Rezaei showed that NaOH-assisted co-precipitation of iron, chromium, and copper nitrates provided catalysts stable up to 20 hours at 400 °C under HTS conditions at atmospheric pressure²⁴. Catalysts aged at pH 10 at 60 °C and calcined at 400 °C provided the highest CO conversion. Single-step NaOH-assisted co-precipitation is therefore regarded as a suitable method to obtain stable WGS catalysts.

Despite many studies^{6,22,24,27,28}, there are only few investigations involving characterisation of copper-chromium-doped iron-oxide-based HTS catalysts that were not exposed to air after prolonged activity evaluation under industrially relevant conditions, *i.e.*, elevated pressure, relevant gas compositions, and prolonged exposure times²⁰. Mössbauer spectroscopy is a powerful technique to study iron-based catalysts²⁹, including the incorporation of dopants in the active iron oxide phase³⁰. Mössbauer spectra can be deconvoluted into contributions of different iron species present in complex structures such as those present in tetrahedral and octahedral sites of magnetite³¹. This allows for detailed investigation of local dopant incorporation and its impact on the Fe²⁺/Fe³⁺ redox couple. Mössbauer spectroscopy has not been applied to investigate copper-doped HTS catalysts aged under close-to-industrial conditions. Incorporation of Cr³⁺ into the active Fe₃O₄ phase as studied using Mössbauer spectroscopy has been reported previously by us³². In the present study, we report on the promoting effect of copper in chromium-doped iron-oxide based HTS catalysts. Copper promotion at different dopant levels was investigated on catalysts treated for 96 hours under industrially relevant HTS conditions at 2 bar and 25 bar. The bulk catalyst was investigated by Mössbauer spectroscopy and x-ray diffraction (XRD), while the surface was analysed by x-ray photoelectron spectroscopy (XPS). Near-ambient pressure (NAP)-XPS was performed to investigate the copper dopant in a working catalyst.

3.2 EXPERIMENTAL

3.2.1 CATALYST PREPARATION

Catalysts were prepared via a co-precipitation/calcination procedure described elsewhere ²⁴. Briefly, appropriate amounts of iron, chromium, and copper nitrates were dissolved in deionised water at 60 °C under vigorous stirring. The pH was subsequently raised to pH 10 by the addition of a NaOH solution and the resulting slurry was aged at 60 °C for 1 h. After filtration and washing, the precipitates were dried at 150 °C for 3 h and calcined in static air at 400 °C for 4 h. Target compositions of $x = 0, 1, 3,$ and 5 wt. % CuO in α -Fe₂O₃/Cr₂O₃/CuO (92-x/8/x) wt. % were chosen to investigate the influence of copper doping. A reference 100% α -Fe₂O₃ catalyst was synthesised to differentiate between the influence of chromium and copper doping. Some aspects of the calcined reference α -Fe₂O₃ and CrCu(0) catalysts have been published elsewhere ³².

3.2.2 CATALYST CHARACTERISATION

XRD patterns were recorded on a PANalitical X'pert pro diffractometer equipped with a PW3064 spinner between $10^\circ < 2\theta < 100^\circ$, step size 0.008° , using Cu-K α radiation. Spectral fitting was performed with the HighScore Plus software. Crystallite sizes were calculated with the Scherrer equation. XRD measurements of used catalyst samples were performed under an argon atmosphere and special care was taken to not expose the used catalyst samples to air.

Transmission ⁵⁷Fe Mössbauer spectroscopy was performed with constant-acceleration or sinusoidal velocity spectrometers using a ⁵⁷Co(Rh) source. Velocity calibration is reported relative to α -Fe at room temperature. The source and the absorbing samples were kept at the same temperature during measurements. Spectra were fitted using the Moss Winn 4.0 program ³³. Used catalyst samples were kept under argon before and during measurement.

Nitrogen physisorption was performed on a Micromeritics 2420 ASAP instrument. Samples were outgassed prior to analysis with nitrogen at 140 °C for at least 1 h.

TEM images were acquired on a FEI Tecnai 20 (type Sphera) transmission electron microscope. Samples were suspended in a small quantity of acetone by sonication, followed by dispersion over a Cu grid containing holey carbon film. Particle size distributions were obtained by counting 200 particles per sample.

XPS measurements were performed on a Thermo Scientific K-Alpha spectrometer using an aluminium anode (Al K α = 1486.6 eV). The pressure in the measurement chamber was 2×10^{-8} mbar. Binding energy calibration was performed relative to adventitious carbon at BE = 285 eV. Spectral fitting was performed using CasaXPS software (version 2.3.19PR1.0). The samples were suspended on carbon tape and transferred to the spectrometer under vacuum. Fe 3p regions were fitted by a method adapted from Yamashita and Hayes³⁴. For the Fe³⁺ component, a linear background was used and a A(0.23,1,0)GL(10) line shape. The Fe 3p peak position was fixed between 55.9 – 56.1 eV, FWHM = 2.0 – 2.2 eV. These values are based on the fitting of a freshly calcined 8% Cr-doped catalyst with all iron present as Fe³⁺. For the Fe²⁺ component, a linear background was used and a A(0.23,1,0)GL(10) line shape. The peak position was not fixed, FWHM = 2.0 – 2.2 eV.

NAP-XPS measurements were performed on a lab-based SPECS system using Al K α irradiation (1486.6 eV). A thorough description of the machine is provided elsewhere³⁵. Spectra were recorded in a reaction cell positioned in the ultra-high vacuum chamber. CO gas was added via a mass flow controller, steam was added via a piezo valve. Experiments were performed at 0.76 mbar and pressure was controlled via a backpressure controller. Binding energy calibration was performed relative to lattice oxygen at BE = 529.7 eV.

3.2.3 CATALYTIC ACTIVITY MEASUREMENTS

Catalytic performance in the WGS reaction was determined in a parallel micro-reactor setup. In a typical test, 6 reactor tubes were charged with calcined catalyst and diluted with α -Al₂O₃. The reactors were purged with nitrogen and the temperature was raised to 250 °C at a rate of 2 °C min⁻¹. Steam was added via a HPLC pump after which dry reaction gas (55% H₂, 14% CO, 6% CO₂, and 25% N₂) was introduced to reach the desired composition (37% H₂, 9% CO, 4% CO₂, 17% N₂, 33% H₂O). The temperature was then ramped to 450 °C at a rate of 1 °C min⁻¹ and maintained for 24 h to activate and age the catalysts. After

initial ageing the temperature was lowered to 360 °C and activity was measured for 24 h. This was followed by an additional ageing step at 450 °C and activity measurement at 360 °C, each step for 24 h. Effluent products were analysed using a continuous gas analyser to allow calculation of CO conversion. After the reaction sequence was completed, the temperature was lowered to 250 °C and the H₂, CO, and CO₂ flows were switched to N₂. When no more CO was observed in the exit stream the steam addition was switched off and the catalysts were allowed to cool to room temperature in nitrogen flow. Samples were kept under a nitrogen atmosphere after the reaction before being stored in a glovebox under argon atmosphere prior to characterisation.

Some aspects of the used reference α -Fe₂O₃ and CrCu(0) catalysts have been published before ³².

3.3 RESULTS AND DISCUSSION

3.3.1 CALCINED CATALYSTS

Table 1. Physico-chemical properties of calcined catalysts.

Catalyst	d (nm) ^a	Surface area (m ² g ⁻¹) ^c	V _{tot} (cm ³ g ⁻¹)	Average pore size (nm)	CuO (wt. %) ^b	Cr ₂ O ₃ (wt. %) ^b
α -Fe ₂ O ₃ (ref)	44	45	0.22	19.9	0.0	0.0
CrCu(0)	25	110	0.25	9.2	0.0	7.5
CrCu(1)	*	135	0.21	6.3	1.0	8.5
CrCu(3)	*	132	0.20	6.0	3.1	8.4
CrCu(5)	*	157	0.23	5.9	5.1	8.4

^a Based on the Scherrer equation from the FWHM of the α -Fe₂O₃ (110) reflection. Patterns of too low quality for fitting marked with an asterisk.

^b Obtained by XRF analysis. Intended Cr₂O₃ and CuO concentrations differ slightly in some samples due to residual Na₂O (0.6-1.5 wt. %) ^{25,26}.

^c Surface area, pore volume, and pore diameter were determined by applying the Brunauer-Emmett-Teller (BET) method to N₂ adsorption isotherms.

Chromium-copper co-doped iron oxide catalysts were prepared via a method adapted from Meshkani and Rezaei ²⁴. Prior to characterisation, catalysts were dried at 150 °C followed by calcination at 400 °C in static air. The physico-chemical properties of the freshly calcined catalysts are shown in Table 1 and

the corresponding XRD patterns in Figure 1. All XRD reflections observed are consistent with the presence of hematite, irrespective of the dopant level. Formation of hematite is typical for (doped) iron oxide catalysts prepared via precipitation-calcination. Zhu *et al.*⁶ and Reddy *et al.*³⁶ mentioned the formation of hematite after calcination of similar materials. We observed that the position of the (110) reflection shifts to higher 2θ values for the chromium-doped samples in comparison to the $\alpha\text{-Fe}_2\text{O}_3$ reference (Fig. 1). This shift is caused by a contraction of the unit cell, pointing to the incorporation of chromium with a smaller ionic radius (Cr^{3+} , 62 pm) than the cations in the host structure (Fe^{3+} , 65 pm)³⁷. No significant shift in 2θ values was observed upon copper doping.

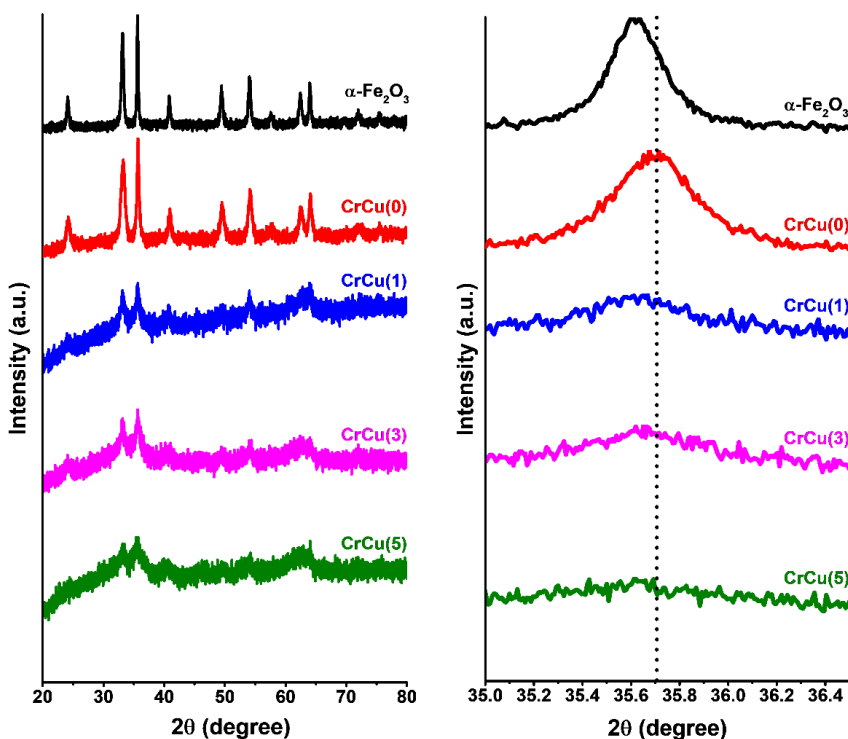


Figure 1. XRD patterns of freshly calcined catalysts. Complete patterns (left). Patterns zoomed in on (110) reflection (right).

Considerable line broadening was observed in the XRD patterns of the CrCu(1-5) samples compared to CrCu(0) and the $\alpha\text{-Fe}_2\text{O}_3$ (ref) sample. The line broadening in the XRD patterns confirms the formation of small crystallites. It should be noted that the absence of reflections due to other phases does not

exclude the presence of small (< 3-4 nm) or amorphous oxides of iron, chromium, or copper ³⁷.

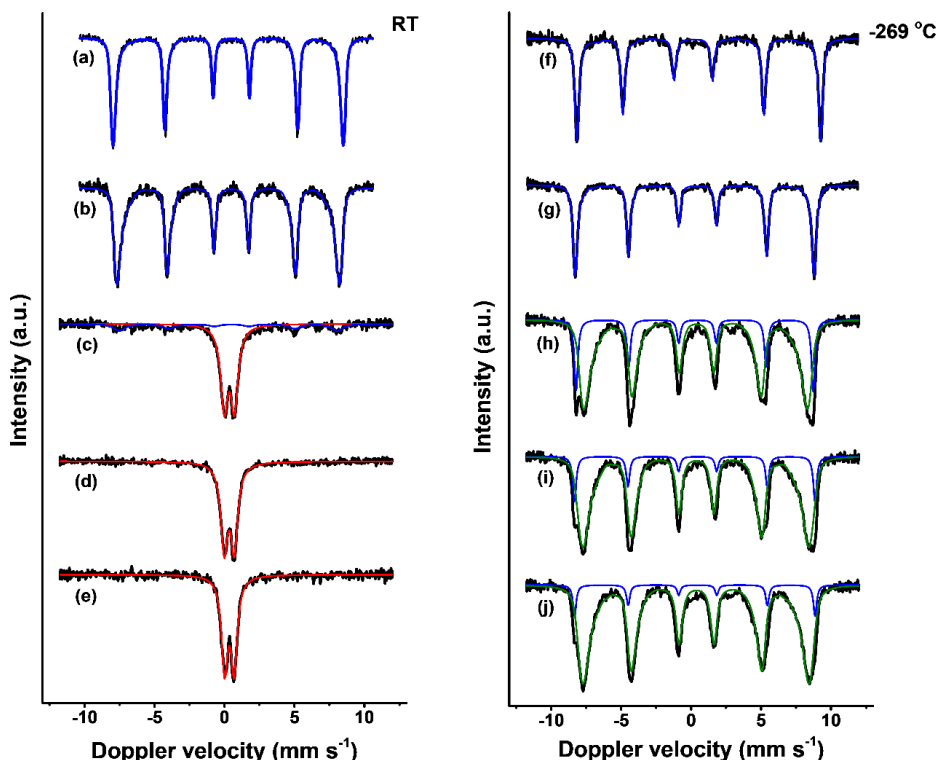


Figure 2. Mössbauer spectra of freshly calcined catalysts. Room temperature Mössbauer spectra of: (a) α - Fe_2O_3 (ref); (b) CrCu(0); (c) CrCu(1); (d) CrCu(3); (e) CrCu(5). Mössbauer spectra recorded at $-269\text{ }^\circ\text{C}$ of: (f) α - Fe_2O_3 (ref); (g) CrCu(0); (h) CrCu(1); (i) CrCu(3); and (j) CrCu(5).

Mössbauer spectroscopy was used to investigate in more detail the iron oxide phases in the calcined catalysts, including the possible formation of particles with a size smaller than a few nm not visible by XRD characterisation. Room-temperature Mössbauer spectra showed the presence of a magnetically split hematite phase ^{38,39} with a quadrupole splitting (QS) of -0.21 mm s^{-1} and an average hyperfine magnetic field between 50.5 T and 48.4 T in α - Fe_2O_3 , CrCu(0), and CrCu(1) (Fig. 2, Table 2). The superparamagnetic (SPM) doublet with an isomer shift (IS) of 0.37 mm s^{-1} , which is observed for all the CrCu(1-5) catalysts, indicates the presence of bulk iron oxide species with high spin Fe^{3+} in octahedral positions ²⁹.

Table 2. Mössbauer data of freshly calcined catalysts obtained at room temperature and -269 °C.

T (°C)	Catalyst	IS (mm s ⁻¹)	QS (mm s ⁻¹)	Hyperfine field (T)	Γ (mm s ⁻¹)	Phase	(%) ^c
RT	α-Fe ₂ O ₃ (ref)	0.38	-0.23	50.5†	0.23	α-Fe ₂ O ₃	100
	CrCu(0)	0.38	-0.21	48.5†	0.25	α-Fe ₂ O ₃	100
	CrCu(1)	0.35	0.72	-	0.62	Fe ³⁺ SPM	78
		0.39	-0.24	48.4	0.98	α-Fe ₂ O ₃	22
	CrCu(3)	0.34	0.71	-	0.59	Fe ³⁺ SPM	100
CrCu(5)	0.35	0.68	-	0.57	Fe ³⁺ SPM	100	
-269 °C	α-Fe ₂ O ₃ (ref)	0.35	0.40	53.6†	0.28	α-Fe ₂ O ₃	100
	CrCu(0)	0.36	-0.21	52.7†	0.26	α-Fe ₂ O ₃	100
	CrCu(1)	0.35	-0.20	52.7	0.30	α-Fe ₂ O ₃	22
		0.36	-0.06	48.1	0.45	Fe ₅ HO ₈ · 4 H ₂ O	78
	CrCu(3)	0.36	-0.21	53.4	0.29	α-Fe ₂ O ₃	14
0.36		-0.04	48.9	0.48	Fe ₅ HO ₈ · 4 H ₂ O	86	
CrCu(5)	0.37	-0.21	53.4	0.27	α-Fe ₂ O ₃	9	
	0.37	-0.04	48.6	0.47	Fe ₅ HO ₈ · 4 H ₂ O	91	

^a Fixed values are marked with an asterisk (*), average values of distribution fits with a dagger (†).

^b Experimental uncertainties: IS ± 0.01 mm s⁻¹, QS ± 0.01 mm s⁻¹, line width: Γ ± 0.01 mm s⁻¹, hyperfine magnetic field: ± 0.1 T, spectral contribution: ± 3%.

^c Spectral contribution.

In Mössbauer spectra measured at -269 °C (Fig. 2), magnetic splitting was regained and two sextets were observed for the CrCu(1-5) catalysts, while only one sextet was observed for the α-Fe₂O₃(ref) and CrCu(0) catalysts. The sextets with QS = -0.21 mm s⁻¹ (Table 2), prevalent for all catalysts irrespective of the dopant level, confirm the presence of hematite ⁴⁰. In the Mössbauer spectrum of α-Fe₂O₃(ref), a QS of 0.40 mm s⁻¹ was observed, which indicates that hematite underwent the Morin transition ³⁸. The Morin transition is a magnetic phase transition inherent to non-doped hematite, which typically occurs between -12 °C and -32 °C characterised by spin canting around the c-axis ³⁹. In Mössbauer spectra of CrCu(1-5), two sextets were observed indicating the presence of a second phase besides hematite. IS values of 0.37 mm s⁻¹ and QS =

-0.04 mm s⁻¹ and a hyperfine magnetic field between 48 T and 49 T point to the presence of the 6-line ferrihydrite (Fe₅HO₈·4 H₂O) phase⁴¹. This shows that the SPM phase observed in the room-temperature Mössbauer spectra contains hematite as well as small particles of ferrihydrite. Copper doping led to a decreased spectral contribution of hematite from 100% in the copper-free catalysts to 22% in CrCu(1) (Table 2). The hematite fraction further decreased from 22% to 9% with increasing Cu content going from CrCu(1) to CrCu(5), which shows that copper has an inhibiting effect on hematite formation during calcination. This inhibiting effect indicates that copper is incorporated in the bulk ferrihydrite structure. The incorporation of Cu²⁺ ions into a solid solution of the Fe-Cr-Cu mixed-oxide catalyst precursor during calcination was confirmed in a recent high-resolution XANES study⁴². XRD analysis was not able to provide solid evidence for this due to the absence of ferrihydrite reflections in the XRD patterns, resulting from the small size of the Fe₅HO₈·4 H₂O crystallites.

3.3.2 CATALYTIC ACTIVITY MEASUREMENTS

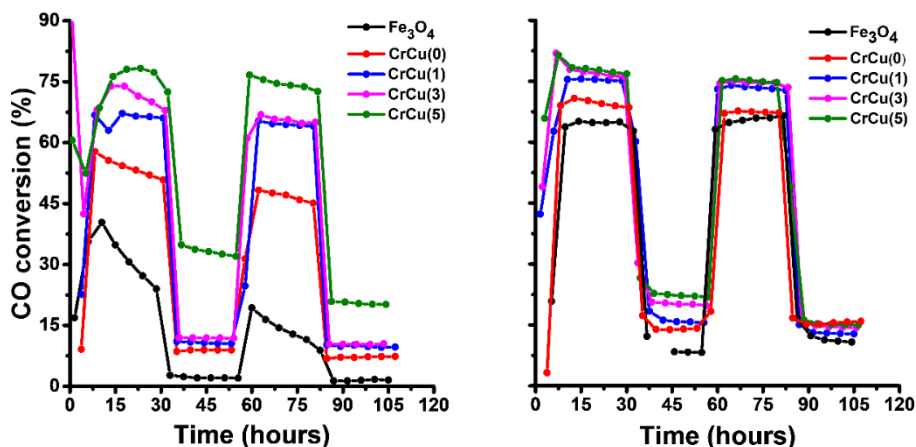


Figure 3. CO conversion over time at 2 bar (left) and 25 bar (right), (37% H₂, 9% CO, 4% CO₂, 17% N₂, 33% H₂O, 360-450 °C). The α -Fe₂O₃ phase present in the α -Fe₂O₃(ref) catalyst is transformed into Fe₃O₄ during the reaction. CO conversion of the Fe₃O₄ and CrCu(0) reference catalysts at 25 bar were recorded in a separate run than the samples characterised in the next section.

The catalytic performance of the obtained samples was evaluated in a plug-flow reactor under industrially relevant HTS conditions (37% H₂, 9% CO, 4%

CO₂, 17% N₂, 33% H₂O). The tests were conducted at 2 and 25 bar to investigate the promotional effect of copper doping on CO conversion at near ambient (2 bar) as well as an industrially relevant pressure (25 bar). Freshly calcined catalysts were initially aged under HTS conditions at 450 °C for 24 hours followed by activity measurements for 24 hours at 360 °C (Fig. 3). The catalysts were then further aged for 24 hours at 450 °C followed by activity measurement for 24 hours at 360 °C.

CO conversion levels during activity measurements at 2 bar are shown in figure 3. Higher CO conversion was observed after initial ageing of the CrCu(0) catalyst compared to the non-doped Fe₃O₄ catalyst. The better performance of the chromium-doped catalyst is usually explained by less extensive sintering of high-surface-area iron-based HTS catalysts^{1,2}. Copper doping increased the CO conversion compared to CrCu(0). The increase in CO conversion was most pronounced for the CrCu(5) catalyst. The promoting effect of copper is typically attributed to the formation of Cu⁰ nanoparticles on the surface of the bulk chromium-doped magnetite catalyst^{6,21,22}. Cu⁰ particles partially covered by an iron oxide over-layer can facilitate water dissociation, resulting in sites that are more active than individual copper and iron oxide sites²¹. The activity of CrCu(5) decreased after the second thermal ageing step.

The catalysts were also evaluated for their HTS performance at 25 bar. These experiments confirmed that copper doping led to a higher CO conversion after initial ageing compared to CrCu(0) and α -Fe₂O₃(ref) (referred to as Fe₃O₄ from this point) (Fig. 3). Thus, the promoting effect of copper is not strongly dependent on the pressure. We also observed that the second ageing step did not affect the CO conversion of the CrCu(0) catalyst (Fig. 3). The positive effect of copper on the CO conversion decreased and CO conversion levels were similar to that of the CrCu(0) sample. Deactivation of the copper doped catalysts can be the result of sintering of the Cu⁰ nanoparticles²², resulting in fewer active sites.

3.3.3 USED CATALYST

The surface and bulk structure of the used catalysts was investigated by XRD, Mössbauer spectroscopy and XPS. XRD patterns of catalysts treated at 25 bar contain 2 θ reflections at 29.9°, 35.3°, 42.9°, 53.3°, 56.8°, 62.4°, 70.8°, 73.9°, 86.6°, 89.5°, and 94.4° (Fig. 4), which point to the presence of either magnetite

(Fe_3O_4) or maghemite ($\gamma\text{-Fe}_2\text{O}_3$)⁴³. Since magnetite and maghemite possess a similar inverse spinel structure, no distinction can be made by XRD analysis alone⁴⁴. No reflections due to copper- or chromium-containing phases were observed, which is in line with the expected size of the Cu^0 nanoparticles below a few nm⁶ and the absence of separate chromium oxide phases.

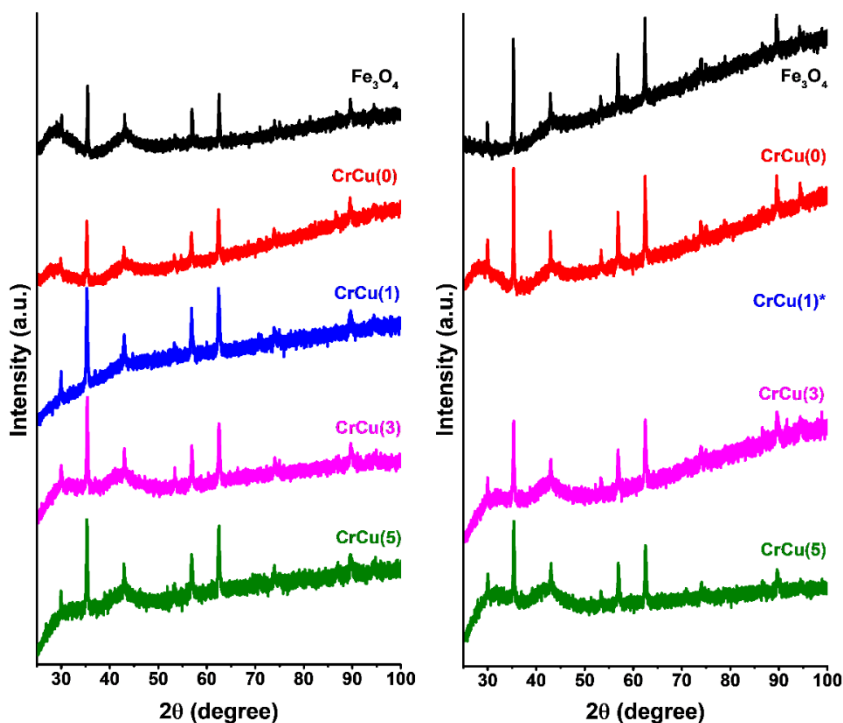


Figure 4. XRD patterns after treatment under HTS conditions for 96 hours at 2 bar (left) and 25 bar (right). *no XRD pattern for CrCu(1) after 25 bar was recorded.

Room-temperature Mössbauer spectra demonstrate that magnetite was formed during operation under HTS conditions (Fig. 5). Detailed information on local dopant incorporation, including their location in tetrahedral and octahedral sites, can be obtained by deconvoluting the Mössbauer spectra into sub-spectra representing the various sites^{31,45}. IS and hyperfine magnetic field values of respectively $\sim 0.28 \text{ mm s}^{-1}$ and $\sim 48.5 \text{ T}$ were observed for the tetrahedral sites, irrespective of the presence of copper and chromium (Table 3). These values are similar with those reported by Reddy *et al.*²⁸ for used HTS catalysts under atmospheric conditions and show that dopants are not

incorporated in tetrahedral sites. The IS value of the octahedral sites decreased from 0.68 mm s⁻¹ for the non-doped Fe₃O₄ catalysts to 0.64 mm s⁻¹ for the CrCu(0-5) samples (Table 3). This decrease from the bulk value of ~0.67 mm s⁻¹ points to partially oxidised octahedral sites upon chromium incorporation^{32,44,46}. The higher than unity Fe³⁺/Fe²⁺ ratio in the octahedral sites upon chromium doping can be the result of the octahedral site preference of Cr³⁺ which during magnetite formation hinders Fe³⁺ reduction⁴⁷. Very similar IS values were observed for the CrCu(0), CrCu(1), CrCu(3) and CrCu(5) samples, indicating that copper has no effect on the average iron oxidation state in the octahedral sites in the activated catalysts. The similar IS values suggest that no copper is incorporated into the octahedral sites, since the incorporation of divalent ions like Cu²⁺ is expected to replace divalent Fe²⁺ ions resulting in a more Fe³⁺-like IS in the octahedral sites. The absence of copper in octahedral sites contradicts an earlier Mössbauer study by Reddy *et al.*²⁸. These authors based their conclusion that copper is incorporated into the octahedral sites of magnetite on a decrease in the ratio of the octahedral/tetrahedral site spectral contributions. A decreased ratio of the spectral contribution of the octahedral and tetrahedral sites can however also indicate the presence of a maghemite phase, which can form upon exposure of the active magnetite phase to air. The spectral contribution of maghemite overlaps with the tetrahedral site contribution of magnetite because of its similar hyperfine magnetic field. QS values of ~0.00 mm s⁻¹ were observed for both the tetrahedral and octahedral sites, which is typical for magnetite (Table. 3)⁴¹. The hyperfine magnetic field of the octahedral sites decreased from 45.7 T to ~44.3 T for the chromium-doped catalysts (Table 3, Fig. 5). The deviation of the hyperfine magnetic field from the bulk value of 46.0 T confirms that chromium is incorporated in the octahedral sites⁴⁸. No significant decrease in hyperfine magnetic field values was observed for the samples that contained copper (Table 3, Fig. 5). Thus, copper does not remain included in the iron oxide phase and the decreased hyperfine magnetic field arises solely from chromium incorporation. Particle size effects on the hyperfine magnetic field values are unlikely, because the decrease only occurs for the octahedral sites. The Mössbauer parameters for the tetrahedral sites remain the same. These results point to the removal of Cu²⁺ from the bulk iron oxide structure upon activation of the catalyst⁶. The absence of copper in the bulk Fe_{3-x(1-δ)Cr_xO₄} phase after exposure to HTS conditions for 96 hours at 25 bar is in line with the observation of a separate Cu⁰ phase by Zhu *et al.*⁶ and Zhu *et al.*²², who tested their catalysts at ambient pressure in a H₂O/CO mixture and under reverse WGS conditions, respectively.

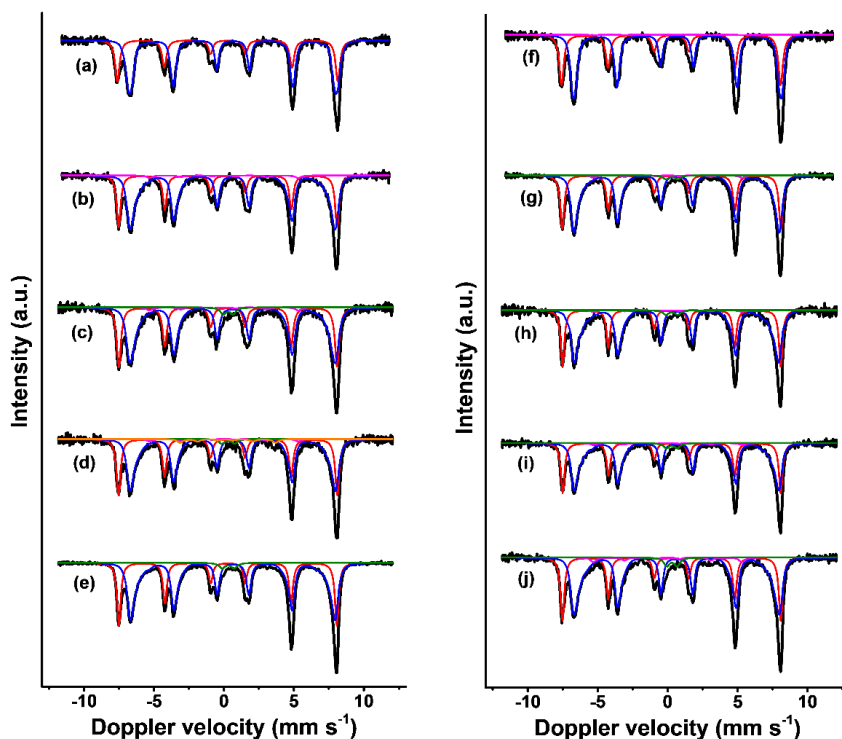


Figure 5. Mössbauer spectra recorded at room temperature of catalysts treated under HTS conditions for 96 hours at 2 bar: (a) α - Fe_2O_3 (ref); (b) CrCu(0); (c) CrCu(1); (d) CrCu(3); (e) CrCu(5); and 25 bar: (f) α - Fe_2O_3 (ref); (g) CrCu(0); (h) CrCu(1); (i) CrCu(3); (j) CrCu(5). Spectral contributions of the tetrahedral and octahedral sites of magnetite are shown in red and blue respectively. Minor spectral contributions indicating the presence of an α -Fe (magenta), and Fe_3C (orange) were observed, indicating some over-reduction of the active catalyst with no apparent trend with respect to the presence of dopants or pressure. The Fe^{3+} SPM phase (green) indicates the presence of a small particle magnetite phase.

Table 3. Mössbauer parameters of catalysts exposed to HTS conditions for 96 hours at 25 bar.

Catalyst	IS (mm s ⁻¹)	QS (mm s ⁻¹)	Hyperfine field (T)	Γ (mm s ⁻¹)	Phase	Spectral contribution (%)
Fe ₃ O ₄ ^a	0.26	-0.03	48.7	0.38	Fe ₃ O ₄ (tet)	37
	0.68	-0.03	45.7†	0.32	Fe ₃ O ₄ (oct)	62
	0.00*	0.00*	33.0*	0.50*	α-Fe	1
CrCu(0)	0.28	0.00	48.6	0.34	Fe ₃ O ₄ (tet)	35
	0.64	-0.01	44.6†	0.32	Fe ₃ O ₄ (oct)	61
	0.00*	0.00*	33.0*	0.50*	α-Fe	2
	0.30*	0.86	-	0.50*	Fe ³⁺ SPM	2
CrCu(1)	0.28	0.01	48.5	0.31	Fe ₃ O ₄ (tet)	33
	0.64	-0.02	44.1†	0.30	Fe ₃ O ₄ (oct)	63
	0.00*	0.00*	33.0*	0.50*	α-Fe	2
	0.30*	0.83	-	0.50*	Fe ³⁺ SPM	2
CrCu(3)	0.29	0.00	48.4	0.32	Fe ₃ O ₄ (tet)	34
	0.64	-0.03	44.2†	0.30	Fe ₃ O ₄ (oct)	62
	0.00*	0.00*	33.0*	0.50*	α-Fe	2
	0.30*	0.76	-	0.50*	Fe ³⁺ SPM	2
CrCu(5)	0.28	-0.00	48.5	0.33	Fe ₃ O ₄ (tet)	34
	0.65	-0.02	44.3†	0.30	Fe ₃ O ₄ (oct)	59
	0.00*	0.00*	33.0*	0.50*	α-Fe	4
	0.30*	0.73	-	0.50*	Fe ³⁺ SPM	3

^a Fe₃O₄ corresponds to activated α-Fe₂O₃(ref)

^b Fixed values are marked with an asterisk (*), average values of distribution fits with a dagger (†).

^c Experimental uncertainties: IS ± 0.01 mm s⁻¹, QS ± 0.01 mm s⁻¹, line width: Γ ± 0.01 mm s⁻¹, hyperfine magnetic field: ± 0.1 T, spectral contribution: ± 3%.

After treatment for 96 hours at 2 bar, the XRD reflections are similar to those of catalysts treated at 25 bar (Fig. 4). Again, no reflections due to separate copper or chromium species were observed. Mössbauer spectra (Fig. 5, Table 4) showed the same decreased IS values from the bulk value to 0.64 mm s⁻¹ in the CrCu(0-5) catalysts. For the Fe₃O₄ reference catalyst, an IS of 0.64 mm s⁻¹ was observed. The unexpected decrease in IS, together with a hyperfine magnetic field of 49.0 T observed for the tetrahedral sites, points to accidental oxidation, resulting in the formation of a small amount of maghemite and partially oxidised magnetite. Since maghemite is known to transform into magnetite under WGS conditions⁸, it is unlikely that this is the result of the process conditions. Incorporation of chromium in the octahedral sites of

magnetite was confirmed by decreased hyperfine magnetic field values from the value of 45.6 T CrCu(0-5) samples compared to the reference Fe₃O₄ catalyst (Table 4). The catalysts treated at 2 bar also show no effect of copper on the hyperfine magnetic field, indicating that copper was not incorporated into the Fe_{3-x(1-δ)Cr_xO₄ structure, in good agreement with earlier observations^{6,21,22}. These results show that the incorporation of chromium into the octahedral sites resulting in partial oxidation and the expulsion of copper from the bulk structure are independent of pressure.}

Table 4. Mössbauer parameters of catalysts exposed to HTS conditions for 96 hours at 2 bar.

Catalyst	IS (mm s ⁻¹)	QS (mm s ⁻¹)	Hyperfine field (T)	Γ (mm s ⁻¹)	Phase	Spectral contribution (%)
Fe ₃ O ₄ ^{a,+}	0.28	-0.04	49.0	0.38	Fe ₃ O ₄ (tet)	35
	0.64	-0.00	45.6†	0.29	Fe ₃ O ₄ (oct)	63
	0.00*	0.00*	33.0*	0.50*	α-Fe	2
CrCu(0)	0.29	-0.01	48.5	0.33	Fe ₃ O ₄ (tet)	33
	0.64	-0.02	44.3†	0.33	Fe ₃ O ₄ (oct)	64
	0.00*	0.00*	33.0*	0.50*	α-Fe	3
CrCu(1)	0.29	-0.00	48.5	0.37	Fe ₃ O ₄ (tet)	35
	0.64	-0.03	44.4†	0.36	Fe ₃ O ₄ (oct)	60
	0.00*	0.00*	33.0*	0.50*	α-Fe	2
	0.30*	0.70	-	0.50*	Fe ³⁺ SPM	3
CrCu(3)	0.28	0.00	48.6	0.35	Fe ₃ O ₄ (tet)	35
	0.64	0.00	44.6†	0.35	Fe ₃ O ₄ (oct)	58
	0.00*	0.00*	33.0*	0.50*	α-Fe	2
	0.30*	0.91	-	0.50*	Fe ³⁺ SPM	2
	0.19*	0.18	21.2*	0.50*	Fe ₃ C	3
CrCu(5)	0.29	-0.01	48.4	0.32	Fe ₃ O ₄ (tet)	35
	0.64	-0.01	44.3†	0.34	Fe ₃ O ₄ (oct)	63
	0.30*	0.86	-	0.50*	Fe ³⁺ SPM	2

^a Fe₃O₄ corresponds to activated α-Fe₂O₃(ref)

^b Fixed values are marked with an asterisk (*), average values of distribution fits with a dagger (†).

^c Experimental uncertainties: IS ± 0.01 mm s⁻¹, QS ± 0.01 mm s⁻¹, line width: Γ ± 0.01 mm s⁻¹, hyperfine magnetic field: ± 0.1 T, spectral contribution: ± 3%.

+ The decreased IS for the reference Fe₃O₄ catalyst is likely due to accidental oxidation.

Crystallite sizes of calcined α-Fe₂O₃ and used Fe₃O₄ catalysts obtained from XRD analysis are shown in Table 5. The average crystallite size of discharged

catalysts after treatment at 2 bar is 71 nm for the non-doped Fe_3O_4 catalyst, which implies significant sintering compared to the average crystallite size of 44 nm of the fresh $\alpha\text{-Fe}_2\text{O}_3(\text{ref})$ catalyst. The crystallite size of $\text{CrCu}(0)$ increases from 25 nm in the fresh state to 41 nm after reaction at 2 bar for 96 hours. The lower degree of sintering of $\text{CrCu}(0)$ can be attributed to chromium doping, which is known to prevent thermal agglomeration^{1,2}. Crystallite sizes of freshly calcined copper-doped samples could not be determined due to the broadness of XRD reflections caused by the presence of a ferrihydrite phase that is either amorphous or has very small crystallite size (Fig. 1). After treatment at 2 bar, average crystallite sizes of 39 nm in $\text{CrCu}(1)$, 47 nm in $\text{CrCu}(3)$, and 46 nm in $\text{CrCu}(5)$ were observed. These crystallite sizes are similar to those of the $\text{CrCu}(0)$ catalyst and lower than the crystallite sizes of the non-doped Fe_3O_4 reference catalyst. The lower crystallite size can be attributed to chromium incorporation, stabilising the high surface area of the catalyst^{1,2}. These results show that, while the presence of copper resulted in smaller crystallites of the calcined catalyst, copper did not affect the crystallite size during the HTS reaction. This provides further evidence of the expulsion of copper from the bulk structure in line with the promotion mechanism of a separate Cu^0 phase proposed by Zhu *et al.*⁶. Catalysts treated at 25 bar showed a similar trend in average crystallite sizes with the exception of $\text{CrCu}(0)$ (Table 5). We believe that this is an outlier, because there has been no prior evidence for the role of Cu as a structural promoter. Furthermore, this effect is not observed for the catalysts aged at 2 bar. The decrease in crystallite size for the chromium-doped catalysts confirms that chromium acts as a structural stabiliser^{1,2}. The similar crystallite sizes measured for the copper-doped samples together with increased CO conversion are in line with a chemical promotion mechanism.

TEM was used to explore the particle sizes of the various samples in more detail (Fig. 6). The average crystallite sizes of the copper-doped catalysts after treatment at 25 bar were very similar (i.e., 52 nm for $\text{CrCu}(1)$, 50 nm for $\text{CrCu}(3)$, and 48 nm for $\text{CrCu}(5)$), close to the values derived by XRD. The similar average crystallite sizes confirm that the promoting effect of copper doping is of a chemical nature.

Table 5. Average crystallite sizes of spent catalysts after treatment under HTS conditions for 96 hours as determined by XRD analysis.

	Fresh ^a	2 bar	25 bar
Fe ₃ O ₄	44 ^b	71 ^b	74
CrCu(0)	25	41	64
CrCu(1)	*	39	n.m.
CrCu(3)	*	47	43
CrCu(5)	*	46	43

^a Freshly calcined catalysts.

^b Calculated with the Scherrer equation from the FWHM of the α -Fe₂O₃ (110) reflection and the Fe₃O₄ (311) reflection.

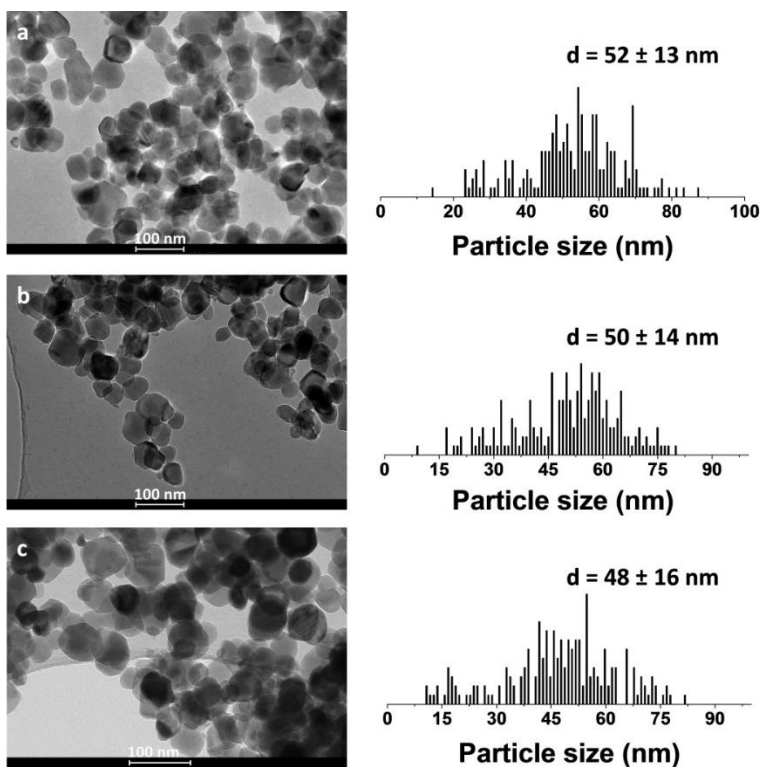


Figure 6. TEM images and particle size distributions of discharged copper-doped catalysts after treatment under HTS conditions for 96 hours at 25 bar: (a) CrCu(1); (b) CrCu(3); and (c) CrCu(5).

XPS measurements were performed to investigate the surface structure of the used catalysts. The Fe 2p XPS spectra of catalysts treated at 2 bar and 25 bar are shown in Figure 7. The typical satellite feature due to Fe³⁺ at a binding

energy of 719 eV was absent for all samples, which is in line with the predominance of magnetite ⁶ as followed from Mössbauer spectroscopy and XRD. Surface Fe³⁺/Fe²⁺ ratios were approximated by fitting the Fe 3p region (Fig. 8) according to the method proposed by Yamashita and Hayes ³⁴. A lower Fe³⁺/Fe²⁺ ratio was observed for all catalysts treated at 25 bar compared to those treated at 2 bar. The exception is CrCu(5), which exhibited similar Fe³⁺/Fe²⁺ ratios after the two experiments. The more ferrous-like surface of the catalyst after treatment at elevated pressure can be explained by the reducing nature of the gas mixture. In the Cr 2p region (Fig. 9), the peak at a BE of 577 eV indicates that chromium is present as Cr³⁺ ⁴⁹, which is in line with observations by others ⁶.

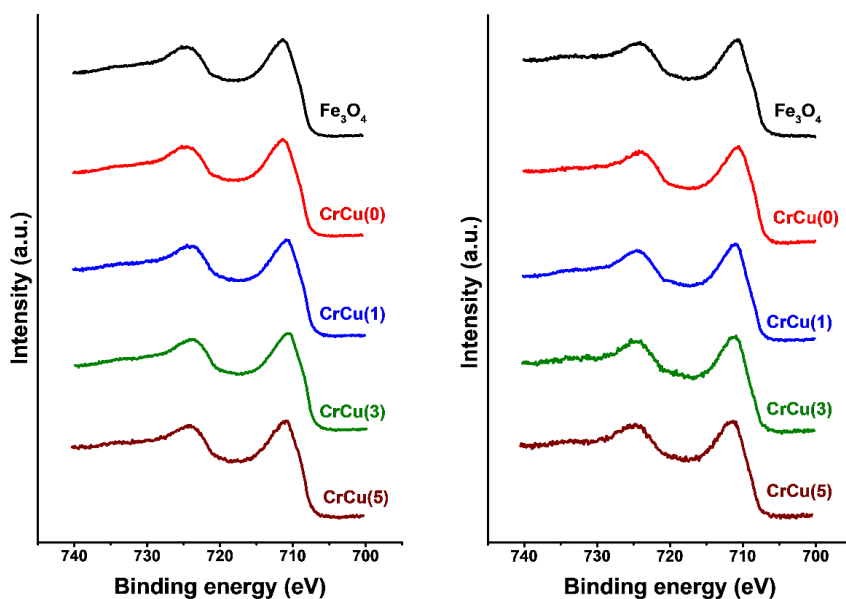


Figure 7. Fe 2p region XPS spectra recorded after treatment of the catalysts under HTS conditions for 96 hours at 2 bar (left) and 25 bar (right).

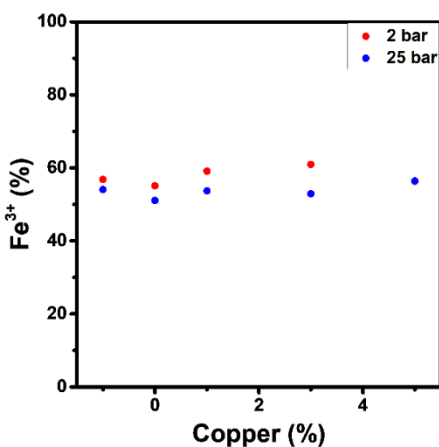


Figure 8. Fe³⁺ content obtained from fitting Fe 3p region. The reference Fe₃O₄ value is shown at -1% on the x-axis.

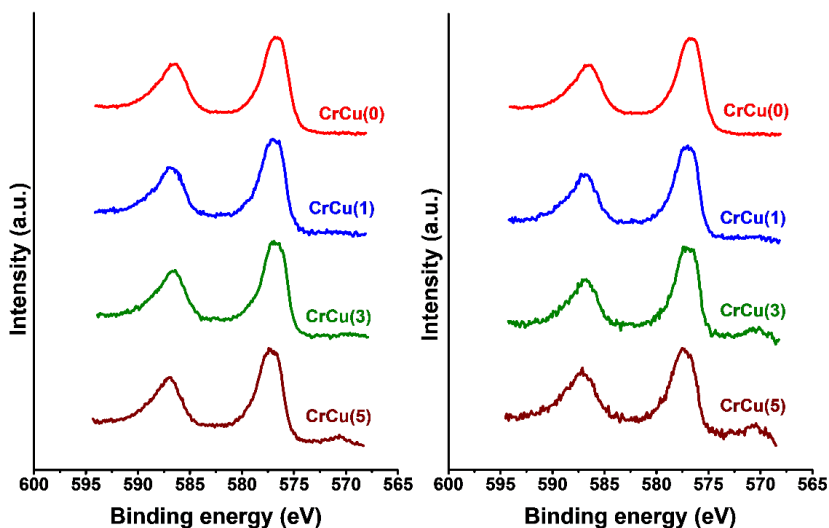


Figure 9. Cr 2p region XPS spectra recorded after treatment of the catalysts under HTS conditions for 96 hours at 2 bar (left) and 25 bar (right). Peaks at BE = ± 570 corresponds to Cu LMM ⁵⁰.

Analysis of the Cu 2p region (Fig. 10) confirmed the presence of copper on the surface of the used catalysts after treatment at 2 and 25 bar. The sharp peak at BE = 933 eV corresponds to either Cu⁰ or Cu⁺ oxide ⁵¹. Inspection of the Cu LMM region (Fig. 10) shows a peak at a kinetic energy (KE) ~ 916.7 eV, which is characteristic for Cu⁺ ^{51,52}. The formation of Cu⁺ instead of metallic copper

contradicts earlier findings by others^{6,21,22} and could be the result of the shutdown procedure after activity measurements or accidental exposure to air. After cooling to 250 °C, the CO, CO₂, and H₂ streams were switched to N₂ before water addition was stopped to prevent accidental over-reduction of the active Fe_{3-x(1-δ)Cr_xO₄ phase. Oxidation of Cu⁰ to Cu⁺ by water was observed before⁵³ and is therefore a likely cause.}

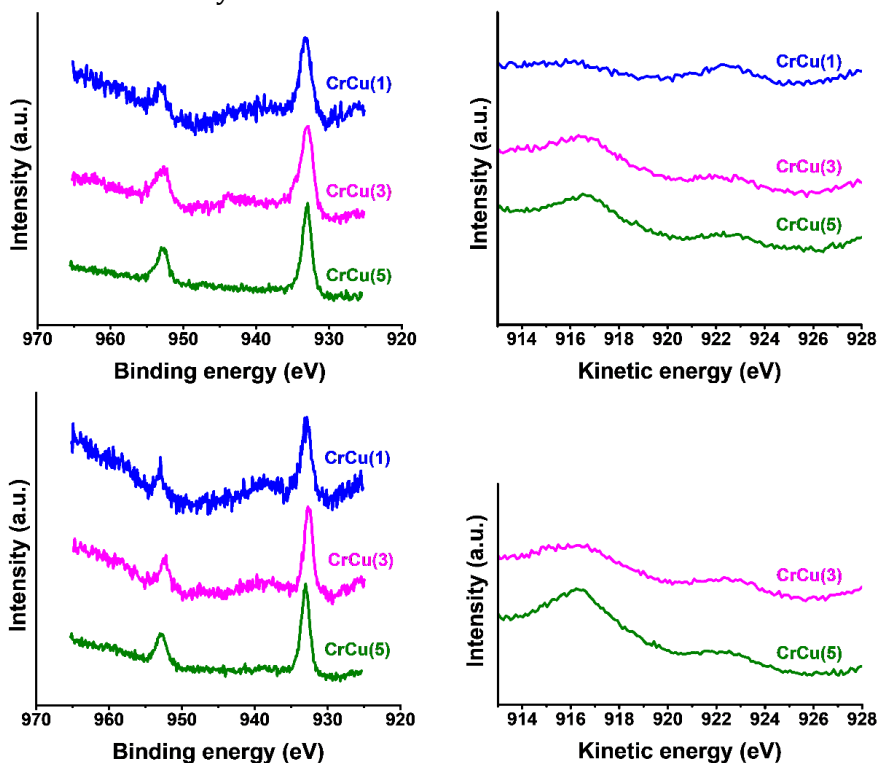


Figure 10. XPS spectra Cu 2p and Cu LMM region after treatment under HTS conditions for 96 hours at 2 bar (top) and 25 bar (bottom).

To further investigate the oxidation state of copper on the catalyst surface, NAP-XPS measurements were performed. Figure 11 shows the Cu 2p_{3/2} region and the Cu LMM region of CrCu(5) before and during exposure to a CO/H₂O mixture at a total pressure of 0.76 mbar. The Cu 2p_{3/2} region of the calcined catalyst shows a strong satellite peak at BE = ~941 eV, which points to the presence of Cu²⁺. Upon exposure to an atmosphere of steam (0.46 mbar) and raising the temperature from room temperature to 250 °C, the satellite peak at BE = ~941 eV disappeared and a sharp peak at BE = 932.3 eV became visible, which is typical for reduced Cu species (Cu⁰ and/or Cu⁺). Thus, heating in a

steam atmosphere led to the reduction of Cu^{2+} . The reduction of Cu^{2+} ($\text{CuO} \rightarrow \text{Cu}_2\text{O} + \frac{1}{2} \text{O}_2$) was observed before for CuO nanowires during heating between $155\text{ }^\circ\text{C}$ to $244\text{ }^\circ\text{C}$ under vacuum in *in-situ* TEM experiments⁵⁴. The Cu LMM feature at $\text{KE} = \sim 916.5\text{ eV}$ confirms the formation of Cu^+ . No change in Cu oxidation states was observed upon the replacement of the H_2O atmosphere by a $\text{CO}/\text{H}_2\text{O}$ mixture at $250\text{ }^\circ\text{C}$. When the temperature was raised to $450\text{ }^\circ\text{C}$, a peak at $\text{KE} = 918.8\text{ eV}$ was observed, while the peak at $\text{KE} = 916.6\text{ eV}$ disappeared. This confirms the presence of metallic copper on the catalyst in a $\text{H}_2\text{O}/\text{CO}$ mixture at $450\text{ }^\circ\text{C}$ ^{6,21,22}. The temperature was then lowered to $250\text{ }^\circ\text{C}$ and the catalyst was exposed to steam (0.46 mbar) at $250\text{ }^\circ\text{C}$ overnight to mimic water exposure during the shutdown procedure of experiments as discussed above. Exposure to H_2O did not lead to the oxidation of Cu^0 to Cu^+ . This is most likely the result of the low H_2O pressure during the NAP-XPS measurements (0.46 mbar) compared to 8.25 bar H_2O during the reactor activity evaluation at 25 bar . Exposure of the used catalyst to 0.3 mbar O_2 after cooling to RT in UHV also did not oxidise the catalyst, which further confirms that oxidation is hindered by low concentrations of the oxidising gases. The NAP-XPS experiments confirm that copper is present as Cu^0 after exposure to a $\text{CO}/\text{H}_2\text{O}$ mixture at $450\text{ }^\circ\text{C}$ ⁶. These experiments reveal that investigating HTS catalysts under NAP-XPS conditions is of limited value in understanding the dynamic phenomena occurring under industrially relevant HTS conditions and confirms the necessity to study carefully discharged catalysts used under relevant conditions. The presence of Cu^+ on the surface of the catalysts discharged after exposure to industrially relevant HTS conditions (Fig. 10) suggests that the oxidation of Cu^0 nanoparticles by H_2O on the active catalyst can easily occur under steam concentrations close to industrially relevant HTS conditions. This confirms that copper facilitates H_2O dissociation under industrially relevant conditions.²¹

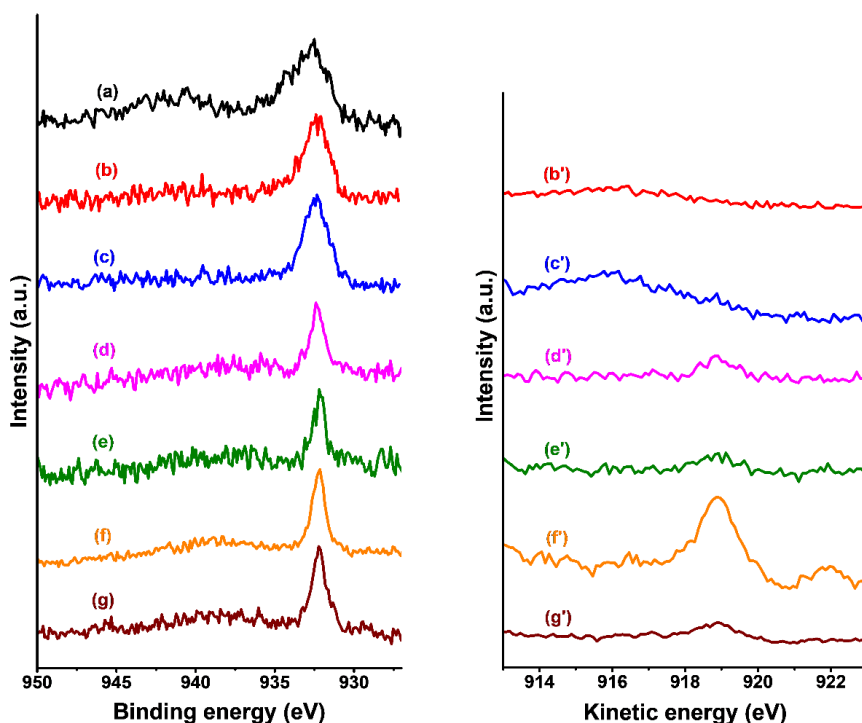


Figure 11. Cu $2p_{3/2}$ region (a-g) and Cu LMM region (b'-g') of CrCu(5) during NAP-XPS measurements in a $\text{H}_2\text{O} + \text{CO}$ (2:1) mixture ⁶. Conditions: (a) fresh; (b, b') H_2O , 250 °C; (c, c') $\text{H}_2\text{O} + \text{CO}$, 250 °C; (d, d') $\text{H}_2\text{O} + \text{CO}$, 450 °C; (e, e') $\text{H}_2\text{O} + \text{CO}$, 250 °C; (f, f') H_2O , 250 °C o.n.; (g, g') O_2 , RT.

3.4 CONCLUSIONS

Hematite is the dominant phase in freshly calcined iron-oxide and chromium-doped iron-oxide WGS catalysts. Calcined chromium-iron-oxide catalysts doped with copper consist of a mixture of hematite and ferrihydrite. Mössbauer spectra of copper-containing samples show that copper inhibits the formation of hematite during calcination. The amount of ferrihydrite increases with the copper content. Hematite and small particles of ferrihydrite convert completely to magnetite under industrially relevant HTS gas compositions at 2 and 25 bar. Mössbauer spectra show that chromium forms a solid solution with magnetite by occupying octahedral sites, resulting in a partially oxidised $\text{Fe}^{2+}/\text{Fe}^{3+}$ redox couple, which is known to be present in the bulk and at the surface of the catalyst. There was no effect of the pressure on the bulk structure. Copper doping had no significant effect on the hyperfine parameters in

Mössbauer spectra, meaning that it is not likely that copper is incorporated in the bulk structure. NAP-XPS experiments confirmed copper exists as metallic copper at the catalyst surface under WGS conditions. Catalysts exposed to HTS conditions at 25 bar had a more ferrous like surface than catalysts treated at 2 bar due to the more reducing nature of the gas mixture at elevated pressure. Chromium stabilises the high surface area of the catalyst at ambient and industrially relevant pressure, leading to a higher CO conversion. Copper promotes CO conversion at ambient and industrially relevant pressure by acting as a chemical promoter, which results in the formation of new active surface sites. Increased pressure has no effect on the chromium- and copper-induced activity increase nor on the bulk structure of the catalyst.

REFERENCES

- [1] M. Zhu; I.E. Wachs Iron-Based Catalysts for the High-Temperature Water-Gas Shift (HT-WGS) Reaction: A Review. *ACS catalysis*, **2016**, *6*, 722-732.
- [2] D.W. Lee; M.S. Lee; J.Y. Lee; S. Kim; H.J. Eom; D.J. Moon; K.Y. Lee The review of Cr-free Fe-based catalysts for high-temperature water-gas shift reactions. *Catalysis Today*, **2013**, *210*, 2-9.
- [3] IEA The Future of Hydrogen; <https://www.iea.org/reports/the-future-of-hydrogen>; 19.
- [4] D.S. Newsome The Water-Gas Shift Reaction. *Catalysis Reviews Science and Engineering*, **1980**, *21*, 275-318.
- [5] M.V. Twigg Catalyst handbook; 2 ed.; **1989**.
- [6] M. Zhu; T.C.R. Rocha; T. Lunkenbein; R. Schlogl; I.E. Wachs Promotion Mechanisms of Iron Oxide-Based High Temperature Water-Gas Shift Catalysts by Chromium and Copper. *ACS catalysis*, **2016**, *6*, 4455-4464.
- [7] C. Ratnasamy; J.P. Wagner Water Gas Shift Catalysis. *Catalysis Reviews*, **2009**, *51*, 325-440.
- [8] C.J. Keturakis; M. Zhu; E.K. Gibson; M. Daturi; F. Tao; A.I. Frenkel; I.E. Wachs Dynamics of CrO₃-Fe₂O₃ Catalysts during the High-Temperature Water-Gas Shift Reaction: Molecular Structures and Reactivity. *ACS catalysis*, **2016**, *6*, 4786-4798.
- [9] D. Damma; P.G. Smirniotis Recent advances in iron-based high-temperature water-gas shift catalysis for hydrogen production. *Current Opinion in Chemical Engineering*, **2018**, *21*, 103-110.
- [10] A. Khan; P.G. Smirniotis Relationship between temperature-programmed reduction profile and activity of modified ferrite-based catalysts for WGS reaction. *Journal of Molecular Catalysis A: Chemical*, **2008**, *280*, 43-51.
- [11] C. Rhodes; G.J. Hutchings; A.M. Ward Water-gas shift reaction: finding the mechanistic boundary. *Catalysis Today*, **1995**, *23*, 43-58.
- [12] J.E. Kubsh; J.A. Dumesic In situ gravimetric studies of the regenerative mechanism for water-gas shift over magnetite: Equilibrium and kinetic

- measurements in CO₂/CO and H₂O/H₂ gas mixtures. *American Institute of Chemical Engineers*, **1982**, *28* (5), 793-800.
- [13] G.K. Boreskov; T.M. Yurieva; A.S. Sergeeva Mechanism of the Conversion of Carbon Monoxide on Iron-Chromium Catalyst. *Kinet. Catal.*, **1970**, *11*, 374-381.
- [14] M. Robbins; G.K. Wertheim; R.C. Sherwood; D.N.E. Buchanan MAGNETIC PROPERTIES AND SITE DISTRIBUTIONS IN THE SYSTEM FeCr₂O₄-Fe₃O₄(Fe₂+Cr₂-xFe₃+xO₄). *J. Phys. Chem. Solids*, **1971**, *32*, 717-729.
- [15] H.J. Levinstein; M. Robbins; C. Capio A CRYSTALLOGRAPHIC STUDY OF THE SYSTEM FeCr₂O₄-Fe₃O₄(Fe₂+Fe₃+xCr₂-xO₄). *Mat. Res. Bull.*, **1972**, *7*, 27-34.
- [16] H. Topsoe; M. Boudart Mossbauer Spectroscopy of CO Shift Catalysts promoted with Lead. *Journal of Catalysis*, **1973**, *31*, 346-359.
- [17] S. Natesakhawat; X. Wang; L. Zhang; U.S. Ozkan Development of chromium-free iron-based catalysts for high-temperature water-gas shift reaction. *Journal of Molecular Catalysis A: Chemical*, **2006**, *260*, 82-94.
- [18] M. Zhu; I.E. Wachs A perspective on chromium-Free iron oxide-based catalysts for high temperature water-gas shift reaction. *Catalysis Today*, **2018**, *311*, 2-7.
- [19] M. Estrella; L. Barrio; G. Zhou; X. Wang; Q. Wang; W. Wen; J.C. Hanson; A.I. Frenkel; J.A. Rodriguez In Situ Characterization of CuFe₂O₄ and Cu/Fe₃O₄ Water-Gas Shift Catalysts. *Journal of Physical Chemistry C* **2009**, *113*, 14411-14417.
- [20] A. Puig-Molina; F. Morales Cano; T.V.W. Janssens The Cu Promoter in an Iron-Chromium-Oxide Based Water-Gas Shift Catalyst under Industrial Conditions Studied by in-Situ XAFS. *Journal of Physical Chemistry C*, **2010**, *114*, 15410-15416.
- [21] M. Zhu; P. Tian; R. Kurtz; T. Lunkenbein; J. Xu; R. Schlogl; I.E. Wachs; Y.F. Han Strong Metal-Support Interactions between Copper and Iron Oxide during the High-Temperature Water-Gas Shift Reaction. *Angewandte Chemie*, **2019**, *131*, 9181-9185.

- [22] M. Zhu; P. Tian; J. Chen; M.E. Ford; J. Xu; I.E. Wachs; Y.F. Han Activation and deactivation of the commercial-type CuO–Cr₂O₃–Fe₂O₃ high temperature shift catalyst. *American Institute of Chemical Engineers* **2019**.
- [23] C. Pellerin; S. M. Booker Reflections on hexavalent chromium: health hazards of an industrial heavyweight. *Environmental health perspectives*, **2000**, *108*, A402-A407.
- [24] Fereshteh Meshkani; Mehran Rezaei Preparation of Mesoporous Chromium Promoted Magnetite Based Catalysts for High Temperature Water Gas Shift Reaction. *Industrial & Engineering Chemistry Research*, **2015**, *54*, 1236-1242.
- [25] T. Popa; G. Xu; T.F. Barton; M.D. Argyle High temperature water gas shift catalysts with alumina. *Applied Catalysis A: General*, **2010**, *379*, 15-23.
- [26] E.B. Quadro; M. de Lourdes Ribeiro Dias; A.M.M. Amorim; M. do Carmo Rangel Chromium and Copper-Doped Magnetite Catalysts for the High Temperature Shift Reaction. *Journal of the Brazilian Chemical Society*, **1999**, *10*, 51-59.
- [27] M.A. Edwards; D.M. Whittle; C. Rhodes; A.M. Ward; D. Rohan; M.D. Shannon; G.J. Hutchings; C.J. Kiely Microstructural studies of the copper promoted iron oxide/chromia water-gas shift catalyst. *Physical Chemistry Chemical Physics*, **2002**, *4*, 3902-3908.
- [28] G.K. Reddy; P. Boolchand; P.G. Smirniotis Unexpected Behavior of Copper in Modified Ferrites during High Temperature WGS Reaction- Aspects of Fe³⁺ → Fe²⁺ Redox Chemistry from Mossbauer and XPS Studies. *Journal of Physical Chemistry C*, **2012**, *116*, 11019-11031.
- [29] V.P. Santos; T.A. Wezendonk; J.J. Delgado Jaen; A.I. Dugulan; M.A. Nasalevich; H.U. Islam; A. Chojecki; S. Sartipi; X. Sun; A.A. Hakeem; A.C.J. Koeken; M. Ruitenbeek; T. Davidian; G.R. Meima; G. Sankar; F. Kapteijn; M. Makkee; J. Gascon Metal organic framework-mediated synthesis of highly active and stable Fischer-Tropsch catalysts. *NATURE COMMUNICATIONS*, **2015**, *6*, 6451.
- [30] S. Morup; J.A. Dumesic; H. Topsoe; R.L. Cohen Applications of Mössbauer Spectroscopy, vol. II; **1980**; Vol. 2.

- [31] G.K. Reddy; S.J. Kim; J. Dong; P.G. Smirniotis; J.B. Jasinski Long-term WGS stability of Fe/Ce and Fe/Ce/Cr catalysts at high and low steam to CO ratios-XPS and Mössbauer spectroscopic study. *Applied Catalysis A: General*, **2012**, 415-416, 101-110.
- [32] M.I. Ariëns; V. Chlan; P. Novak; L.G.A. van de Water; A.I. Dugulan; E. Brück; E.J.M. Hensen The role of chromium in iron-based high-temperature water-gas shift catalysts under industrial conditions. *Applied Catalysis B: Environmental*, **2021**, 297, 120465
- [33] Z. Klencsár Mössbauer spectrum analysis by Evolution Algorithm. Nuclear Instruments and Methods in Physics Research Section B: Beam Interactions with Materials and Atoms **1997**, 129, 527-533.
- [34] T. Yamashita; P. Hayes Analysis of XPS spectra of Fe²⁺ and Fe³⁺ ions in oxide materials. *Applied Surface Science*, **2008**, 254, 2441-2449.
- [35] A. Parastaev; V. Muravev; E.H. Osta; A.J.F. van Hoof; T.F. Kimpel; N. Kosinov; E.J.M. Hensen Boosting CO₂ hydrogenation via size-dependent metal-support interactions in cobalt/ceria-based catalysts. *Nature catalysis*, **2020**.
- [36] G.K. Reddy; P.G. Smirniotis Effect of Copper as a Dopant on the Water Gas Shift Activity of Fe/Ce and Fe/Cr Modified Ferrites. *Catalysis Letters*, **2011**, 141, 27-32.
- [37] M. Zhu; Ö. Yalçin; I.E. Wachs Revealing structure-activity relationships in chromium free high temperature shift catalysts promoted by earth abundant elements. *Applied Catalysis B: Environmental*, **2018**, 232, 205-212.
- [38] G. Doppler; A.X. Trautwein; H.M. Ziethen; E. Ambach; R. Lehnert; M.J. Sprague; U. Gonser Physical and Catalytic Properties of High-Temperature Water-Gas Shift Catalysts Based upon Iron-Chromium oxides. *Applied Catalysis*, **1988**, 40, 119-130.
- [39] O. Ozdemir; D.J. Dunlop; T.S. Berquo Morin transition in hematite: Size dependence and thermal hysteresis. *Geochemistry Geophysics Geosystems*, **2008**, 9, 1-12.
- [40] A. Khan; P. Chen; P. Boolchand; P.G. Smirniotis Modified nanocrystalline ferrites for high-temperature WGS membrane reactor applications. *Journal of Catalysis*, **2008**, 253, 91-104.

- [41] R.M. Cornel; U. Schwertmann The Iron Oxides: Structures, Properties, Reactions, Occurrences and Uses; **2003**.pp. 155-156.
- [42] T. Lais; L. Lukashuk; L.G.A. van de Water; T.I. Hyde; M. Araminid; G. Sankar Elucidation of copper environment in a Cu–Cr–Fe oxide catalyst through in situ high-resolution XANES investigation. *Physical Chemistry Chemical Physics*, **2021**, *23*, 5888-5896.
- [43] G.M. da Costa; C. Blanco-Andujar; E. de Grave; Q.A. Pankhurst Magnetic Nanoparticles for in Vivo Use: A Critical Assessment of Their Composition. *The Journal of Physical Chemistry B*, **2014**, *114*, 11738-11746.
- [44] C.E. Johnson; J.A. Johnson; H.Y. Hah; M. Cole; S. Gray; V. Kolesnichenko; P. Kucheryavy; G. Goloverda Mossbauer studies of stoichiometry of Fe₃O₄: characterization of nanoparticles for biomedical applications. *Hyperfine Interact*, **2016**, *237*, 27-1-27-10.
- [45] I.S. Lyubutin; C.R. Lin; Y.V. Korzhetskiy; T.V. Dmitrieva; R.K. Chiang Mössbauer spectroscopy and magnetic properties of hematite/magnetite nanocomposites. *JOURNAL OF APPLIED PHYSICS*, **2009**, *106*, 034311-034311-6.
- [46] Z. Klencsár; A. Ábrahám; L. Szabó; E.G. Szabó; S. Stichleitner; E. Kuzmann; Z. Homonnay; G. Tolnai The effect of preparation conditions on magnetite nanoparticles obtained via chemical co-precipitation. *Materials Chemistry and Physics*, **2019**, *223*, 122-132.
- [47] M. do Carmo Rangel; R.M. Sasaki; F. Galembek Effect of chromium on magnetite formation. *Catalysis Letters*, **1995**, *33*, 237-254.
- [48] M.F.F. Lelis; A.O. Porto; C.M. Goncalves; J.D. Fabris Cation occupancy sites in synthetic Co-doped magnetites as determined with X-ray absorption (XAS) and Mossbauer spectroscopies. *Journal of Magnetism and Magnetic Materials*, **2004**, *278*, 263-269.
- [49] M.C. Biesinger; B.P. Payne; A.P. Grosvenor; L.W.M. Lau; A.R. Gerson; R. S.C. Smart Resolving surface chemical states in XPS analysis of first row transition metals, oxides and hydroxides: Cr, Mn, Fe, Co and Ni. *Applied Surface Science journal*, **2011**, *257*, 2717-2730.
- [50] L. Zhang; L. Han; G. Zhao; R. Chai; Q. Zhang; Y. Liu; Y. Lu Structured Pd–Au/Cu-fiber catalyst for gas-phase hydrogenolysis of dimethyl oxalate

- to ethylene glycol. *ChemComm COMMUNICATION*, **2015**, *51*, 10547-10550.
- [51] Y. Gao; E.J.M. Hensen Highly active and stable spinel-oxide supported gold catalyst for gas-phaseselective aerobic oxidation of cyclohexanol to cyclohexanone. *Catalysis Communications*, **2018**, *117*, 53-56.
- [52] I. Platzman; R. Brener; H. Haick; R. Tannenbaum Oxidation of Polycrystalline Copper Thin Films at Ambient Conditions. *Journal of Physical Chemistry C*, **2008**, *112*, 1101-1108.
- [53] T. Shishido; M. Yamamoto; I. Atake; D. Li; Y. Tian; H. Morioka; M. Honda; T. Sano; K. Takehira Cu/Zn-based catalysts improved by adding magnesium for water-gas shift reaction. *Journal of Molecular Catalysis A: Chemical*, **2006**, *253*, 270-278.
- [54] L. Yuan; Q. Yin; Y. Wang CuO reduction induced formation of CuO/Cu₂O hybrid oxides. *Chemical Physics Letters*, **2013**, *590*, 92-96.

4

ALTERNATIVE DOPANTS

ABSTRACT

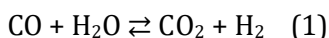
A set of doped iron oxides (chromium, aluminium, gallium, indium, manganese, zinc, niobium) were prepared by a one-step co-precipitation/calcination approach, evaluated for their WGS activity under industrially relevant conditions, and characterised in detail. The WGS activity after ageing the doped catalyst for 4 days at 25 bar follows the order chromium \approx aluminium > gallium > indium > manganese > zinc > niobium for copper co-doped catalysts. The activated catalysts predominantly consist of magnetite, irrespective of the dopant. Mössbauer spectra of aged catalysts showed that aluminium and zinc occupy both tetrahedral and octahedral sites of magnetite, while chromium, gallium, indium, manganese, and niobium preferentially substitute octahedral iron. The incorporation of trivalent metal ions of similar size to octahedral Fe^{3+} (i.e., chromium, aluminium, gallium) increases the CO conversion relative to a non-doped catalyst, irrespective of incorporation in tetrahedral or octahedral sites. The substitution of Fe^{2+} with Mn^{2+} results in an increased $\text{Fe}^{3+}/\text{Fe}^{2+}$ ratio. Incorporation of Zn^{2+} in tetrahedral sites (replacing Fe^{3+} ions) leads to a complex structure where the charge balance is compensated from the

octahedral sites. Separate dopant metal oxide phases were observed in indium- and niobium-doped catalysts. XPS shows that copper is present as a separate phase in activated copper co-doped catalysts. Aluminium is identified as the most promising promoter for substituting chromium in commercial high-temperature WGS catalysts on the basis of their similar high CO conversion, although incorporation of these dopants into the magnetite structure differed substantially.

This chapter was published as: M.I. Ariëns, L.G.A. van de Water, A.I. Dugulan, E. Brück, E.J.M. Hensen, *ACS catalysis*, 2022, 12, 22, 13838-13852.

4.1 INTRODUCTION

Approximately 80% of industrial hydrogen gas is produced from natural gas by steam reforming, followed by the water-gas shift (WGS) reaction (1) ¹. The industrial WGS process involves two temperature stages in order to optimise CO conversion. High-temperature (water-gas) shift (HTS) removes the bulk of CO from the gas stream at temperatures between 350 and 450 °C, while low-temperature (water-gas) shift (LTS) removes most of the remaining CO at 190-250 °C ¹⁻⁴.



The active HTS catalyst, the mixed-valence iron oxide compound magnetite (Fe_3O_4), is obtained upon partial reduction of the Fe^{3+} -oxides/oxyhydroxide precursor species under WGS conditions ^{5,6}. Chromium and copper are used as promoters in commercial HTS catalysts to enhance stability and activity. Chromium exists as Cr^{6+} and Cr^{3+} in the calcined catalyst precursor and ends up as Cr^{3+} in the active magnetite phase ⁷. Chromium doping limits Fe^{2+} formation during activation, resulting in a partially oxidised magnetite structure ^{5,8}, thereby improving the thermal stability and preventing over-reduction of the active phase. Copper is known to facilitate the partial reduction of Fe^{3+} oxides/oxyhydroxide during magnetite formation, it has also been shown that the presence of Cu^0 nanoparticles on the surface of the active magnetite catalyst, partially covered by an iron oxide layer, results in additional active sites ^{9,10}.

Tightening regulations on hazardous chemicals is calling for replacement of chromium by an effective alternative with reduced environmental impact ¹¹. This has motivated researchers to identify dopants that can replace chromium in HTS catalysts ^{12,13}. Comprehensive reviews on alternatives for chromium can be found in literature ^{2,14}. A direct comparison of the potential of these alternative dopants is difficult, because the catalyst preparation methods and specific preparation details, such as the calcination temperature, doping levels, as well as test conditions (temperature, pressure, feed gas composition, and test duration) vary among such investigations. The replacement of chromium by aluminium has received most attention ¹⁴. Zhu et al. showed that aluminium- and aluminium-copper-doped catalysts show comparable thermal stability as chromium-doped catalysts during the WGS reaction at different temperatures

at 1 bar for 90 minutes¹². Meshkani and Rezaei¹⁵ observed that an aluminium-doped HTS catalyst with an aluminium/iron ratio of 1:10 at/at and an atomic copper/iron ratio of 1:10 exhibited a higher conversion than a commercial catalyst after two hours in a WGS test at 1 bar. It should be mentioned that practical catalysts have typical lifetimes of several years in commercial operation⁴. Natesakhawat et al.¹⁶ showed that aluminium doping prevents sintering of magnetite during the WGS reaction. Moreover, they found that the effect of copper promotion depended on the preparation method, as reported before for chromium-doped catalysts¹⁷. Cerium-doped iron oxide catalysts have also been thoroughly investigated in recent years^{13,15,18,19}. Smirniotis' group²⁰ showed that chromium- and cerium co-doped catalysts were the most active in the WGS reaction at atmospheric pressure among a series of chromium-, cerium-, manganese-, cobalt-, nickel-, copper-, zinc-doped catalysts. A sample doped with cerium and chromium in an equimolar ratio provided the highest WGS activity²¹. However, co-doping of the cerium-doped catalyst with copper led to faster deactivation due to over-reduction of the active phase to FeO¹⁹. Meshkani and Rezaei, however, found that a cerium-doped catalyst had the lowest CO conversion among a series of cerium-, manganese-, aluminium- and chromium-doped catalysts¹⁵. It is worthwhile to mention that also catalysts co-doped with nickel have been explored, although the presence of other promoters like sodium²² or niobium²³ is required to suppress methanation.

The local structure of iron oxide HTS catalysts modified with alternative dopants has not been investigated systematically^{12,15}. Another limitation of earlier studies is that most of the activity tests were carried out at atmospheric pressure for a relatively short period under conditions different to those used in commercial HTS configurations⁴. Our previous study⁵ showed that Cr³⁺ is incorporated in the octahedral sites of magnetite in the activated catalyst and that its presence in the fresh catalyst limits the formation of Fe²⁺ during the activation procedure. The incorporation of copper in the magnetite structure was found to be unlikely⁶ which is confirmed by the presence of a separate Cu⁰ phase in the form of nanoparticles^{9,10}. In this study, we investigate the potential of alternative dopants to replace chromium (aluminium, gallium, indium, zinc, manganese, and niobium). All catalysts were prepared with and without co-doping with copper. Besides screening these novel catalysts for their WGS activity under industrially relevant conditions, a thorough investigation of the catalyst structure was made after ageing for 4 days at 25

bar. The group 13 elements aluminium, gallium, and indium were chosen to evaluate the effect of the octahedral ionic radius of trivalent dopants on the local structure. Zinc, manganese (2+), and niobium were selected to investigate the effect of elements with different oxidation states. In addition to routine characterisation techniques such as XRD and XPS, Mössbauer spectroscopy was employed to investigate the local structure of the activated promoted magnetite catalysts. Mössbauer spectroscopy is a highly sensitive technique for bulk-iron species, capable of distinguishing separate contributions of iron in tetrahedral and octahedral positions in the magnetite structure, thus allowing studying of the local structure⁵. The catalytic performance of these samples was evaluated under industrially relevant conditions for 4 days and at a total pressure of 25 bar.

4.2 EXPERIMENTAL

4.2.1 CATALYST PREPARATION

Catalysts were prepared via a single-step co-precipitation/calcination procedure adapted from²⁴. Appropriate amounts of the nitrate salts of Fe³⁺, Cr³⁺, Al³⁺, Ga³⁺, In³⁺, Mn²⁺, Zn²⁺, and Cu²⁺ and a Nb⁵⁺ salt (ammonium niobate oxalate hydrate) were dissolved in deionised water and heated at 60 °C. A NaOH solution was added at this temperature under vigorous stirring until the pH reached 10, followed by ageing the resulting slurry at 60 °C under vigorous stirring for 1 h. The precipitates were filtered, washed and dried at 150 °C for 3 hours, followed by calcination at 400 °C for 4 hours in static air. The target dopant/iron atomic ratio of 8.4 % was chosen to correspond with the Cr doping level in 8 wt.% Cr₂O₃/α-Fe₂O₃. A CuO doping level of 3 wt.% CuO was used, typical for a commercial catalyst composition. Freshly calcined catalysts will be referred to as M-HM or MCu-HM, where M is the metal dopant and HM the hematite phase. Some characterisation data of the HM, Cr-HM, and CrCu-HM reference catalysts were published elsewhere⁵⁻⁶.

4.2.2 CATALYST CHARACTERISATION

XRD patterns were recorded on a PANalytical X'pert pro diffractometer using Cu-K_α radiation. HighScore Plus software was used for spectral fitting. Discharged catalysts were stored in an argon atmosphere before and during measurements. Transmission ⁵⁷Fe Mössbauer spectra were recorded using a ⁵⁷Co (Rh) source with constant-acceleration or sinusoidal velocity

spectrometers. Calibration was performed relative to α -Fe at room temperature. The source and the absorbing samples were kept at the same temperature during measurements. Spectral fitting was performed using Mosswin 4.0 software. Hyperfine magnetic field values fitted with a distribution fit are reported as averages. Fixed values are indicated when applied. Nitrogen physisorption was carried out on a Micromeritics 2420 ASAP instrument. Samples were degassed with nitrogen at 140 °C for at least 1 h prior to analysis. XPS was performed on a Thermo Scientific K-Alpha spectrometer using an aluminium anode (Al K α = 1486.6 eV). The binding energy was calibrated relative to adventitious carbon at a binding energy (BE) of 285 eV and the CasaXPS software (version 2.3.19PR1.0) was used for spectral fitting. Samples were placed on a carbon tape and transferred to the spectrometer under vacuum.

4.2.3 CATALYTIC ACTIVITY MEASUREMENTS

Catalytic performance testing was conducted in a parallel micro-reactor setup. The reactor tubes were charged with calcined catalyst precursors diluted with α -Al₂O₃. Prior to activity measurements, the reactor tubes were purged with nitrogen. Catalysts were activated in the presence of process gas (37% H₂, 9% CO, 4% CO₂, 17% N₂, 33% H₂O) and heated to 450 °C, at which temperature the catalysts were thermally aged for 24 h. The temperature was lowered to 360 °C for activity measurements (24 h). The catalysts were then aged once more for 24 h at 450 °C, followed by a final activity measurement at 360 °C (24 h). Continuous gas-phase analysis by an infrared gas analyser allowed determining the CO conversion. At the end of the activity tests, the reactors were cooled to 250 °C, followed by a switch from the reaction gas mixture to N₂. Steam addition was switched off after CO was not observed anymore in the effluent stream. Samples were kept under N₂ after the reaction, before being stored in a glovebox under Ar atmosphere. Used catalysts are named in a similar fashion as the calcined catalysts, with HM (hematite) being replaced by MG for magnetite. Some characterisation data of the MG, Cr-MG, and CrCu-MG reference catalysts were published elsewhere^{5,6}.

4.3 RESULTS AND DISCUSSION

4.3.1 CALCINED CATALYSTS

Table 1. Physico-chemical properties of calcined M-doped and MCu-doped catalysts.

Sample	dXRD ^a (nm)	SSA ^b (m ² g ⁻¹)	V _{pore} (cm ³ g ⁻¹)	d _{pore} (nm)	MO _x ^c (wt. %)	M (mol %)	CuO (wt. %)	Na ₂ O ^c (wt. %)
HM ^d	44	45	0.22	19.9	0	0	0	0.6
Cr-HM ^d	25	110	0.25	9.2	7.5	7.7	0	1.5
CrCu-HM ^d	*	132	0.20	6	8.4	8.7	3.1	0.7
Al-HM	*	140	0.26	7.4	5.3	8.0	0.0	1.0
AlCu-HM	*	168	0.26	6.1	5.2	7.8	3.0	0.6
Ga-HM	41	51	0.23	18	5.8	5.0	0.0	0.5
GaCu-HM	*	133	0.21	6.4	5.6	4.8	3.0	0.4
In-HM	*	124	0.24	7.8	12.7	7.6	0.0	0.8
InCu-HM	*	153	0.26	6.7	12.9	7.8	2.8	0.4
Mn-HM	17	105	0.22	8.4	8.4	8.4	0.0	0.4
MnCu-HM	*	153	0.27	7.1	8.3	8.3	2.9	0.2
Zn-HM	23	93	0.22	9.6	8.3	8.1	0.0	0.5
ZnCu-HM	*	137	0.21	6.1	8.6	8.4	2.9	0.1
Nb-HM	*	140	0.25	7.3	3.3	5.4	0.0	1.6
NbCu-HM	*	155	0.26	6.7	3.4	5.6	3.1	1.2

^a Calculated with the Scherrer equation from the α -Fe₂O₃ (110) reflection.

^b Specific surface area (SSA), pore volume (V_{pore}), and pore diameter (d_{pore}) determined by the Brunauer-Emmett-Teller (BET) method.

^c Obtained by XRF analysis.

^d From ⁶

A set of metal-doped iron oxide HTS catalysts was prepared by co-precipitation of metal salts followed by calcination according to a method adapted from Meshkani and Rezaei ²⁴. Non-doped hematite (HM) and chromium-doped hematite (Cr-HM) samples are used as reference samples for the discussion of the characterisation and catalytic performance results. The physico-chemical properties of the calcined catalyst precursors are collected in Table 1, the XRD patterns in Figure 1. The dopant content of the samples was close to the intended loading of 8.4 mol%. This ratio was chosen on the basis of the optimum chromium loading (8 wt% Cr₂O₃ in α -Fe₂O₃, 8.4 mol% Cr) typical for a commercial HTS catalyst ²⁴. The dopant content of the gallium- and niobium-doped catalysts were slightly lower than intended.

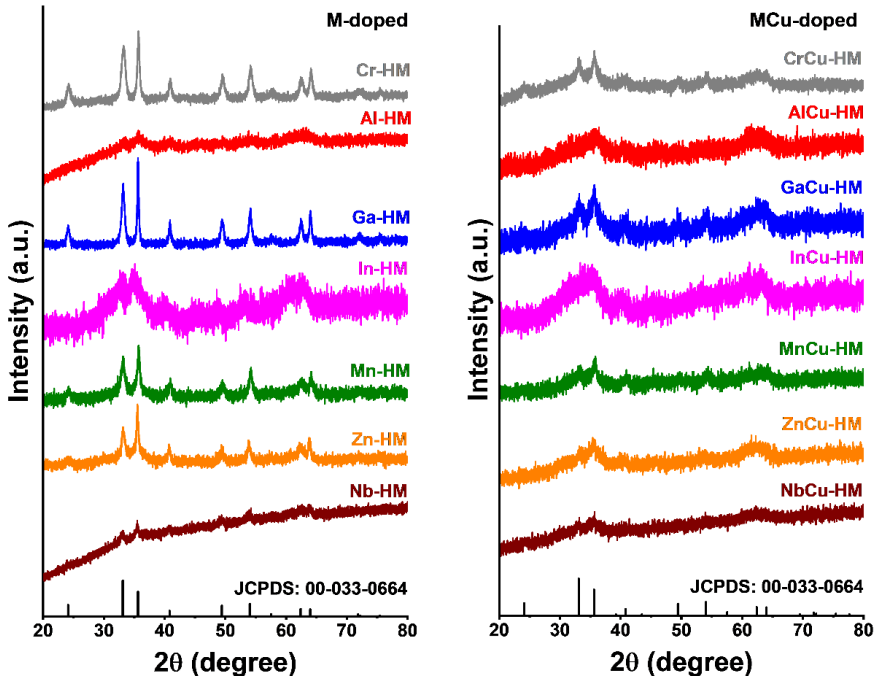


Figure 1. XRD patterns of calcined catalysts. M-doped (left), MCu-doped (right). JCPDS: 00-033-0664 was used as a hematite reference pattern.

The XRD patterns of all calcined samples (Fig. 1) show reflections that can be attributed to hematite. Chromium is known to prevent thermal agglomeration during calcination of the oxide/hydroxide precursor. The XRD patterns of MCu-HM catalysts are significantly broadened compared to those of M-HM and HM catalysts, which suggests the presence of smaller hematite particles in the Cu-doped samples. However, the reflections observed can also be attributed to the presence of ferrihydrite. Smaller HM particles were observed previously in calcined chromium-copper co-doped HTS catalysts compared to a chromium-doped catalyst⁶. No diffraction lines of dopant-oxide phases were observed in the XRD patterns. This may be taken as an indication that most of the dopants end up in the hematite structure, although we cannot exclude the presence of segregated dopant oxide particles with small crystallite size (<3-4 nm) or amorphous in nature¹². Similarly, the presence of non-crystalline or weakly crystalline Fe oxide phases cannot be excluded based on the XRD results.

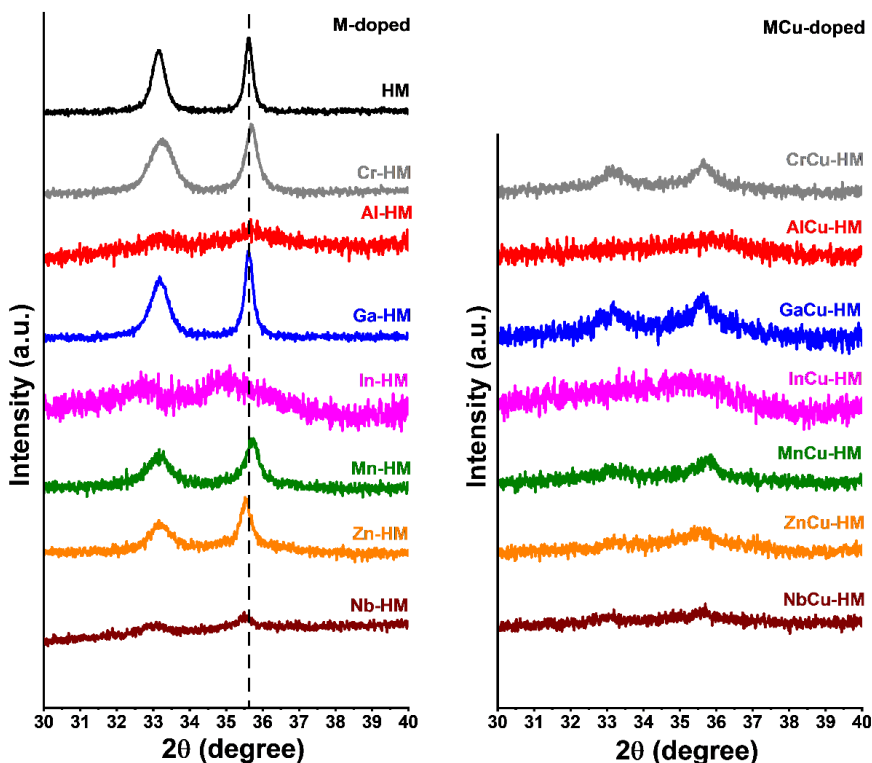


Figure 2. XRD patterns of freshly calcined catalysts in the 2θ range of the (110) reflection of hematite of M-HM catalysts (left) and MCu-HM catalysts (right).

A magnification of the 2θ range corresponding to the (110) reflection of hematite is provided in Figure 2. In the Cr-HM, Al-HM and Mn-HM samples, the (110) reflection is shifted to higher 2θ values compared to the HM reference, indicating that the unit cell is smaller upon doping. This is expected¹² for the incorporation of dopants (62 pm, Cr³⁺ (oct.); 54 pm, Al³⁺ (oct.)) with smaller ionic radii than iron (65 pm, Fe³⁺ (oct.)). The shift to a higher 2θ value in the Mn-doped catalyst can be explained by oxidation of the initially present Mn²⁺ (oct.) (83 pm) to Mn⁴⁺ (oct.) (53 pm) upon calcination in air. The (110) reflection of the In-HM, Zn-HM and Nb-HM catalysts shifted to lower 2θ values, which implies increased unit cell dimensions upon doping. This is in line with the larger ionic radii of indium and zinc (80 pm, In³⁺; 74 pm, Zn²⁺) than Fe³⁺. The shifted 2θ value of the Nb-HM catalyst cannot be explained by the octahedral ionic radius of Nb⁵⁺ (64 pm), which is similar to that of Fe³⁺. No shift was observed for the Ga-HM sample, which may be due to its very similar ionic radius (62 pm, Ga³⁺ (oct.)) to Fe³⁺, or a low substitution level.

Table 2. Mössbauer parameters upon deconvolution of the room-temperature spectra of the calcined HTS catalysts.

Sample	IS (mm s ⁻¹)	QS (mm s ⁻¹)	H (T)	Γ (mm s ⁻¹)	Phase	(%) ^d
HM ^c	0.38	-0.23	50.5†	0.23	α-Fe ₂ O ₃	100
Cr-HM ^c	0.38	-0.21	48.5†	0.25	α-Fe ₂ O ₃	100
CrCu-HM ^c	0.34	0.71	-	0.59	Fe ³⁺ SPM	100
Al-HM	0.34	0.70	-	0.53	Fe ³⁺ SPM	100
AlCu-HM	0.34	0.70	-	0.51	Fe ³⁺ SPM	100
Ga-HM	0.37	-0.21	49.9†	0.26	α-Fe ₂ O ₃	98
	0.34	0.87	-	0.50*	Fe ³⁺ SPM	2
GaCu-HM	0.34	0.71	-	0.56	Fe ³⁺ SPM	100
In-HM	0.34	0.70	-	0.55	Fe ³⁺ SPM	100
InCu-HM	0.34	0.71	-	0.50*	Fe ³⁺ SPM	100
Mn-HM	0.37	-0.20	48.8†	0.26	α-Fe ₂ O ₃	50
	0.34	0.73	-	0.50*	Fe ³⁺ SPM	50
MnCu-HM	0.37*	-0.21*	48.6	0.50*	α-Fe ₂ O ₃	16
	0.34	0.71	-	0.50*	Fe ³⁺ SPM	84
Zn-HM	0.38	-0.20	50.3	0.29	α-Fe ₂ O ₃	42
	0.35	0.66	-	0.52	Fe ³⁺ SPM	58
ZnCu-HM	0.37*	-0.21*	49.7	0.50	α-Fe ₂ O ₃	8
	0.34	0.69	-	0.50*	Fe ³⁺ SPM	92
Nb-HM	0.37	-0.21*	50.1	0.50*	α-Fe ₂ O ₃	17
	0.34	0.73	-	0.50*	Fe ³⁺ SPM	83
NbCu-HM	0.34	0.74	-	0.50*	Fe ³⁺ SPM	100

^a Fixed values are marked with a *, average values with †.

^b Experimental uncertainties: IS ± 0.01 mm s⁻¹, QS ± 0.01 mm s⁻¹, line width: Γ ± 0.01 mm s⁻¹, hyperfine magnetic field: H ± 0.1 T, spectral contribution: ± 3%.

^c From ⁶.

^d Spectral contribution.

With the exception of the Ga-HM, Mn-HM, and Zn-HM catalysts, all samples containing alternative dopants displayed a higher surface area with respect to the HM and Cr-HM references. This suggests an increased resistance against agglomeration of the precursor oxides during the calcination step.

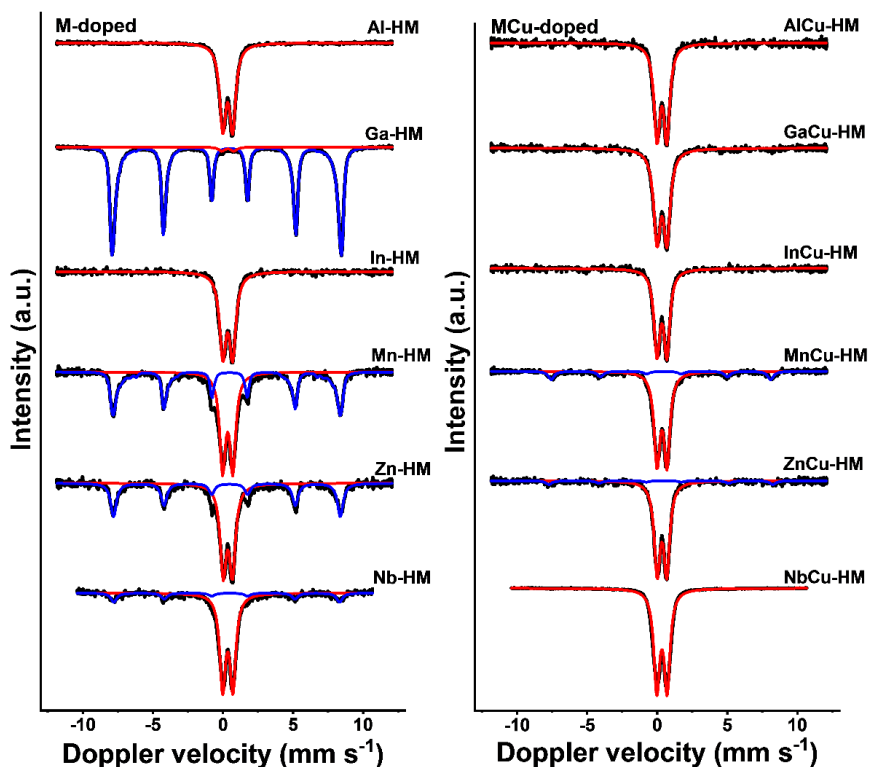


Figure 3. Room-temperature Mössbauer spectra of M-doped (left) and MCu-doped (right) HTS catalysts.

In order to further investigate the highly dispersed or amorphous iron oxide phases present in these samples, temperature-dependent Mössbauer spectroscopy measurements were performed. Room-temperature Mössbauer spectra are provided in Figure 3. A magnetically split sextet with IS (isomer shift) values of $\sim 0.37 \text{ mm s}^{-1}$, QS (quadrupole splitting) values of $\sim -0.21 \text{ mm s}^{-1}$, and a hyperfine magnetic field between 50.5 T and 48.5 T (Table 2) was observed for the Ga-HM, Mn-HM, Zn-HM, Nb-HM, MnCu-HM, and ZnCu-HM catalysts. These hyperfine parameters point to the presence of hematite, in line with XRD patterns²⁰. Apart from the magnetically split hematite phase, a superparamagnetic (SPM) phase with an IS of $\sim 0.34 \text{ mm s}^{-1}$ was observed in all catalysts, which points to a phase with small particles with high spin Fe^{3+} in octahedral positions,²⁵ such as in hematite or ferrihydrite²⁶. Accurate phase identification of the SPM phase cannot be obtained from these room-temperature Mössbauer spectra alone.

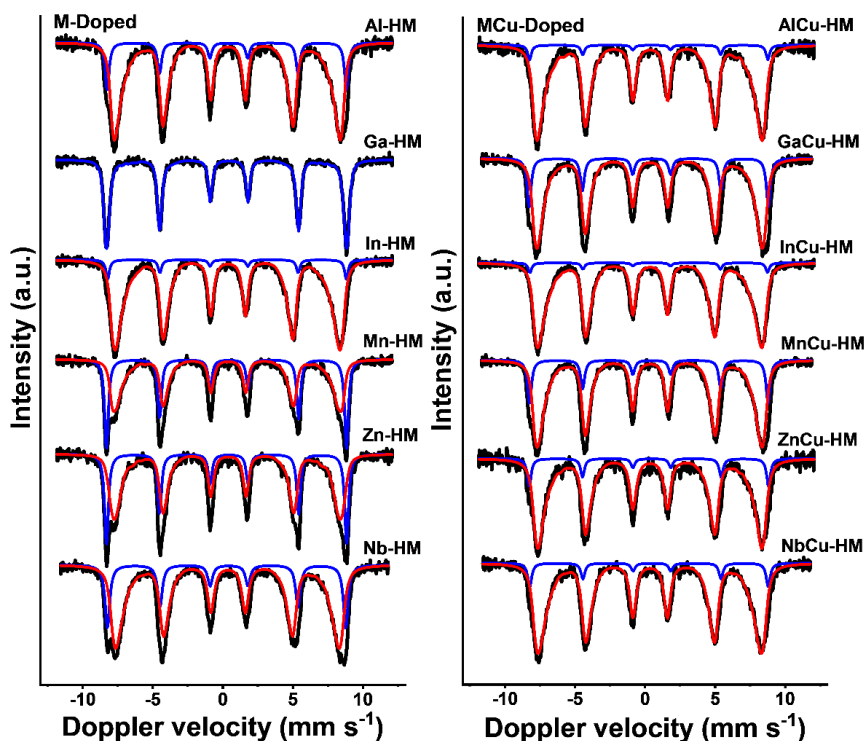


Figure 4. Mössbauer spectra of M-doped (left) and MCu-doped (right) catalysts recorded at $-269\text{ }^{\circ}\text{C}$.

Mössbauer spectra recorded at $-269\text{ }^{\circ}\text{C}$ provide deeper insight into the SPM phases (Fig. 4). Two spectral contributions are observed for all catalysts except for the HM, Cr-HM, and Ga-HM catalyst where only one sextet was observed. The results of the deconvolution of these spectra are given in Table 3. The Mössbauer parameters of the sextets ($IS \sim 0.36\text{ mm s}^{-1}$, hyperfine magnetic fields $> 52\text{ T}$) observed in all catalysts confirm the presence of a hematite phase. The second magnetically split sextet with typical IS values of $\sim 0.35\text{ mm s}^{-1}$ and a hyperfine magnetic field below 49 T is characteristic of ferrihydrite ($\text{Fe}_5\text{HO}_8 \cdot 4\text{ H}_2\text{O}$)²⁶. The data show that the amount of hematite in the catalyst precursor decreased when copper was co-doped, indicating that incorporation of copper in the iron oxide precursor prevented hematite formation during the calcination step. In the HM, Cr-HM and Ga-HM catalysts, only a hematite phase was observed while the Al-HM, In-HM, Mn-HM, Zn-HM, and Nb-HM catalysts contained both hematite and ferrihydrite. This shows that all alternative

dopants except for gallium prevent hematite formation under these conditions, suggesting their incorporation into the ferrihydrite structure.

Table 3. Mössbauer parameters of calcined catalysts of spectra recorded at -269 °C.

Sample	IS (mm s ⁻¹)	QS (mm s ⁻¹)	H (T)	Γ (mm s ⁻¹)	Phase	Spectral contribution (%)
Fe-HM ^c	0.35	0.40	53.6†	0.28	α-Fe ₂ O ₃	100
Cr-HM ^c	0.36	-0.21	52.7†	0.26	α-Fe ₂ O ₃	100
CrCu-HM ^c	0.36	-0.21	53.4	0.29	α-Fe ₂ O ₃	14
	0.36	-0.04	48.9	0.48	Fe ₅ HO ₈ · 4 H ₂ O	86
Al-HM	0.35	-0.14	53.1	0.34	α-Fe ₂ O ₃	17
	0.35	-0.05	48.3†	0.42	Fe ₅ HO ₈ · 4 H ₂ O	83
AlCu-HM	0.37*	-0.21*	52.8	0.31	α-Fe ₂ O ₃	5
	0.35	-0.05	48.2†	0.46	Fe ₅ HO ₈ · 4 H ₂ O	95
Ga-HM	0.36	-0.18	52.5†	0.30	α-Fe ₂ O ₃	100
GaCu-HM	0.37*	-0.21*	53.0	0.35	α-Fe ₂ O ₃	19
	0.35	-0.05	48.7†	0.38	Fe ₅ HO ₈ · 4 H ₂ O	81
In-HM	0.37	-0.14	52.9	0.30	α-Fe ₂ O ₃	7
	0.35	-0.04	48.2†	0.42	Fe ₅ HO ₈ · 4 H ₂ O	93
InCu-HM	0.37*	-0.21*	52.7	0.30*	α-Fe ₂ O ₃	4
	0.35	-0.03	48.0†	0.45	Fe ₅ HO ₈ · 4 H ₂ O	96
Mn-HM	0.36	-0.19	53.2	0.33	α-Fe ₂ O ₃	40
	0.36	-0.07	48.4†	0.40	Fe ₅ HO ₈ · 4 H ₂ O	60
MnCu-HM	0.37	-0.21*	52.9	0.34	α-Fe ₂ O ₃	17
	0.35	-0.05	48.4†	0.44	Fe ₅ HO ₈ · 4 H ₂ O	83
Zn-HM	0.36	-0.18	53.2	0.33	α-Fe ₂ O ₃	35
	0.36	-0.08	48.8†	0.40	Fe ₅ HO ₈ · 4 H ₂ O	65
ZnCu-HM	0.38	-0.21*	53.0	0.33	α-Fe ₂ O ₃	10
	0.36	-0.02	48.0†	0.49	Fe ₅ HO ₈ · 4 H ₂ O	90
Nb-HM	0.35	-0.17	52.8	0.40	α-Fe ₂ O ₃	25
	0.35	-0.05	48.0†	0.51	Fe ₅ HO ₈ · 4 H ₂ O	75
NbCu-HM	0.39	-0.21*	52.9	0.34	α-Fe ₂ O ₃	9
	0.35	-0.03	47.9†	0.48	Fe ₅ HO ₈ · 4 H ₂ O	91

^a Fixed values are marked with a *, average values with a †.

^b Experimental uncertainties: Isomer shift: IS ± 0.01 mm s⁻¹, quadrupole splitting: QS ± 0.01 mm s⁻¹, line width: Γ ± 0.01 mm s⁻¹, hyperfine magnetic field: H ± 0.1 T, spectral contribution: ± 3%.

^c From ⁶.

The Mössbauer spectroscopy data indicate no significant gallium incorporation into the structure, in line with the large average crystallite size and low SSA for the Ga-doped material (Table 1). Mössbauer spectroscopy allows for quantification of the ferrihydrite contents, which is not possible with XRD analysis due to the overlap of ferrihydrite and hematite signals. In addition, the presence of significant levels of a ferrihydrite phase shows that the incorporation of dopants cannot be deduced from XRD analysis, using the shift of the hematite (110) reflection discussed above, as XRD analysis is not able to discriminate between ferrihydrite and weakly crystalline hematite phases.

4.3.2 CATALYTIC ACTIVITY TESTING

The catalytic performance of the calcined catalysts was evaluated under close-to-industrial HTS conditions. Figure 5 shows the CO conversion of the M-HM and MCu-HM catalysts at 25 bar as a function of time on stream. An accelerated ageing protocol was carried out for 4 days involving activation, ageing and activity testing of the catalysts at a pressure of 25 bar using a reaction gas mixture typical for HTS of the effluent of a steam methane reformer. Initial activation was done at 450 °C for 24 h, where the slightly higher than equilibrium conversion for the MCu-doped samples is likely due to the reduction of the precursor Fe-oxides to magnetite. Catalytic performance of the various samples was then evaluated at 360 °C for 24 h, followed by an ageing step at 450 °C for 24 h and another catalytic activity test at 360 °C for 24 h. As it has been well established that the iron oxide precursor phase reduces into the active magnetite phase during the initial phases of the HTS reaction, we will denote the used catalysts as M-MG and MCu-MG. The comparison of the copper co-doped catalysts is most meaningful as the presence of copper promotes the activation of the catalyst by enhancing the partial reduction of the iron oxide precursor phases. While the Al-MG catalyst shows a higher activity than the Cr-MG sample, the CO conversion levels of their copper-promoted counterparts are very similar, especially after the high-temperature ageing step. This shows that aluminium doping of Fe-based WGS catalysts can lead to a similar activity and stability as chromium doping under industrial HTS conditions. Earlier, such promising effect of aluminium doping was reported at atmospheric pressure and for relatively short reaction times¹⁵. The other catalysts show an appreciably lower CO conversion than these two, with the activity decreasing in the order gallium > indium > manganese > zinc > niobium. As one may expect similar chemical behavior of Ga and Al, it could be that the lower performance

of the Ga-MG and GaCu-MG catalysts is due to the low gallium content and/or low incorporation level in the fresh catalyst. The HTS activity upon doping with group 13 elements decreases in the order Al > Ga > In.

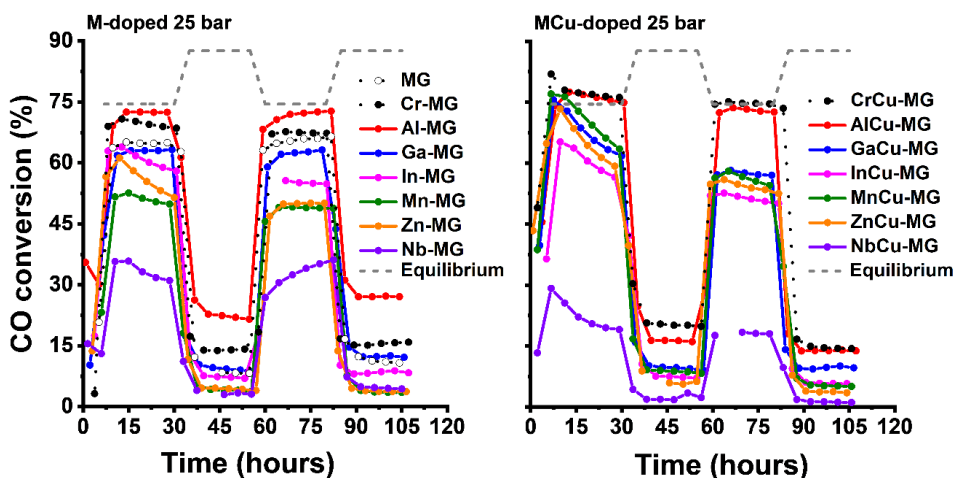


Figure 5. CO conversion under HTS conditions at 25 bar with time on stream of M-doped catalysts (left) and MCu-doped catalysts (right). The temperature was varied between 450 °C and 360 °C with 24 hour intervals. CO conversion of MG, Cr-MG, and CrCu-MG from ⁶. The initial CO conversion beyond the equilibrium conversion of the MCu-doped samples can be attributed to magnetite formation.

4.3.3 USED CATALYSTS

The XRD patterns of the discharged catalysts in Figure 6 contain reflections that can be attributed to magnetite or maghemite ($\gamma\text{-Fe}_2\text{O}_3$) phases. Despite their very similar diffraction patterns, we assign them to magnetite, as it is well accepted that exposure of Fe^{3+} -oxides to WGS conditions results in this phase ⁷. The indium- and niobium-containing samples exhibited additional reflections at $2\theta = \sim 30.5^\circ$ and $2\theta = \sim 32.3^\circ$, respectively (Fig. 6, Fig. S1). The 2θ reflection at 30.5° for the former is the (222) reflection of In_2O_3 ²⁷ and its formation is likely due to the relatively large ionic radius of indium ions (In^{3+} (oct.), 80 pm) compared to ferric ions (Fe^{3+} (oct.), 65 pm). The reflection at $2\theta = \sim 32.3^\circ$ for the niobium-containing samples can be linked to the formation of FeNbO_4 ²⁸ and FeNb_2O_6 ²⁹. Similar to the calcined catalysts, the unit cell of magnetite is contracted for the Cr-MG and Al-MG catalysts and expanded for the In-MG, Zn-MG, and Nb-MG ones. Interestingly, the lattice of the Mn-MG

catalyst is expanded, while a lattice contraction was observed in the Mn-HM catalyst. No significant differences were observed between the XRD patterns of the M-MG and MCu-MG catalysts, with the exception of the Ga-MG and GaCu-MG catalysts where lattice expansion and contraction occur, respectively. Because of the different sizes of the various dopants in tetrahedral and octahedral positions ³⁰, it is difficult to correlate the shift in 2θ values to the degree of dopant incorporation.

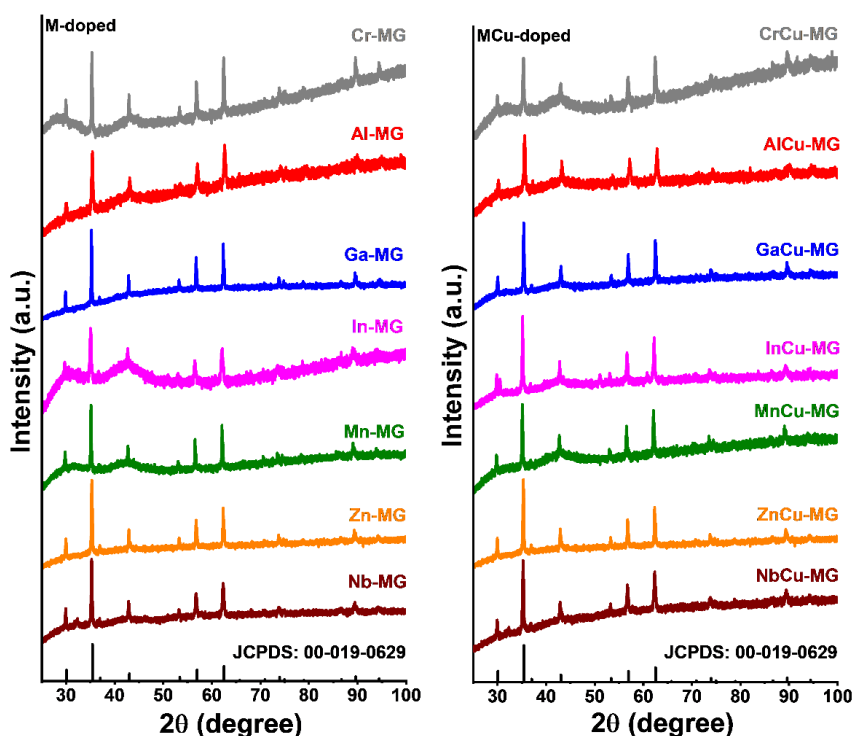


Figure 6. XRD patterns of used catalysts (M-doped, left; MCu-doped, right) after 4 days at 25 bar. JCPDS: 00-019-0629 represents magnetite.

Crystallite sizes of the used catalysts were determined by XRD line broadening analysis (Table 4). The differences in crystallite size among the copper-doped catalysts are relatively small, with the size of 30 nm of the AlCu-MG standing out. Among the catalysts not containing copper, Al-MG, In-MG, and Nb-MG contain the smallest magnetite crystallites. Clearly, the variations in the crystallite sizes cannot account for the differences in the catalytic performance. Therefore, the incorporation of dopants in magnetite was investigated in more

detail and an attempt was made to correlate this information to the activity data.

Table 4. Particle size determined from XRD (d_{XRD}) of used catalysts after 4 days at 25 bar.

Dopant	d_{XRD} (nm) ^a	
	M-MG	MCu-MG
--	74	-
Al	35	30
Ga	99	54
In	36	44
Mn	76	57
Zn	83	47
Nb	34	48
Cr	64 ^b	43 ^b

^a Calculated with the Scherrer equation from the magnetite (311) reflection.

^b From ⁶.

Mössbauer spectra of the discharged catalysts used in the activity tests for 4 days at 25 bar are shown in Figure 7. The hyperfine parameters obtained after deconvolution are collected in Table 5. A magnetite phase was observed for all used catalysts, irrespective of the dopant. The active magnetite catalyst has an inverse spinel structure (AB_2O_4) with Fe^{3+} in the tetrahedral A-sites and $\text{Fe}^{3+}/\text{Fe}^{2+}$ in the octahedral B-sites in an equimolar ratio ³¹. The magnetite HTS catalyst follows a regenerative redox mechanism for the WGS reaction where Fe^{2+} is oxidised to Fe^{3+} by H_2O and subsequently reduced back to Fe^{2+} by CO in the $\text{Fe}^{3+}/\text{Fe}^{2+}$ redox couple ¹. The room-temperature Mössbauer spectrum of magnetite can be deconvoluted into separate contributions from tetrahedral and octahedral Fe ions ⁵. The separate tetrahedral and octahedral contributions allow us to study in detail the effects of the various dopants on the tetrahedral and octahedral sites together with dopant effects on the $\text{Fe}^{3+}/\text{Fe}^{2+}$ redox couple in the octahedral sites.

Deconvolution of the Mössbauer spectra of the Al-MG and AlCu-MG catalysts yields hyperfine magnetic field values of ~ 48.0 T for the tetrahedral and ~ 44.5 T for the octahedral sites (Table 5, Fig. 7). These values are lower than those of the reference MG catalyst (48.7 T and 45.7 T, respectively, Table 5). A decrease of the hyperfine magnetic field from the bulk value of magnetite can be due to a decrease in the particle size or the incorporation of another metal in the

structure⁵. Quantification of the dopant level is in theory possible by using a set of samples with different dopant levels. However, such approach is hampered by the influence of particle size on the hyperfine magnetic field. Therefore, we discuss the incorporation levels in a qualitative sense in this work. The average crystallite sizes of 35 nm for Al-MG and 30 nm for AlCu-MG are very similar to the crystallite size of 30 nm for a 12 wt% chromium-doped catalyst recently described by us⁵. The higher hyperfine magnetic field of tetrahedral sites for this latter sample of 48.4 T is due to the preferential doping of chromium in octahedral sites. Taken together, it can be concluded that the lower tetrahedral hyperfine magnetic field for the Al-MG and AlCu-MG catalysts is due to the incorporation of aluminium in the tetrahedral sites of magnetite. The observed hyperfine magnetic field of ~ 44.4 T for the octahedral sites means that aluminium is also incorporated in octahedral sites. As the hyperfine magnetic field values and the crystallite sizes are similar for the AlCu-MG and Al-MG catalysts, we conclude that copper is not incorporated in the magnetite phase in the used AlCu-MG catalyst. The same holds for the CrCu-MG catalysts⁶. Aluminium incorporation in both tetrahedral and octahedral positions of magnetite has been reported before. Some studies reported that aluminium can be incorporated in both tetrahedral and octahedral sites³² using Mössbauer spectroscopy, whereas others indicated a preference for substitution of octahedral iron by aluminium in magnetite by measuring magnetic susceptibility³³. None of these earlier studies pertained to catalysts used under industrial HTS conditions.

The IS value of 0.66 mm s^{-1} for the octahedral sites in the Al-MG catalyst is within the experimental uncertainty of the bulk value of 0.67 mm s^{-1} in non-doped magnetite²⁶. The latter value is the result of fast electron hopping in the equimolar $\text{Fe}^{3+}/\text{Fe}^{2+}$ redox couple in the octahedral sites, which is faster than the lifetime of the relevant excited state in the Mössbauer measurement, resulting in an IS value representing an average oxidation state of $\text{Fe}^{2.5+}$ ³⁴. As IS values of typical Fe^{3+} -oxides are around 0.3 mm s^{-1} , a value lower than the bulk magnetite value of 0.67 mm s^{-1} can be explained by a higher than unity $\text{Fe}^{3+}/\text{Fe}^{2+}$ ratio⁵. The IS value of 0.64 mm s^{-1} for the octahedral sites of the AlCu-MG catalyst indicates that a small fraction of Fe^{2+} in these locations was oxidised. Such a decrease in the IS value upon copper doping was not observed for the CrCu-MG catalyst.

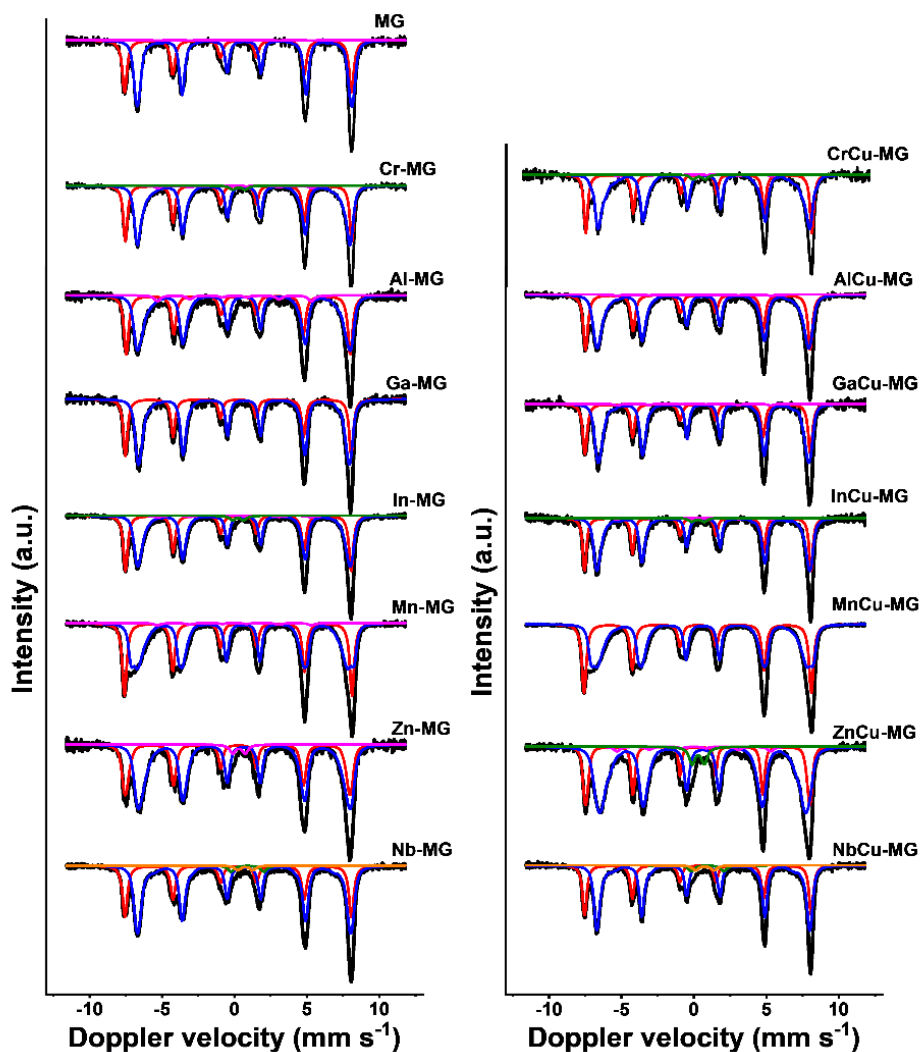


Figure 7. Room-temperature Mössbauer spectra of discharged catalysts after 4 days at 25 bar under HTS conditions.

Our hyperfine magnetic field data for the AlCu-MG catalysts show that doping of aluminium occurs in both tetrahedral and octahedral sites of the active magnetite phase. Clearly, such doping contributes to the improved thermal stability of this phase under HTS conditions, which is comparable to the stability during a 4-day test of the CrCu-MG catalyst where the chromium is incorporated exclusively in octahedral positions. This shows that the stabilisation of the high surface area of magnetite occurs irrespective of the location of dopant.

The hyperfine magnetic field values for the Ga-MG and GaCu-MG catalysts are ~ 48.4 T for the tetrahedral sites and 44.6 T for the octahedral sites (Table 5, Fig. 7). The tetrahedral hyperfine magnetic field of ~ 48.4 T is only slightly lower than that of the MG reference (48.7 T), indicating that gallium doping in tetrahedral position is likely limited. The significantly lower octahedral hyperfine magnetic field value of 44.6 T, compared to 45.7 T in the MG reference, in combination with the relatively large crystallite size observed (Table 4) points to preferential gallium incorporation into octahedral sites. The presence of gallium in the activated catalyst suggests that dopant incorporation can occur during the activation procedure since no evidence of gallium incorporation was found in the catalyst precursor. Earlier, Kohout et al.³⁵ and Rečko et al.³⁶ suggested preferential occupation of tetrahedral sites of magnetite by gallium using NMR and Mössbauer spectroscopy respectively, whereas a study by Wang et al.³⁷ indicated incorporation of gallium into both tetrahedral and octahedral sites using Mössbauer spectroscopy. These inconclusive findings might be due to the fact that the samples were prepared in different ways. The IS values of 0.66 mm s^{-1} for the octahedral sites in Ga-MG and GaCu-MG are close to the one observed for the MG catalyst, indicating that the $\text{Fe}^{3+}/\text{Fe}^{2+}$ ratio is unaffected by gallium doping.

The In-MG and InCu-MG catalysts showed similar tetrahedral hyperfine magnetic field values of ~ 48.5 T as MG (48.7 T), see Table 5. The slightly lower hyperfine magnetic field of 44.9 T for the octahedral sites in comparison to the MG reference value of 45.7 T suggests that a small amount of indium is incorporated in octahedral sites. Thus, it is likely that the extent of indium doping in the active catalyst is small and a significant amount of indium ends up in a separate In_2O_3 phase, as was confirmed by XRD analysis (Fig. 6). The octahedral IS values of 0.66 mm s^{-1} for the two indium-doped catalysts shows that indium doping has no significant effect on the $\text{Fe}^{3+}/\text{Fe}^{2+}$ redox couple. It is therefore likely that the relatively large size of In^{3+} compared to Fe^{3+} results in phase segregation during the activation treatment, although In incorporation in the calcined precursor was confirmed by XRD and Mössbauer spectroscopy. Likely, this additional In_2O_3 phase blocks the active magnetite sites at the surface, explaining the much lower activity in comparison to the Cr-MG sample.

In the Mn-MG and MnCu-MG catalysts, hyperfine magnetic field values of ~ 48.7 T and ~ 45.0 T were observed for the tetrahedral and octahedral sites of

magnetite, respectively (Table 5). These values are relatively close to those of the reference MG catalyst (48.7 T and 45.7 T). Nevertheless, the lower octahedral value for the manganese-doped samples points to incorporation of manganese into the magnetite structure. A substantial decrease in the IS values of the octahedral sites to 0.58 mm s^{-1} compared to the bulk value of 0.67 mm s^{-1} points to an increased $\text{Fe}^{3+}/\text{Fe}^{2+}$ ratio, which can be due to the replacement of octahedral Fe^{2+} for Mn^{2+} .⁵ Incorporation of Mn^{2+} for Fe^{2+} into octahedral sites of magnetite was reported before by Sorescu et al.³⁸ using Mössbauer spectroscopy, in line with our results. This does not exclude however the possibility that some Mn^{3+} ions replace Fe^{3+} ions in octahedral sites as well. These results show that doping M^{2+} ions with an octahedral site preference can lead to a significant distortion of the $\text{Fe}^{3+}/\text{Fe}^{2+}$ redox couple. Although Mn^{2+} incorporation occurs in a similar way as Cr^{3+} incorporation by replacing octahedral Fe ions in magnetite, no improved catalyst activity or stability was observed (Fig. 5). This highlights the complex correlation between dopant incorporation and catalyst performance.

In the Zn-MG catalyst, a hyperfine magnetic field value of 48.0 T (Table 5) was observed for the tetrahedral sites of magnetite. This, in combination with relatively large crystallites (Table 4), indicates the incorporation of zinc into the tetrahedral sites, similar to the aluminium-doped catalysts. A tetrahedral site preference was observed before for zinc-doped magnetite^{39,40}. The hyperfine magnetic field of the octahedral sites decreased in the Zn-MG catalyst (44.4 T), which points to zinc incorporation in octahedral sites as well. Zinc can occupy both the tetrahedral and octahedral sites of magnetite at high zinc content⁴¹ and it has been pointed out before that the preparation procedure can influence the site preference⁴². The incorporation of divalent zinc into the tetrahedral sites of magnetite where it replaces trivalent iron, would lead to a charge imbalance. Wen et al.⁴³ proposed that the charge imbalance can be resolved by partial oxidation of Fe^{2+} to Fe^{3+} in the octahedral sites. This leads to the $(\text{Zn}_x^{2+}\text{Fe}_{1-x}^{3+})[\text{Fe}_{1-x}^{2+}\text{Fe}_{1+x}^{3+}]\text{O}_4$ structure, where the tetrahedral sites are shown in parentheses and the octahedral sites in brackets. In support of this model are the observations of Mendoza Zélis et al.⁴⁰ of a more ferric-like IS in the octahedral sites of their samples with increasing zinc doping in tetrahedral sites. Walz et al.⁴⁴ suggested a different model where zinc was incorporated into both the tetrahedral and octahedral sites of vacancy(Δ)-doped magnetite $(\text{Zn}_{x-y}^{2+}\text{Fe}_{1-x+y}^{3+})[\text{Zn}_y^{2+}\text{Fe}_{1-x}^{2+}\text{Fe}_{1+x-y}^{3+}]_{-\Delta}\text{O}_4$. They proposed that, at low zinc

content, Zn^{2+} ions can migrate to octahedral vacancies, resulting in incorporation into both lattice sites of the spinel. The IS value of 0.66 mm s^{-1} measured for the octahedral sites of our Zn-MG catalyst is similar to that of bulk magnetite (0.67 mm s^{-1}). As such, this implies that the Wen model cannot describe the cation arrangement in our Zn-MG catalyst. Instead, the Walz model better describes the observed decrease in the hyperfine magnetic field values of the tetrahedral and octahedral sites for our Zn-MG catalyst (Table 5).

A hyperfine magnetic field value of 48.0 T was observed for the tetrahedral sites of the ZnCu-MG catalyst. The decrease from the bulk magnetite value can again be attributed to the incorporation of zinc in tetrahedral sites. Different from the Zn-MG catalyst, the copper-doped sample also led to a substantial decrease in the hyperfine magnetic field of the octahedral sites to 43.4 T. The lower hyperfine magnetic field in the octahedral sites is accompanied by a more ferric-like IS value of 0.62 mm s^{-1} . This could indicate the incorporation of Cu^{2+} into the zinc-doped magnetite structure in place of Fe^{2+} . However, copper incorporation in magnetite has not been observed before for other copper-doped magnetite samples. It is therefore more likely that the lower IS value in the octahedral sites can be explained by the Wen model, where partial oxidation in the octahedral sites leads to a lower IS. The lower hyperfine magnetic field is due to the presence of small magnetite particles, which is supported by the substantial SPM contribution for ZnCu-MG (Fig. 7, Table 5). Thus, doping magnetite with divalent ions with a preference for tetrahedral sites results in a complex structure where the charge imbalance is compensated from the octahedral sites by partial oxidation of Fe^{2+} to Fe^{3+} , as described by Wen et al.

In the Mössbauer spectra of the Nb-MG and NbCu-MG catalysts (Fig. 7), two SPM doublets and two magnetically split sextets were observed. The two SPM doublets with IS values of 0.75 mm s^{-1} and $\sim 0.92 \text{ mm s}^{-1}$ and QS values of $1.06\text{--}1.29 \text{ mm s}^{-1}$ and $2.24\text{--}2.29 \text{ mm s}^{-1}$, respectively, are typical for an FeNb_2O_6 phase⁴⁵. Hyperfine magnetic field values of 48.6 T and $\sim 45.0 \text{ T}$ were observed for the magnetically split sextets. The value of 48.6 T is close to that of non-doped MG, indicating that no niobium substitution occurred in tetrahedral sites. The hyperfine magnetic field of $\sim 45.0 \text{ T}$ observed for the octahedral sites was slightly lower than that of the reference MG catalyst, indicating some niobium incorporation in octahedral sites of magnetite. The relatively low influence of niobium on the hyperfine magnetic field values is most likely due

to the segregation into a separate phase. IS values of 0.65-0.66 mm s⁻¹ for the octahedral sites indicate that no significant change in the Fe³⁺/Fe²⁺ redox couple occurred upon niobium doping. This might be due to the low doping level but also due to the replacement of an equal amount of Fe²⁺ and Fe³⁺ ions for one Nb⁵⁺ ion. The formation of a separate FeNb₂O₆ phase during activation under industrially relevant HTS conditions and the low catalytic performance mean that niobium is unsuitable to replace chromium in HTS catalysts.

Table 5. Mössbauer parameters of discharged catalysts after exposure to HTS conditions for 4 days at 25 bar.

Sample	IS (mm s ⁻¹)	QS (mm s ⁻¹)	H (T)	Γ (mm s ⁻¹)	Phase	(%) ^c
MG ^b	0.26	-0.03	48.7	0.38	Fe ₃ O ₄ (tet)	37
	0.68	-0.03	45.7†	0.32	Fe ₃ O ₄ (oct)	62
	0.00*	0.00*	33.0*	0.50*	α-Fe	1
Cr-MG ^b	0.28	0.00	48.6	0.34	Fe ₃ O ₄ (tet)	35
	0.64	-0.01	44.6†	0.32	Fe ₃ O ₄ (oct)	61
	0.00*	0.00*	33.0*	0.50*	α-Fe	2
	0.30*	0.86	-	0.50*	Fe ³⁺ SPM	2
CrCu-MG ^b	0.29	0.00	48.4	0.32	Fe ₃ O ₄ (tet)	34
	0.64	-0.03	44.2†	0.30	Fe ₃ O ₄ (oct)	62
	0.00*	0.00*	33.0*	0.50*	α-Fe	2
	0.30*	0.76	-	0.50*	Fe ³⁺ SPM	2
Al-MG	0.28	-0.02	48.0	0.37	Fe ₃ O ₄ (tet)	36
	0.66	-0.02	44.5	0.35	Fe ₃ O ₄ (oct)	59
	0.00*	0.00*	33.0*	0.50*	α-Fe	5
AlCu-MG	0.28	-0.01	48.1	0.37	Fe ₃ O ₄ (tet)	36
	0.64	-0.02	44.5†	0.35	Fe ₃ O ₄ (oct)	63
	0.00*	0.00*	33.0*	0.50*	α-Fe	1
Ga-MG	0.27	-0.01	48.4	0.34	Fe ₃ O ₄ (tet)	35
	0.66	0.00	44.6†	0.30	Fe ₃ O ₄ (oct)	65
GaCu-MG	0.27	-0.02	48.3	0.35	Fe ₃ O ₄ (tet)	34
	0.67	0.01	44.6†	0.29	Fe ₃ O ₄ (oct)	64
	0.00*	0.00*	33.0*	0.50*	α-Fe	2
In-MG	0.28	-0.02	48.4	0.35	Fe ₃ O ₄ (tet)	38
	0.66	0.00	44.9†	0.32	Fe ₃ O ₄ (oct)	58
	0.00*	0.00*	33.0*	0.50*	α-Fe	2
	0.25	0.77	-	0.50*	Fe ³⁺ SPM	2

Table 5. Continued.

Sample	IS (mm s ⁻¹)	QS (mm s ⁻¹)	H (T)	Γ (mm s ⁻¹)	Phase	(%) ^c
InCu-MG	0.28	-0.02	48.5	0.30	Fe ₃ O ₄ (tet)	35
	0.66	0.00	44.9†	0.30	Fe ₃ O ₄ (oct)	61
	0.00*	0.00*	33.0*	0.50*	α-Fe	2
	0.29	0.87	-	0.50*	Fe ³⁺ SPM	2
Mn-MG	0.28	-0.03	48.8	0.36	Fe ₃ O ₄ (tet)	39
	0.58	-0.04	45.1†	0.31	Fe ₃ O ₄ (oct)	59
	0.00*	0.00*	33.0*	0.50*	α-Fe	2
MnCu-MG	0.28	-0.03	48.7	0.36	Fe ₃ O ₄ (tet)	39
	0.59	-0.04	45.0†	0.32	Fe ₃ O ₄ (oct)	61
Zn-MG	0.25	-0.06	48.0	0.33	Fe ₃ O ₄ (tet)	34
	0.66	0.04	44.4†	0.38	Fe ₃ O ₄ (oct)	63
	0.31	0.86	-	0.50*	Fe ³⁺ SPM	3
ZnCu-MG	0.27	-0.01	48.0	0.24	Fe ₃ O ₄ (tet)	26
	0.62	0.00	43.4†	0.39	Fe ₃ O ₄ (oct)	66
	0.00*	0.00*	33.0*	0.50*	α-Fe	3
	0.30*	0.84	-	0.50*	Fe ³⁺ SPM	5
Nb-MG	0.27	-0.03	48.6	0.40	Fe ₃ O ₄ (tet)	33
	0.66	0.02	45.1†	0.36	Fe ₃ O ₄ (oct)	62
	0.90	2.29	-	0.50*	FeNb ₂ O ₆ (I)	3
	0.75*	1.06	-	0.50*	FeNb ₂ O ₆ (II)	2
NbCu-MG	0.28	0.00	48.6	0.34	Fe ₃ O ₄ (tet)	33
	0.65	0.00	44.9†	0.31	Fe ₃ O ₄ (oct)	61
	0.94	2.24	-	0.50*	FeNb ₂ O ₆ (I)	3
	0.75*	1.29	-	0.50*	FeNb ₂ O ₆ (II)	3

Fixed values are marked with an asterisk (*), average values of distribution fits with (†).

^a Experimental uncertainties: IS ± 0.01 mm s⁻¹, QS ± 0.01 mm s⁻¹, line width: Γ ± 0.01 mm s⁻¹, hyperfine magnetic field: H ± 0.1 T, spectral contribution: ± 3%.

^b From ⁶.

^c Spectral contribution

The surface of the catalysts aged under HTS conditions for 4 days at 25 bar was investigated by XPS. The Fe 2p spectra of the M- and MCu-doped catalysts are shown in Figure 8. The Fe³⁺ and Fe²⁺ satellite peaks expected for the corresponding pure Fe₂O₃ and Fe_{1-y}O oxide at binding energies of 719 eV and 715.5 eV,⁴⁶ respectively, are not observed in the XPS spectra of the used catalysts. This is typical for materials in which magnetite is the dominant iron oxide phase. It also implies that the surface of the catalysts is very similar to the bulk magnetite structure as shown by XRD and Mössbauer spectroscopy.

XPS spectra of valence states of the dopants are provided in the supporting information (Fig. S2). All dopants are present in the expected oxidation states.

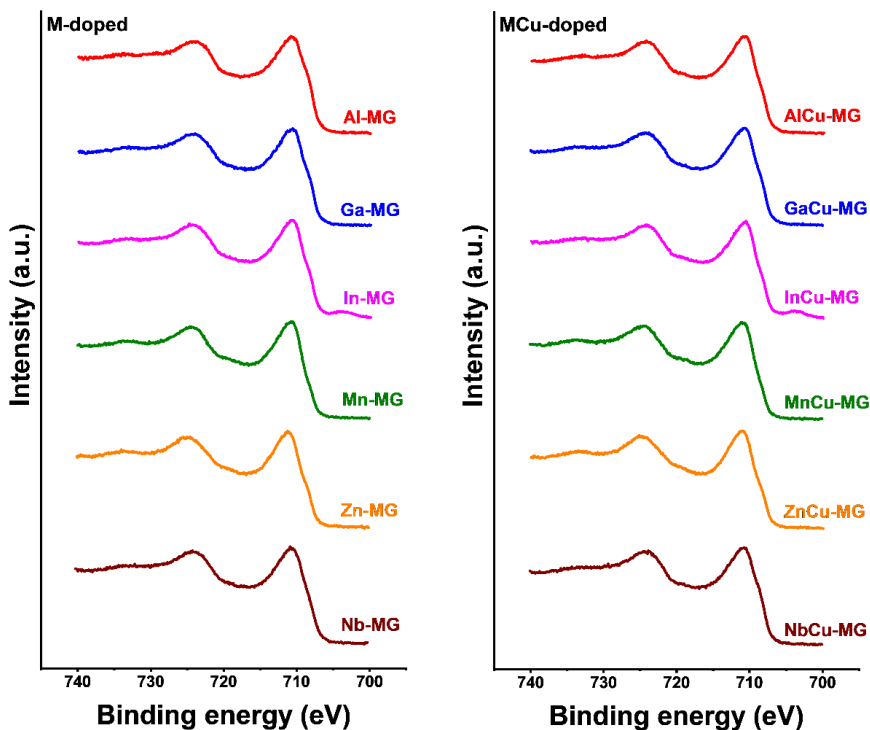


Figure 8. Fe 2p region of discharged M-MG and MCu-MG catalysts after exposure to HTS conditions for 4 days at 25 bar. The small peak observed in the Fe 2p regions of the In-MG and InCu-MG spectra at BE = ~ 703 eV results from the In 3p peak.

The Cu 2p and Cu LMM regions of used MCu-doped catalysts are presented in Figure 9. The broad peaks at BE = 932 eV and BE = 952 eV in the Cu 2p region can be attributed to the Cu $2p_{3/2}$ and Cu $2p_{1/2}$ states, respectively⁴⁷. These values can be attributed to Cu⁰ or Cu⁺ species. The absence of Cu²⁺ is underpinned by the absence of a satellite feature at BE = ~ 942 eV⁴⁷. Thus, it is not likely that Cu²⁺ is incorporated in the octahedral sites of ZnCu-MG. Inspection of the Cu LMM region (Fig. 9) shows a peak at a kinetic energy of ~ 917 eV⁴⁸ in all MCu-MG catalysts, which implies that copper is mainly present as Cu⁺. The presence of Cu⁺ instead of Cu⁰ in activated HTS catalysts contradicts a recent *in situ* study performed by the Wachs group¹⁰. In our earlier work on chromium-copper doped catalysts, we also demonstrated that copper is

present in the metallic state in activated catalysts ⁶. The observation of Cu⁺ in our used catalysts is likely the result of accidental oxidation during the shutdown procedure.

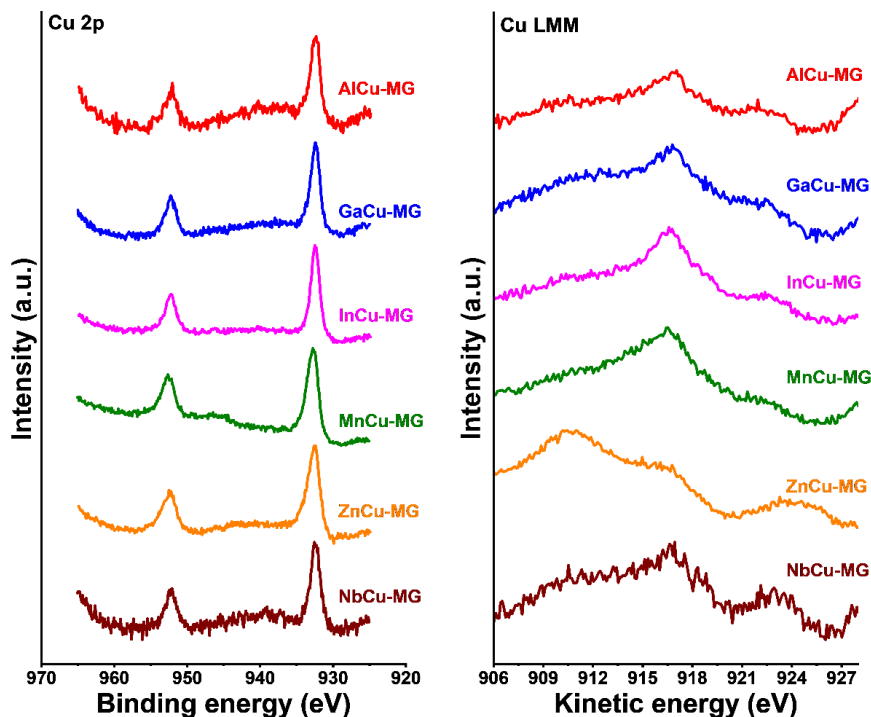


Figure 9. Cu 2p and Cu LMM regions of discharged MCu-MG catalysts after exposure to HTS conditions for 4 days at 25 bar.

4.4 CONCLUSIONS

Iron oxide phases in the precursor and activated WGS catalysts were promoted by a range of metals in order to establish their suitability to replace chromium. Emphasis was on establishing structure and performance under close to practical conditions of the high-temperature WGS reaction. Similar to the non-doped hematite precursor, doping with chromium and gallium yielded hematite as the main precursor phase after calcination. Doping with aluminium, indium, manganese, zinc, and niobium resulted in a mixture of hematite and ferrihydrite, the latter in the form of relatively small crystallites. All calcined copper-promoted samples contained mainly ferrihydrite. The most suitable substituent for chromium in terms of catalytic performance is aluminium. Comparing the copper co-promoted catalysts under HTS conditions using an

accelerated ageing protocol, it can be concluded that aluminium can replace chromium with nearly similar catalytic performance. The other substituents result in a significantly faster deactivation with the HTS performance decreasing in the order gallium > indium > manganese > zinc > niobium. The location of the dopants in the (predominantly) magnetite structure of the activated catalysts was further investigated by Mössbauer spectroscopy. Aluminium was incorporated in both tetrahedral and octahedral sites of magnetite in contrast to the chromium dopant which exclusively substitutes octahedral iron. Aluminium doping did not affect the $\text{Fe}^{3+}/\text{Fe}^{2+}$ ratio, while chromium doping prevented Fe^{2+} formation during activation. The doping situation for the other catalysts varied with the doping metal. For indium and niobium, segregated promoter metal oxide phases were observed in addition to magnetite. Overall, the following generalisations can be made about the rational design of chromium-free HTS catalysts:

- (1) The incorporation of trivalent ions of similar size to octahedral trivalent iron, such as aluminium, chromium, and gallium into the magnetite structure results in active and stable WGS catalysts, irrespective of dopant incorporation in tetrahedral or octahedral positions. Aluminium doping leads to comparable activity and stability as chromium doping in a four-day test under HTS conditions at 25 bar.
- (2) Large trivalent ions, such as indium, do not remain in the iron oxide structure upon reduction of the Fe^{3+} -oxide precursor to magnetite, resulting in segregated promoter oxide phases. Elements that can form separate iron-M-oxide phases under reducing conditions, such as niobium, are also unsuited to replace chromium in HTS catalysts.
- (3) The incorporation of divalent ions with a tetrahedral site preference, such as zinc, results in complex structures where the charge imbalance is compensated by partial oxidation of Fe^{2+} in octahedral sites. No beneficial effect on WGS performance was observed for the Zn-promoted catalysts.
- (4) The incorporation of divalent ions with an octahedral site preference, such as Mn^{2+} , leads to a distortion of the octahedral $\text{Fe}^{3+}/\text{Fe}^{2+}$ redox couple because of the replacement of Fe^{2+} by Mn^{2+} . Unlike substitution with trivalent ions with an octahedral site preference, Mn^{2+} substitution has a detrimental effect on HTS catalytic activity.

REFERENCES

- [1] M. Zhu; I.E. Wachs Iron-Based Catalysts for the High-Temperature Water-Gas Shift (HT-WGS) Reaction: A Review. *ACS catalysis* **2016**, *6*, 722-732.
- [2] D.W. Lee; M.S. Lee; J.Y. Lee; S. Kim; H.J. Eom; D.J. Moon; K.Y. Lee The review of Cr-free Fe-based catalysts for high-temperature water-gas shift reactions. *Catalysis Today* **2013**, *210*, 2-9.
- [3] D.S. Newsome The Water-Gas Shift Reaction. *Catalysis Reviews Science and Engineering* **1980**, *21*, 275-318.
- [4] M.V. Twigg *Catalyst handbook*; 2 ed.; 1989.
- [5] M.I. Ariëns; V. Chlan; P. Novák; L.G.A. van de Water; A.I. Dugulan; E. Brück; E.J.M Hensen The Role of Chromium in Iron-based High-Temperature Water-Gas Shift Catalysts under Industrial Conditions. *Applied Catalysis B: Environmental* **2021**, *297*, 120465.
- [6] M.I. Ariëns; L.G.A. van de Water; A.I. Dugulan; E. Brück; E.J.M Hensen Copper Promotion of Chromium-Doped Iron Oxide Water-Gas Shift Catalysts under Industrially Relevant Conditions. *Journal of Catalysis* **2022**, *405*, 391-406.
- [7] C.J. Keturakis; M. Zhu; E.K. Gibson; M. Daturi; F. Tao; A.I. Frenkel; I.E. Wachs Dynamics of CrO₃-Fe₂O₃ Catalysts during the High-Temperature Water-Gas Shift Reaction: Molecular Structures and Reactivity. *ACS catalysis* **2016**, *6*, 4786-4798.
- [8] M. do Carmo Rangel; R.M. Sassaki; F. Galembeck Effect of chromium on magnetite formation. *Catalysis Letters* **1995**, *33*, 237-254.
- [9] M. Zhu; P. Tian; R. Kurtz; T. Lunkenbein; J. Xu; R. Schlogl; I.E. Wachs; Y.F. Han Strong Metal-Support Interactions between Copper and Iron Oxide during the High-Temperature Water-Gas Shift Reaction. *Angewandte chemie* **2019**, *131*, 9181-9185.
- [10] M. Zhu; T.C.R. Rocha; T. Lunkenbein; A. Knop-Gericke; R. Schlogl; I.E. Wachs Promotion Mechanisms of Iron Oxide-Based High Temperature Water-Gas Shift Catalysts by Chromium and Copper. *ACS catalysis* **2016**, *6*, 4455-4464.
- [11] C. Pellerin; S.M. Booker Reflections on hexavalent chromium: health hazards of an industrial heavyweight. *Environmental Health Perspectives* **2000**, *108*, 402-407.

- [12] M. Zhu; Ö. Yalçın; I.E. Wachs Revealing structure-activity relationships in chromium free high temperature shift catalysts promoted by earth abundant elements. *Applied Catalysis B: Environmental* **2018**, *232*, 205-212.
- [13] G.K. Reddy; K. Gunasekara; P. Boolchand; P.G. Smirniotis Cr- and Ce-Doped Ferrite Catalysts for the High Temperature Water-Gas Shift Reaction: TPR and Mössbauer Spectroscopic Study. *Journal of Physical Chemistry C* **2011**, *115*, 920-930.
- [14] M. Zhu; I.E. Wachs A perspective on chromium-Free iron oxide-based catalysts for high temperature water-gas shift reaction. *Catalysis Today* **2018**, *311*, 2-7.
- [15] F. Meshkani; M. Rezaei Preparation of nanocrystalline metal (Cr, Al, Mn, Ce, Ni, Co and Cu) modified ferrite catalysts for the high temperature water gas shift reaction. *Renewable Energy* **2015**, *74*, 588-589.
- [16] S. Natesakhawat; X. Wang; L. Zhang; U.S. Ozkan Development of chromium-free iron-based catalysts for high-temperature water-gas shift reaction. *Journal of Molecular Catalysis A: Chemical* **2006**, *260*, 82-94.
- [17] T. Popa; G. Xu; T.F. Barton; M.D. Argyle High temperature water gas shift catalysts with alumina. *Applied Catalysis A: General* **2010**, *379*, 15-23.
- [18] G.K. Reddy; P. Boolchand; P.G. Smirniotis Sulfur tolerant metal doped Fe/Ce catalysts for high temperature WGS reaction at low steam to CO ratios – XPS and Mössbauer spectroscopic study. *Journal of Catalysis* **2011**, *282*, 258-269.
- [19] G.K. Reddy; P. Boolchand; P.G. Smirniotis Unexpected Behavior of Copper in Modified Ferrites during High Temperature WGS Reaction - Aspects of Fe³⁺ Fe²⁺ Redox Chemistry from Mössbauer and XPS Studies. *Journal of Physical Chemistry C* **2012**, *116*, 11019-11031.
- [20] A. Khan; P.G. Smirniotis Relationship between temperature-programmed reduction profile and activity of modified ferrite-based catalysts for WGS reaction. *Journal of Molecular Catalysis A: Chemical* **2008**, *280*, 43-51.
- [21] D. Devaiah; P.G. Smirniotis Effects of the Ce and Cr Contents in Fe-Ce-Cr Ferrite Spinel on the High-Temperature Water-Gas Shift Reaction. *Industrial & Engineering Chemistry Research* **2017**, *56*, 1772-1781.
- [22] F. Meshkani; M. Rezaei Preparation of mesoporous nanocrystalline alkali promoted chromium free catalysts (Fe₂O₃-Al₂O₃- NiO) for a high temperature water gas shift reaction. *RSC Advances* **2015**, *5*, 9955-9964.

- [23] D. Damma; D. Jampaiah; A. Welton; P. Boolchand; A. Arvanitis; J. Dong; P.G. Smirniotis Effect of Nb modification on the structural and catalytic property of Fe/Nb/M (M = Mn, Co, Ni, and Cu) catalyst for high temperature water-gas shift reaction. *Catalysis Today* **2019**, *355*, 921-931.
- [24] F. Meshkani; M. Rezaei Preparation of Mesoporous Chromium Promoted Magnetite Based Catalysts for High Temperature Water Gas Shift Reaction. *Industrial & Engineering Chemistry Research* **2015**, *45*, 1236-1242.
- [25] V.P. Santos; T.A. Wezendonk; J.J. Delgado Jaén; A.I. Dugulan; M.A. Nasalevich; H.U. Islam; A. Chojecki; S. Sartipi; X. Sun; A.A. Hakeem; A.C.J. Koeken; M. Ruitenbeek; T. Davidian; G.R. Meima; G. Sankar; F. Kapteijn; M. Makkee; J. Gascon Metal organic framework-mediated synthesis of highly active and stable Fischer-Tropsch catalysts. *Nature Communications* **2015**, *6*, 6451.
- [26] R.M. Cornel; U. Schwertmann The Iron Oxides: Structures, Properties, Reactions, Occurrences and Uses; 2003.pp. 155-156.
- [27] C. Liang; G. Meng; Y. Lei; F. Phillipp; L. Zhang Catalytic Growth of Semiconducting In₂O₃ Nanofibers. *Advanced Materials* **2001**, *13*, 1330-1333.
- [28] P. Dhak; D. Dhak; M. Das; T. Subashchandrabose; P. Pramanik A novel synthesis of FeNbO₄ nanorod by hydrothermal process. *Journal of Nanoparticle Research* **2011**, *13*, 4153-4159.
- [29] A.N. Mansurova; R.I. Gulyaeva; V.M. Chumarev; S.A. Petrova High-temperature heat capacity and temperatures of phase transformations of the FeNb₂O₆. *Journal of Alloys and Compounds* **2017**, *695*, 2483-2487.
- [30] R.D. Shannon Revised Effective Ionic Radii and Systematic Studies of Interatomic Distances in Halides and Chalcogenides. *Acta Crystallographica* **1976**, *A32*, 751-767.
- [31] G.S. Parkinson Iron oxide surfaces. *Surface Science Reports* **2016**, *71*, 272-365.
- [32] U. Schwertmann; E. Murad The Influence of Aluminum on Iron Oxides: XIV. Al-Substituted Magnetite Synthesized at Ambient Temperatures. *Clays and Clay Minerals* **1990**, *38*, 196-202.
- [33] Ó. Alejos; C. de Francisco; J.M. Muñoz; P. Hernández; C. Torres; J.I. Íñiguez; L. Torres The magnetic disaccommodation in aluminium ferrites. *Journal of Magnetism and Magnetic Materials* **1999**, *202*, 141-149.

- [34] C.A. Gorski; M.M. Scherer Influence of Magnetite Stoichiometry on Fe^{II} Uptake and Nitrobenzene Reduction. *Environmental Science and Technology* **2009**, *43*, 3675-3680.
- [35] J. Kohout; E. Gamaliy; H. Štěpánková; J. English; V. Procházka; V.A.M. Brabers NMR of ⁵⁷Fe, ⁶⁹Ga and ⁷¹Ga in Ga substituted magnetite. *Journal of Magnetism and Magnetic Materials* **2005**, *290-291*, 1018-1020.
- [36] K. Recko; U. Klekotka; B. Kalska-Szostko; D. Soloviov; D. Satula; J. Waliszewski Properties of Ga-Doped Magnetite Nanoparticles. *ACTA PHYSICA POLONICA A* **2018**, *134*, 998-1002.
- [37] J. Wang; T. Deng; C.Q. Yang; W. Wang Synthesis of gallium bearing magnetic particles from aqueous solution: influence of mixing procedure of initial solution and the ratio of Ga/Fe. *Journal of Alloys and Compounds* **2008**, *450*, 276-283.
- [38] M. Sorescu; D. Tarabasanu-Mihaila; L. Diamandescu A Mössbauer study of manganese-doped magnetite. *Materials Letters* **2003**, *57*, 1867-1869.
- [39] J.M. Byrne; V.S. Coker; E. Cespedes; P.L. Wincott; D.J. Vaughan; R.A.D. Patrick; G. van der Laan; E. Arenholz; F. Tuna; M. Bencsik; J.R. Lloyd; N.D. Telling Biosynthesis of Zinc Substituted Magnetite Nanoparticles with Enhanced Magnetic Properties. *Advanced Functional Materials* **2014**, *24*, 2518-2529.
- [40] P. Mendoza Zélis; G.A. Pasquevich; S.J. Stewart; M.B. Fernández van Raap; J. Apesteguy; I.J. Bruvera; C. Laborde; B. Pianciola; S. Jacobo; F.H. Sánchez Structural and magnetic study of zinc-doped magnetite nanoparticles and ferrofluids for hyperthermia applications. *Journal of Physics D: Applied Physics* **2013**, *46*, 125006.
- [41] X. Liu; J. Liu; S. Zhang; Z. Nan; Q. Shi Structural, Magnetic, and Thermodynamic Evolutions of Zn-Doped Fe₃O₄ Nanoparticles Synthesized Using a One-Step Solvothermal Method. *Journal of Physical Chemistry C* **2016**, *120*, 1328-1341.
- [42] H. Ito; S. Amagasa; N. Nishida; Y. Kobayashi; Y. Yamada Wet chemical synthesis of zinc-iron oxide nanocomposite. *Hyperfine Interactions* **2017**, *238*, 79-1-79-9.
- [43] M. Wen; Q. Li; Y. Li Magnetic, electronic and structural properties of Zn_xFe_{3-x}O₄. *Journal of Electron Spectroscopy and Related Phenomena* **2006**, *153*, 65-70.
- [44] F. Walz; L. Torres; C. de Francisco; J. Iñiguez; H. Kronmüller Analysis of Magnetic After-Effect Spectra in Zinc Ferrites. *physica status solidi (a)* **1997**, *163*, 233-245.

- [45] M.V. Cagnoli; A.M. Alvarez; N.G. Gallegos; J.F. Bengoa; C.D. Duarte de Souza; M. Schmal; S.G. Marchetti Mössbauer and XPS spectroscopies studies of SMSI effect on Fe/Nb₂O₅ catalysts for the Fischer-Tropsch synthesis. *Applied Catalysis A: General* **2007**, *326*, 113-119.
- [46] T. Yamashita; P. Hayes Analysis of XPS spectra of Fe²⁺ and Fe³⁺ ions in oxide materials. *Applied Surface Science* **2008**, *254*, 2441-2449.
- [47] I. Platzman; R. Brener; H. Haick; R. Tannenbaum Oxidation of Polycrystalline Copper Thin Films at Ambient Conditions. *Journal of Physical Chemistry C* **2008**, *112*, 1101-1108.
- [48] Y. Gao; E.J.M. Hensen Highly active and stable spinel-oxide supported gold catalyst for gas-phase selective aerobic oxidation of cyclohexanol to cyclohexanone. *Catalysis Communications* **2018**, *117*, 53-56.

5

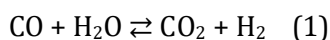
IN SITU MÖSSBAUER SPECTROSCOPY

ABSTRACT

The influence of chromium and aluminium doping on over-reduction during the activation of iron-oxide based water-gas shift catalysts was investigated for the first time using *in situ* Mössbauer spectroscopy. Copper co-doping of these catalysts was investigated also. *In situ* Mössbauer spectra were recorded of catalysts exposed to industrially relevant gas compositions with increasingly reducing R factors $R = (\text{H}_2 + \text{CO})/(\text{CO}_2 + \text{H}_2\text{O})$ for 1 hour at 450 °C. *In situ* Mössbauer spectra showed the presence of α -Fe and cementite phases after exposing a non-doped iron-oxide catalyst to process conditions with an R factor of 2.09. These phases were only observed at $R = 4.60$ for a chromium doped catalyst, showing that chromium stabilises the catalyst from over-reduction. In a chromium copper co-doped catalyst, the over reduction was slightly enhanced to $R = 2.88$. α -Fe formation was observed at $R = 1.64$ in an aluminium doped catalyst while cementite formation occurred at $R = 2.09$, showing that over reduction was enhanced while carburisation was delayed by the presence of aluminium. Co-doping copper on the aluminium doped catalyst showed cementite formation to $R = 2.09$, the same as a non-doped catalyst.

5.1 INTRODUCTION

The water-gas shift (WGS) reaction (1) is industrially employed to increase hydrogen production from natural gas after steam methane reforming (SMR) ¹⁻³. High CO conversion is achieved by separating the exothermic reaction into two processes ¹. Most CO is removed during the high temperature (water-gas) shift (HTS) reaction over a copper/chromium doped iron-oxide catalyst between 360-450 °C. The concentration of CO in the effluent (2-4%) is then lowered to ~0.1% in a low temperature (water-gas) shift (LTS) step over a copper based catalyst between 190-250 °C ^{1,4}.



The active industrial HTS catalyst consists of magnetite (Fe_3O_4) and is formed by exposing a Fe^{3+} -oxide or -oxyhydroxide precursor to WGS conditions ⁵⁻⁷. Chromium and copper are added to this catalyst as promoters. Chromium exists as Cr^{6+} and Cr^{3+} in the calcined precursor and is incorporated into the magnetite structure during activation, during this process the Cr^{6+} species are reduced to Cr^{3+} ⁷. The presence of chromium prevents thermal agglomeration of the active phase, and limits over-reduction of the active magnetite phase to $\alpha\text{-Fe}$, and FeC_x ^{1,4-6,8}. The formation of $\alpha\text{-Fe}$ and FeC_x is undesired, because they can catalyse unwanted methanation and Fischer-Tropsch side reactions ⁹. Over-reduction is also associated with catalyst pellet degradation, which can induce a significant pressure drop in industrial reactors ⁹. Copper is added to commercial catalysts to enhance CO conversion via a chemical promotion mechanism ^{6,8}. The Wachs group recently showed that divalent copper, present in the calcined catalyst precursor, is removed from the Fe-Cr structure during activation, resulting in Cu^0 nanoparticles partially covered by an iron oxide over-layer on the active chromium-doped magnetite catalyst ^{8,10}. This results in active sites that are more active than the separate iron oxide and metallic copper sites ¹¹.

The presence of hexavalent chromium in the fresh catalyst has inspired researchers to investigate alternative dopants ^{2,12-16}. Several groups ^{13,17,18} have shown that aluminium doping resulted in high activity at atmospheric pressure after relatively short reaction times. We recently demonstrated that industrially relevant chromium/copper- and aluminium/copper-doped

catalysts have similar CO conversion at 25 bar after 4 days on stream under industrial HTS conditions ¹⁹.

Despite the consensus that aluminium doping results in enhanced thermal stability of the catalyst, no such agreement exists on the influence of aluminium on the reducibility of the fresh and activated catalyst. Meshkani and Rezaei ¹⁸ and Araújo and Rangel ²⁰ showed by H₂-TPR that the Fe₂O₃ → Fe₃O₄ transition is shifted to lower temperatures in the presence of aluminium. Thus, aluminium can enhance the reducibility of the Fe₂O₃. Nevertheless, these authors did not observe an influence of aluminium doping on the Fe₃O₄ → FeO and FeO → α-Fe transitions. Jeong et al. ²¹ observed a similar effect of aluminium doping. In their catalysts, the Fe₂O₃ → Fe₃O₄ transition shifted to lower temperatures, while the over-reduction peak of Fe₃O₄ was not distinct enough to interpret. In contrast, Natesakhawat et al. ¹⁷ showed that aluminium doping did not affect the Fe₂O₃ → Fe₃O₄ transition, while the Fe₃O₄ → FeO, α-Fe transition shifted to higher temperatures. The comparison of different TPR studies is likely complicated by the use of different heating rates, catalyst preparation methods, and different phases present in the catalyst precursors. We recently showed in two separate studies that the calcined catalyst precursor can contain a significant amount of small amorphous ferrihydrite (Fe₅HO₈ · 4 H₂O) particles, partially invisible to XRD analysis, in addition to hematite (α-Fe₂O₃), typically observed as the dominant phase by XRD ^{6,19}. The presence of ferrihydrite, which was shown by ⁵⁷Fe Mössbauer spectroscopy, likely complicates the interpretation of the TPR patterns because of overlapping reduction features with hematite ²². In H₂-TPR, over-reduction of magnetite leads to reduction features between 650 °C and 770 °C ^{17,18,21}, which is far above realistic industrial HTS conditions (typically in the range of 360-450 °C), although over-reduction during the WGS reaction also depends on the concentration of reducing and oxidising gasses ². When studying aluminium-doped iron oxides, the precipitation rate of iron and aluminium species relies heavily on the pH. Natesakhawat et al. ¹⁷ suggested that low pH favours iron precipitation while high pH favours aluminium precipitation. They showed that a catalyst prepared at pH = 9 provided the highest CO conversion in the preparation range pH = 8-11. The authors proposed that precipitated aluminium species start to dissolve at pH > 9 possibly due to the amphoteric nature of aluminium. This suggests that not all aluminium that is added for precipitation is incorporated into the catalyst structure when catalysts are aged at elevated pH and possibly a separate alumina phase is formed. While

alumina itself is not reducible, an impact on H₂-TPR data can be expected because aluminium can enter the iron oxide phases. This can explain the different outcomes of TPR measurements reported for aluminium-doped iron oxides.

Herein, we investigated the stability of aluminium- and chromium-doped magnetite with and without copper promoter under industrially relevant reaction conditions. The effect of dopants on the formation of FeO, α -Fe, and FeC_x was investigated with *in situ* Mössbauer spectroscopy. Mössbauer spectroscopy has been used extensively^{23,24} to study the formation of FeC_x phases in iron-based Fischer-Tropsch catalysts because of its high sensitivity for bulk iron species. In the present work, we exposed model HTS catalysts to increasingly reducing gas atmospheres by decreasing the steam partial pressure in a simulated HTS gas mixture containing H₂, CO, CO₂, He, and H₂O.

5.2 EXPERIMENTAL

5.2.1 CATALYST PREPARATION

Catalysts were prepared via a single-step co-precipitation/calcination route^{5,6,19}. In brief, appropriate amounts of iron, chromium, aluminium, and/or copper nitrates were dissolved in deionised water at 60 °C. The metals were precipitated by addition of a NaOH solution until the pH reached 10. The resulting slurry was aged for 1 hour at 60 °C after which the precipitates were washed with hot (60 °C) deionised water. After washing, the precipitates were dried at 150 °C for 3 hours and calcined at 400 °C for 4 hours in static air. Typical chromium and copper contents of commercial HTS catalysts are 8 wt% and 3 wt%, respectively. Accordingly, we prepared a chromium-doped iron oxide with a chromium content of 8.4 mol% (corresponding to 8 wt% chromium) and an aluminium-doped iron oxide with an aluminium content of 8.4 mol%. Both catalysts contained 3 wt% Cu. The calcined catalyst precursors are referred to as M-HM or MCu-HM, where M is the metal dopant and HM refers to hematite.

5.2.2 EXPERIMENTAL

In situ Mössbauer spectra were recorded on an in house made reactor cell. A detailed description of the *in situ* Mössbauer spectroscopy cell is provided elsewhere²⁵. Gas flows were controlled with mass flow controllers. Water was

added via a controlled evaporator mixer (Bronkhorst). In a typical experiment, the *in situ* Mössbauer spectroscopy cell was charged with 32.5 mg catalyst mixed with approximately 30 mg graphite. Experiments were performed at atmospheric pressure. After purging the cell in a He flow of 100 ml min⁻¹ at room temperature for 3 min, the samples were exposed to reaction conditions at 450 °C in a gas flow with a steam to gas ratio of 0.5, containing steam (added as liquid water at a rate of 2.22 g hour⁻¹), H₂ (55 ml min⁻¹), CO (14 ml min⁻¹), and CO₂ (6 ml min⁻¹), while the He flow was reduced to 25 ml min⁻¹. Starting from this composition, the steam concentration was lowered in steps of 3% until over-reduction was observed. After 1 hour at 450 °C, the temperature was lowered to 250 °C. At 250 °C, the H₂, CO, and CO₂ flows were replaced by He. After flushing for 3 min, water addition was stopped and the cell was allowed to cool to room temperature under a He flow. At room temperature, the gas inlet of the cell was closed and a Mössbauer spectrum was recorded overnight. Most of the contribution of iron dissolved in the beryllium windows of the *in situ* Mössbauer cell was removed in the presented spectra. In some of the spectra, small features of the beryllium window remain at ~0.00 mm s⁻¹.

XRD patterns were recorded on a PANalitical X'pert pro diffractometer using a Cu-K α source using a step size of 0.008°. Spectral fitting was performed using HighScore Plus software. Catalysts discharged from the HTS reactors were exposed to air before and during the XRD measurements.

5.3 RESULTS AND DISCUSSION

The detailed characterisation of the calcined catalyst precursors has been reported elsewhere^{5,6,19}. An overview of the phases present in the calcined catalyst precursors is given in Table 1. In brief, XRD patterns and Mössbauer spectra show that the non-doped HM and chromium-doped Cr-HM reference samples consist of hematite. The other samples, *i.e.*, CrCu-HM, Al-HM, and AlCu-HM, contain a mixture of hematite and ferrihydrite. While XRD suggest the exclusive presence of hematite crystallites in all samples, room-temperature Mössbauer spectra indicate the presence of a Fe³⁺ superparamagnetic (SPM) phase. By recording Mössbauer spectra at -269 °C, it was shown that this Fe³⁺ SPM phase consisted of a mixture of ferrihydrite and hematite. The CrCu-HM, Al-HM, and AlCu-HM catalysts contain mainly ferrihydrite with small contributions of hematite. On the contrary, the HM and Cr-HM reference catalysts only contain hematite.

Table 1. Phase identification of calcined catalysts (data taken from ¹⁹).

Sample	XRD	Mössbauer spectroscopy at room temperature	(%) ^a	Mössbauer spectroscopy at -269 °C	(%) ^a
HM	α -Fe ₂ O ₃	α -Fe ₂ O ₃	100	α -Fe ₂ O ₃	100
Cr-HM	α -Fe ₂ O ₃	α -Fe ₂ O ₃	100	α -Fe ₂ O ₃	100
CrCu-HM	α -Fe ₂ O ₃	Fe ³⁺ SPM	100	α -Fe ₂ O ₃ Fe ₅ HO ₈ · 4 H ₂ O	14 86
Al-HM	α -Fe ₂ O ₃	Fe ³⁺ SPM	100	α -Fe ₂ O ₃ Fe ₅ HO ₈ · 4 H ₂ O	17 83
AlCu-HM	*	Fe ³⁺ SPM	100	α -Fe ₂ O ₃ Fe ₅ HO ₈ · 4 H ₂ O	5 95

^a Spectral contribution

We used *in situ* Mössbauer spectra to study the activation of the calcined HM precursor in a simulated HTS feed mixture as a function of the steam concentration. Table S1 lists the volumetric compositions investigated and the corresponding ratios ($R = [\text{CO}][\text{H}_2]/[\text{CO}_2][\text{H}_2\text{O}]$) between the reducing gases H₂ and CO and the oxidising gases H₂O and CO₂ ². The variations in the H₂O concentration were balanced by changing the He concentration in order to keep the CO, CO₂ and H₂ concentrations constant. The gas composition with the highest steam concentration of 27% (*i.e.*, the lowest R of 1.48) is close to that of a commercial HTS feed with a steam to gas ratio of 0.5 (33% steam) ⁴. Starting from this composition, the steam concentration was lowered in steps of 3% until over-reduction was observed.

Figure 1 shows the *in situ* Mössbauer spectra of the used HM catalyst as well as the reference *ex situ* Mössbauer spectrum of the calcined precursor of HM. Exposure of the calcined HM catalyst to industrial HTS conditions with $R = 1.48$ results in the disappearance of the magnetically split sextet characteristic of hematite and the emergence of two new sextets related to the tetrahedral and octahedral Fe sites of magnetite (Table S2). No other Fe phases than magnetite were observed under these conditions. Increasing R to 1.64 and 1.84 (more reducing conditions) gave similar results. The onset of over-reduction was observed at $R = 2.09$ with the appearance of two more magnetically split sextets. The Mössbauer parameters of these sextets indicate the formation of α -Fe and Fe₃C (cementite) phases. At $R = 2.42$, reduction is substantial and the contribution of cementite is much larger than that of metallic Fe, indicating

rapid carburisation of the latter. These samples did not contain wüstite (FeO), which is normally observed as an intermediate in the reduction of magnetite to metallic Fe during TPR experiments²¹. These results show that α -Fe and likely FeO are short-lived intermediates during the over-reduction of the active phase in HTS conditions to Fe-carbides under practical HTS conditions. These Fe-carbides are a major cause of deactivation associated with over-reduction^{1,9}. XRD patterns of the catalysts used in the *in situ* Mössbauer experiments are shown in Figure S1. Consistent with the Mössbauer data, HM treated at $R = 1.48$ only contains magnetite. The same holds for the samples treated in the R -range of 1.64 – 2.42. However, different from the Mössbauer findings, the catalysts exposed to $R = 2.09$ and 2.42 did not contain XRD evidence for the presence of cementite. A likely explanation is that the cementite phase is present as very small particles.

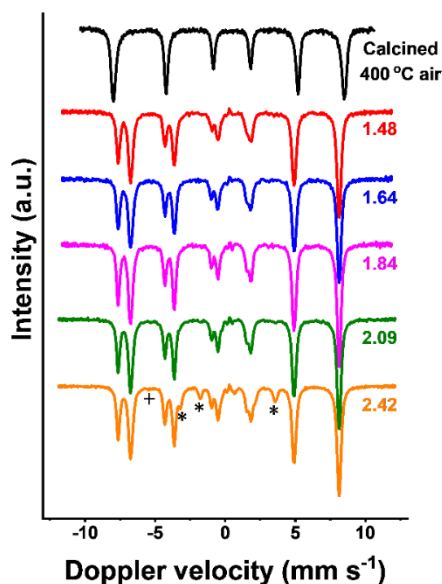


Figure 1. *In situ* Mössbauer spectra of HM catalyst as a function of H₂O content. The spectra are dominated by two sextets of magnetite. Peaks of the cementite sextet are indicated with an (*), peaks of α -Fe with a (+).

The corresponding Mössbauer spectra for Cr-HM are collected in Figure 2. Similar to the non-doped HM catalyst, the hematite phase in the calcined chromium-doped catalyst precursor is completely converted into magnetite upon exposure to HTS conditions of $R = 1.48$ (Table S3). Different from the HM catalyst, exposing Cr-HM to a feed with $R = 2.42$ does not lead to the formation of cementite. Thus, chromium doping rendered the active magnetite phase more stable against over-reduction under industrially relevant HTS conditions. For this Cr-HM catalyst, α -Fe and FeC_3 phases were only observed at $R = 6.57$. These data show that chromium-doped magnetite is more stable against over-reduction, which is in line with literature¹⁵. The corresponding XRD patterns of the used Cr-HM catalysts confirm these findings (Fig. S2). However, in this case the cementite phase obtained at $R = 6.57$ was also observed by XRD, which is likely due to the much larger amount of this phase.

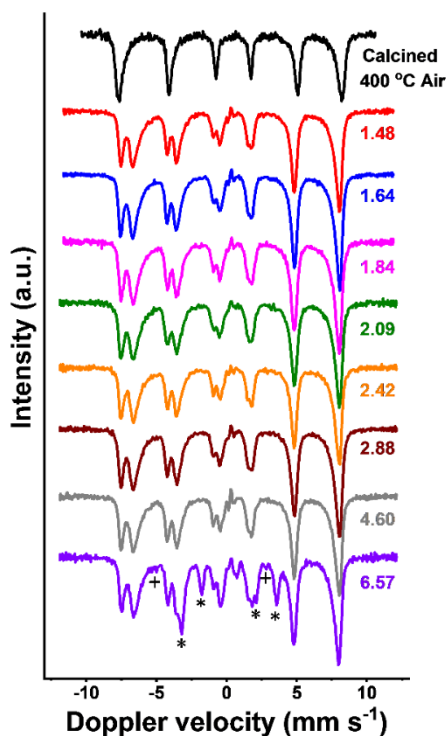


Figure 2. *In situ* Mössbauer spectra of Cr-HM catalyst compared to *ex situ* spectrum of calcined catalyst. Visible peaks of the cementite sextet are indicated with an asterisk (*), those of α -Fe with a plus (+).

The *in situ* Mössbauer spectra of the CrCu-HM catalyst are shown in Figure 3. The reference spectrum of the calcined precursor contains a SPM doublet. Analysis of this SPM phase by Mössbauer spectroscopy at -269 °C confirmed that this sample contains both hematite and ferrihydrite (Table 1). After exposure of the calcined CrCu-HM catalyst to HTS conditions with $R = 1.48$, the SPM doublet disappeared and two magnetically split sextets emerged, indicating the formation of magnetite (Table S4). At $R = 2.88$, an additional small sextet appeared, indicating the formation of cementite. The fraction of cementite remained constant until $R = 6.57$, where the contribution of the cementite phase had grown much larger. Thus, the presence of copper leads to a slightly earlier onset of over-reduction in terms of R value compared to Cr-HM. Nevertheless, the amount of over-reduced phases remains small, while the amount of cementite under the most reducing conditions for CrCu-HM was similar to that for Cr-HM. XRD patterns of the used CrCu-HM catalysts are shown in (Fig. S3). The diffraction pattern observed after exposure of the calcined catalyst to HTS conditions of $R = 1.48$ points to magnetite. No reflections due to phases obtained by over-reduction were observed between $R = 1.48$ - 2.42 , in line with the *in situ* Mössbauer results. The discharged catalyst treated at $R = 2.88$ shows a small feature at $2\theta = \sim 45^\circ$ in its XRD pattern, confirming the formation of a small amount of cementite in line with the *in situ* Mössbauer spectra (Fig. 3). This cementite feature was not observed for the discharged catalyst treated at $R = 4.60$, whereas it was visible in the XRD pattern of the catalyst treated at $R = 6.57$. The absence of cementite reflections in the used catalyst after exposure to HTS conditions with $R = 4.60$ again shows the utility of Mössbauer spectroscopy when studying bulk iron species.

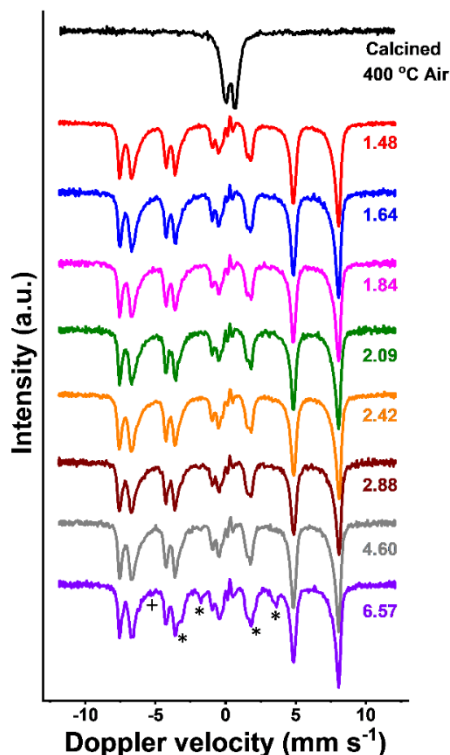


Figure 3. *In situ* Mössbauer spectra of CrCu-HM catalyst compared to *ex situ* spectrum of calcined catalyst. Visible peaks of the cementite sextet are indicated with an asterisk (*), those of α -Fe with a plus (+).

Exposure of the calcined Al-HM catalyst to HTS conditions of $R = 1.48$ resulted in the formation of the active magnetite phase similar to the HM, Cr-HM, and CrCu-HM catalysts (Fig. 4). Upon exposure of the calcined catalyst to a gas mixture of $R = 1.64$, a third sextet was observed which was attributed to α -Fe (Table S5), indicating over-reduction of the active magnetite phase. When the catalyst was subsequently exposed to more reducing conditions, the α -Fe phase was observed until a cementite phase formed at $R = 2.09$. This shows that the presence of aluminium in these catalysts enhances over-reduction of the active phase to α -Fe, while it initially prevents carburisation. The stabilisation of the α -Fe phase against carburisation was not observed in the non-doped and chromium-doped catalysts. This could indicate that the α -Fe interacts with an amorphous Al_2O_3 phase invisible to XRD analysis, whose presence was hypothesised above. Despite the possible presence of a separate amorphous Al_2O_3 phase, and the enhanced over-reduction caused by the

aluminium doping, the aluminium-doped catalyst was stable from over-reduction at a steam concentration of 27% ($R = 1.48$), which is substantially lower than normal operating conditions where a steam concentration of 33% is used⁴. This underpins the potential of aluminium to replace chromium as a dopant in Fe-based WGS catalysts¹⁹. The possible presence of a separate amorphous Al_2O_3 phase suggests that further optimisation of the preparation procedure should be explored to obtain an optimal ageing pH for both aluminium and iron oxides. Natesakhawat et al. showed that the pH during precipitation had a large influence on the CO conversion of the catalysts. They suggested that this is the result of low pH values in the preparation, which would favour Fe precipitation, whereas at high pH values precipitation of Al species is faster. Although the authors mention that precipitated aluminium species can dissolve in water at $\text{pH} > 9$, it is also mentioned that in other works an optimum pH of 11 has been reported. XRD patterns of the used Al-HM catalysts (Fig. S4) confirm the formation of magnetite upon exposure of the calcined catalyst to HTS conditions at $R = 1.48$. No reflections belonging to α -Fe were observed $R = 1.64$ - 2.09 , in contrast to the *in situ* Mössbauer spectra where α -Fe formation was observed from an R factor of 1.64 and below. Since these patterns were recorded after the catalysts were exposed to air, α -Fe observed in Mössbauer spectra is likely oxidised. This shows the benefit of using *in situ* Mössbauer spectroscopy. No evidence of a separate aluminium oxide phase was found, this is consistent with the presence of an amorphous aluminium oxide phase.

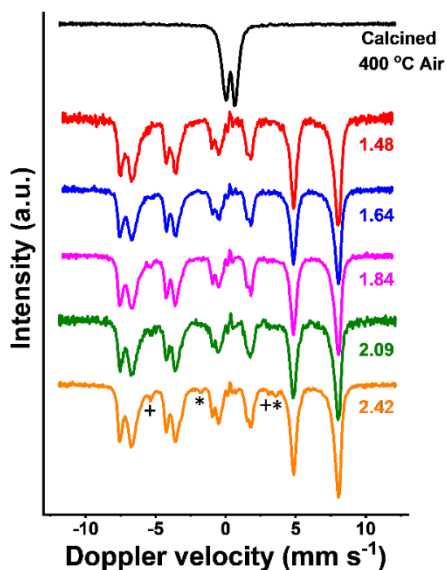


Figure 4. *In situ* Mössbauer spectra of Al-HM catalyst compared to *ex situ* spectrum of calcined catalyst. Visible peaks of the cementite sextet are indicated with an (*), those of α -Fe with a (+).

In situ Mössbauer spectra of AlCu-HM catalysts (Fig. 5, Table S6) show α -Fe and a cementite formation at $R = 2.09$. This is similar to the non-doped HM catalyst which suggests that there is no effect of these dopants on over-reduction of the catalyst. It should be mentioned that $R = 2.09$ is far below normal operating conditions of 33% steam typically employed in an industrial plant. This means that the AlCu-HM catalyst is a viable candidate to replace chromium. It is interesting to note that the effect of aluminium/copper co-doping is opposite to that of chromium/copper co-doping, where a slight enhancement of over-reduction was found. The stabilisation of α -Fe, observed in the aluminium-doped catalyst, was not observed in the aluminium/copper co-doped catalyst. Since the preparation procedure for the aluminium-doped catalysts was not optimised in our study, we cannot exclude the presence of a separate amorphous Al_2O_3 phase. Based on these results, further optimisation of the aluminium precipitation procedure should be explored. XRD patterns of used AlCu-HM catalysts confirm the formation of the active magnetite catalysts at $R = 1.48$ (Fig. S5). In contrast to the *in situ* Mössbauer spectra, no reflections due to cementite were observed in the sample treated at $R = 2.42$, suggesting that, if present, it is in the form of very small particles.

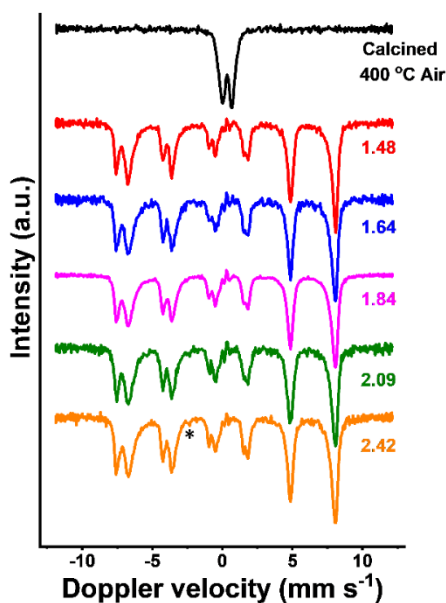


Figure 5. *In situ* Mössbauer spectra of AlCu-HM catalyst compared to *ex situ* spectrum of calcined catalyst. Visible peaks of the cementite sextet are indicated with an (*), those of α -Fe with a (+).

5.4 CONCLUSIONS

The influence of chromium and aluminium doping, together with copper co-doping of iron oxide based HTS catalysts, was investigated for the first time with *in situ* Mössbauer spectroscopy (Table 2). *In situ* Mössbauer spectra showed that in a non-doped iron-oxide catalyst α -Fe and cementite formation occurred after treatment under HTS conditions at an R factor of 2.09. Chromium doping stabilised the active magnetite phase down to $R = 4.60$ before α -Fe and cementite formation occurred, confirming the well known stabilising effect of chromium on these structures during HTS operation. The chromium copper co-doped catalyst slightly enhanced over-reduction of the active magnetite phase to an R factor of 2.88. The aluminium-doped catalysts showed α -Fe formation at $R = 1.64$. Cementite formation was observed at $R = 2.09$ for the aluminium-doped catalyst, which shows that the α -Fe is stabilised from carburisation in aluminium-doped catalysts. In the aluminium/copper co-doped catalyst, cementite formation was observed at $R = 2.09$, which is the same as a non-doped catalyst. Despite the enhanced over-reduction in the aluminium-doped catalyst, compared to the chromium-doped catalyst, no over-reduction was observed at $R = 1.48$, which is already significantly lower

than normal operating conditions of 33% H₂O. This shows that aluminium-doped catalysts are initially stable under industrially relevant HTS conditions. Further research is required to optimise the incorporation of the promising aluminium dopant into the structure of the freshly calcined catalyst and in the activated magnetite catalyst.

Table 2. Overview of phases observed *in situ* Mössbauer spectra.

	1.48	1.64	1.84	2.09	2.42	2.88	4.60	6.57
HM	●	●	●	●■◆	●◆	-	-	-
Cr-HM	●	●	●	●	●	●	●	●■◆
CrCu-HM	●	●	●	●	●	●■◆	●■◆	●◆
Al-HM	●	●	●■	●■◆	●■◆	-	-	-
AlCu-HM	●	●	●	●◆	●■◆	-	-	-

^a Phases are indicated as: Magnetite (●), α -Fe (■), Fe₃C (◆).

REFERENCES

- [1] M. Zhu; I.E. Wachs Iron-Based Catalysts for the High-Temperature Water-Gas Shift (HT-WGS) Reaction: A Review. *ACS catalysis* **2016**, *6*, 722-732.
- [2] D.W. Lee; M.S. Lee; J.Y. Lee; S. Kim; H.J. Eom; D.J. Moon; K.Y. Lee The review of Cr-free Fe-based catalysts for high-temperature water-gas shift reactions. *Catalysis Today* **2013**, *210*, 2-9.
- [3] D.S. Newsome The Water-Gas Shift Reaction. *Catalysis Reviews Science and Engineering* **1980**, *21*, 275-318.
- [4] M.V. Twigg *Catalyst handbook*; 2 ed.; 1989.
- [5] M.I. Ariëns; V. Chlan; P. Novák; L.G.A. van de Water; A.I. Dugulan; E. Brück; E.J.M Hensen The role of chromium in iron-based high-temperature water-gas shift catalysts under industrial conditions. *Applied Catalysis B: Environmental* **2021**, *297*, 120465.
- [6] M.I. Ariëns; L.G.A. van de Water; A.I. Dugulan; E. Brück; E.J.M Hensen Copper promotion of chromium-doped iron oxide water-gas shift catalysts under industrially relevant conditions. *Journal of Catalysis* **2021**, *405*, 391-403.
- [7] C.J. Keturakis; M. Zhu; E.K. Gibson; M. Daturi; F. Tao; A.I. Frenkel; I.E. Wachs Dynamics of CrO₃-Fe₂O₃ Catalysts during the High-Temperature Water-Gas Shift Reaction: Molecular Structures and Reactivity. *ACS catalysis* **2016**, *6*, 4786-4798.
- [8] M. Zhu; T.C.R. Rocha; T. Lunkenbein; A. Knop-Gericke; R. Schlögl; I.E. Wachs Promotion Mechanisms of Iron Oxide-Based High Temperature Water-Gas Shift Catalysts by Chromium and Copper. *ACS catalysis* **2016**, *6*, 4455-4464.
- [9] C. Rhodes; G.J. Hutchings; A.M. Ward Water-gas shift reaction: finding the mechanistic boundary. *Catalysis Today* **1995**, *23*, 43-58.
- [10] M. Zhu; P. Tian; J. Chen; M.E. Ford; J. Xu; I.E. Wachs; Y.F. Han Activation and deactivation of the commercial-type CuO-Cr₂O₃-Fe₂O₃ high temperature shift catalyst. *American Institute of Chemical Engineers* **2019**, *66*, 1-6.
- [11] M. Zhu; P. Tian; R. Kurtz; T. Lunkenbein; J. Xu; R. Schlögl; I.E. Wachs; Y.F. Han Strong Metal-Support Interactions between Copper and Iron Oxide during the High-Temperature Water-Gas Shift Reaction. *Angewandte chemie* **2019**, *131*, 9181-9185.

- [12] C. Pellerin; S.M. Booker Reflections on hexavalent chromium: health hazards of an industrial heavyweight. *Environmental Health Perspectives* **2000**, *108*, 402-407.
- [13] M. Zhu; Ö. Yalçın; I.E. Wachs Revealing structure-activity relationships in chromium free high temperature shift catalysts promoted by earth abundant elements. *Applied Catalysis B: Environmental* **2018**, *232*, 205-212.
- [14] G.K. Reddy; K. Gunasekara; P. Boolchand; P.G. Smirniotis Cr- and Ce-Doped Ferrite Catalysts for the High Temperature Water-Gas Shift Reaction: TPR and Mössbauer Spectroscopic Study. *Journal of Physical Chemistry C* **2011**, *115*, 920-930.
- [15] D. Damma; D. Jampaiah; A. Welton; P. Boolchand; A. Arvanitis; J. Dong; P.G. Smirniotis Effect of Nb modification on the structural and catalytic property of Fe/Nb/M (M = Mn, Co, Ni, and Cu) catalyst for high temperature water-gas shift reaction. *Catalysis Today* **2019**, *355*, 921-931.
- [16] M. Zhu; I.E. Wachs A perspective on chromium-free iron oxide-based catalysts for high temperature water-gas shift reaction. *Catalysis Today* **2018**, *311*, 2-7.
- [17] S. Natesakhawat; X. Wang; L. Zhang; U.S. Ozkan Development of chromium-free iron-based catalysts for high-temperature water-gas shift reaction. *Journal of Molecular Catalysis A: Chemical* **2006**, *260*, 82-94.
- [18] F. Meshkani; M. Rezaei Preparation of nanocrystalline metal (Cr, Al, Mn, Ce, Ni, Co and Cu) modified ferrite catalysts for the high temperature water gas shift reaction. *Renewable Energy* **2015**, *74*, 588-589.
- [19] M.I. Ariëns; L.G.A. van de Water; A.I. Dugulan; E. Brück; E.J.M Hensen Substituting Chromium in Iron-Based Catalysts for the High-Temperature Water-Gas Shift Reaction. *ACS catalysis* **2022**.
- [20] G. Carneiro de Araújo; M. do Carmo Rangel An environmental friendly dopant for the high-temperature shift catalysts. *Catalysis Today* **2000**, *62*, 201-207.
- [21] D.W. Jeong; V. Subramanian; J.O. Shim; W.J. Jang; Y.C. Seo; H.S. Roh; J.H. Gu; Y.T. Lim High-Temperature Water Gas Shift Reaction Over Fe/Al/Cu Oxide Based Catalysts Using Simulated Waste-Derived Synthesis Gas. *Catalysis Letters* **2013**, *143*, 438-444.
- [22] W.K. Jozwiak; E. Kaczmarek; T.P. Maniecki; W. Ignaczak; W. Maniukiewicz Reduction behavior of iron oxides in hydrogen and

- carbon monoxide atmospheres. *Applied Catalysis A: General* **2007**, *326*, 17-27.
- [23] V.P. Santos; T.A. Wezendonk; J.J. Delgado Jaén; A.I. Dugulan; M.A. Nasalevich; H.U. Islam; A. Chojecki; S. Sartipi; X. Sun; A.A. Hakeem; A.C.J. Koeken; M. Ruitenbeek; T. Davidian; G.R. Meima; G. Sankar; F. Kapteijn; M. Makkee; J. Gascon Metal organic framework-mediated synthesis of highly active and stable Fischer-Tropsch catalysts. *Nature Communications* **2015**, *6*, 6451.
- [24] J. Xie; H.M. Torres Galvis; A.C.J. Koeken; A. Kirilin; A.I. Dugulan; M. Ruitenbeek; K.P. de Jong Size and Promoter Effects on Stability of Carbon-Nanofiber-Supported Iron-Based Fischer-Tropsch Catalysts. *ACS catalysis* **2016**, *6*, 4017-4024.
- [25] T.A. Wezendonk; V.P. Santos; M.A. Nasalevich; Q.S.E. Warringa; A.I. Dugulan; A. Chojecki; A.C.J. Koeken; M. Ruitenbeek; G. Meima; H.U. Islam; G. Sankar; M. Makkee; F. Kapteijn; J. Gascon Elucidating the Nature of Fe Species during Pyrolysis of the Fe-BTC MOF into Highly Active and Stable Fischer-Tropsch Catalysts. *ACS catalysis* **2016**, *6*, 3236-3247.

SUPPORTING INFO

Table S1. Gas flows^a per H₂O percentage.

	27 %	24 %	21 %	18 %	15 %	12 %	9 %	6 %
H ₂ O ^b	40.5	36	31.5	27	22.5	18	13.5	9
He	34.5	39	43.5	48	52.5	57	61.5	66
H ₂	55	55	55	55	55	55	55	55
CO	14	14	14	14	14	14	14	14
CO ₂	6	6	6	6	6	6	6	6
Total	150	150	150	150	150	150	150	150
R ^c	1.48	1.64	1.84	2.09	2.42	2.88	4.60	6.57

^a Gasflows in (ml min⁻¹).

^b Calculated with the ideal gas law.

^c $R = (H_2 + CO)/(CO_2 + H_2O)$

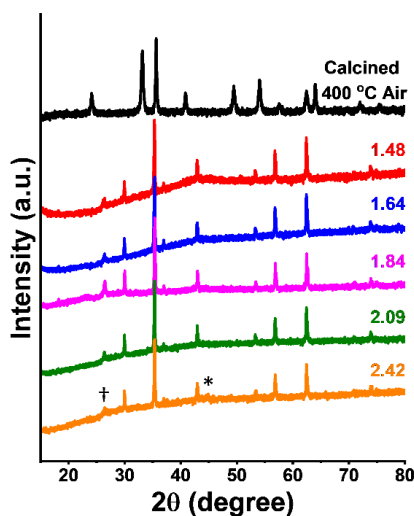


Figure S1. *Ex situ* XRD patterns of HM catalyst recorded before (calcined) and after *in situ* Mössbauer measurements. The position of the main cementite reflection is marked with an asterisk (*), the reflection of residual graphite is indicated with a dagger (†).

Table S2. Fitting parameters of *in situ* Mössbauer spectra HM catalyst.

R	Phase	IS (mm s ⁻¹)	QS (mm s ⁻¹)	Hyperfine field (T)	Linewidth (mm s ⁻¹)	Spectral contribution (%)
1.48	Fe ₃ O ₄ (tet)	0.27	-0.01	49.1	0.29	35
	Fe ₃ O ₄ (oct)	0.67	0.01	45.8	0.26	65
1.64	Fe ₃ O ₄ (tet)	0.27	-0.01	49.1	0.28	35
	Fe ₃ O ₄ (oct)	0.67	0.02	45.9	0.25	65
1.84	Fe ₃ O ₄ (tet)	0.27	-0.01	49.1	0.26	36
	Fe ₃ O ₄ (oct)	0.67	0.01	45.9	0.23	64
2.09	Fe ₃ O ₄ (tet)	0.27	0.00	49.1	0.27	35
	Fe ₃ O ₄ (oct)	0.67	0.01	45.8	0.24	62
	α-Fe	0.00	0.00	32.1	0.5	1
	Fe ₃ C	0.18	0.00	21.0	0.5	2
2.42	Fe ₃ O ₄ (tet)	0.27	0.00	49.1	0.27	32
	Fe ₃ O ₄ (oct)	0.67	0.01	45.9	0.25	56
	Fe ₃ C	0.18	0.02	21.0	0.34	12

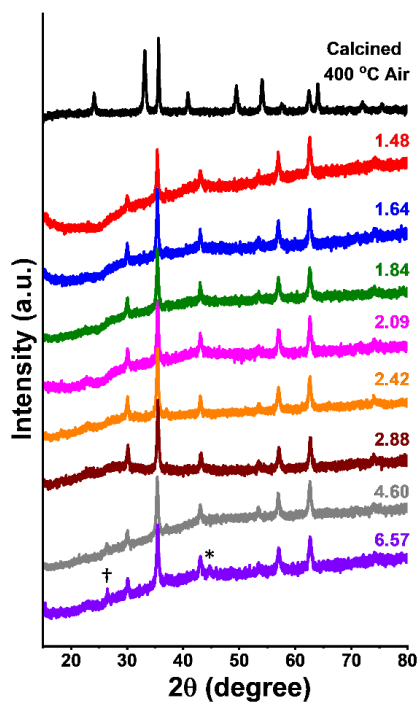


Figure S2. *Ex situ* XRD patterns of Cr-HM catalyst recorded before (calcined) and after *in situ* Mössbauer measurements. The position of the main cementite reflection is marked with an asterisk (*), the reflection of residual graphite is indicated with a dagger (†).

Table S3. Fitting parameters of *in situ* Mössbauer spectra obtained after exposure of Cr-HM catalyst to gas mixtures of increased reducibility.

R	Phase	IS (mm s ⁻¹)	QS (mm s ⁻¹)	Hyperfine field (T)	Linewidth (mm s ⁻¹)	Spectral contribution (%)
1.48	Fe ₃ O ₄ (tet)	0.28	0.00	48.5	0.35	34
	Fe ₃ O ₄ (oct)	0.64	-0.03	44.0	0.37	66
1.64	Fe ₃ O ₄ (tet)	0.28	-0.01	48.6	0.34	33
	Fe ₃ O ₄ (oct)	0.64	-0.03	44.1	0.37	67
1.84	Fe ₃ O ₄ (tet)	0.28	0.00	48.4	0.37	33
	Fe ₃ O ₄ (oct)	0.65	-0.03	43.8	0.36	67
2.09	Fe ₃ O ₄ (tet)	0.28	-0.01	48.4	0.40	35
	Fe ₃ O ₄ (oct)	0.65	-0.02	44.1	0.38	65
2.42	Fe ₃ O ₄ (tet)	0.28	-0.01	48.4	0.35	34
	Fe ₃ O ₄ (oct)	0.64	-0.03	43.9	0.35	66
2.88	Fe ₃ O ₄ (tet)	0.28	-0.01	48.5	0.37	33
	Fe ₃ O ₄ (oct)	0.65	-0.03	44.0	0.38	67
4.60	Fe ₃ O ₄ (tet)	0.29	-0.01	48.4	0.34	33
	Fe ₃ O ₄ (oct)	0.65	-0.04	44.0	0.36	67
6.57	Fe ₃ O ₄ (tet)	0.28	-0.01	48.1	0.36	26
	Fe ₃ O ₄ (oct)	0.65	-0.02	43.7	0.34	52
	α-Fe	0.00	0.00	33.0	0.50	1
	Fe ₃ C	0.19	0.02	20.9	0.36	21

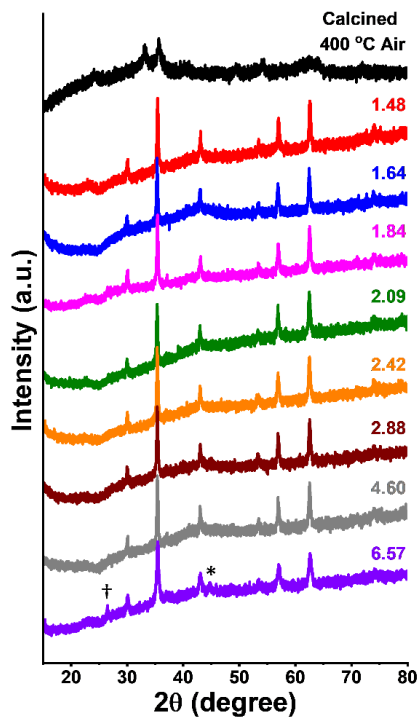


Figure S3. *Ex situ* XRD patterns of CrCu-HM catalyst recorded before (calcined) and after *in situ* Mössbauer measurements. The position of the main cementite reflection is marked with an asterisk (*), the reflection of residual graphite is indicated with a dagger (†).

Table S4. Fitting parameters of *in situ* Mössbauer spectra obtained after exposure of CrCu-HM catalyst to gas mixtures of increased reducibility.

R	Phase	IS (mm s ⁻¹)	QS (mm s ⁻¹)	Hyperfine field (T)	Linewidth (mm s ⁻¹)	Spectral contribution (%)
1.48	Fe ₃ O ₄ (tet)	0.28	-0.01	48.5	0.29	32
	Fe ₃ O ₄ (oct)	0.64	-0.03	44.2	0.36	68
1.64	Fe ₃ O ₄ (tet)	0.28	-0.01	48.5	0.31	33
	Fe ₃ O ₄ (oct)	0.65	-0.02	44.0	0.32	67
1.84	Fe ₃ O ₄ (tet)	0.28	0.00	48.5	0.3	33
	Fe ₃ O ₄ (oct)	0.64	-0.03	44.1	0.34	67
2.09	Fe ₃ O ₄ (tet)	0.28	-0.01	48.5	0.29	32
	Fe ₃ O ₄ (oct)	0.65	-0.03	44.0	0.34	68
2.42	Fe ₃ O ₄ (tet)	0.28	-0.01	48.7	0.32	33
	Fe ₃ O ₄ (oct)	0.65	-0.03	44.2	0.35	67
2.88	Fe ₃ O ₄ (tet)	0.28	-0.01	48.7	0.32	33
	Fe ₃ O ₄ (oct)	0.64	-0.03	44.2	0.32	63
	α-Fe	0.00	0.00	33.0	0.5	1
	Fe ₃ C	0.18	21	0.01	0.5	3
4.60	Fe ₃ O ₄ (tet)	0.29	0.00	48.5	0.32	33
	Fe ₃ O ₄ (oct)	0.64	-0.03	44.0	0.32	62
	α-Fe	0.00	0.00	33.0	0.5	1
	Fe ₃ C	0.17	0.09	20.4	0.5	4
6.57	Fe ₃ O ₄ (tet)	0.28	-0.01	48.5	0.3	28
	Fe ₃ O ₄ (oct)	0.65	-0.03	44.1	0.31	57
	Fe ₃ C	0.20	0.04	22.6	0.5	15

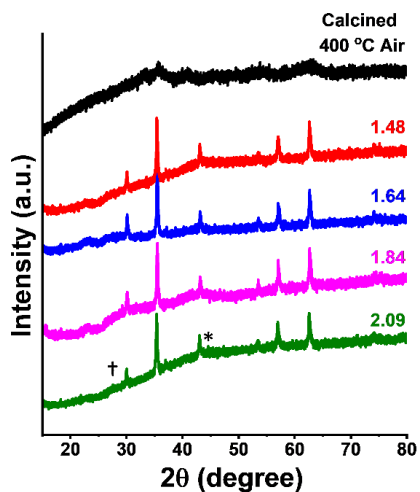


Figure S4. *Ex situ* XRD patterns of Al-HM catalyst recorded before (calcined) and after *in situ* Mössbauer measurements. The position of the main cementite reflection is marked with an asterisk (*), the reflection of residual graphite is indicated with a dagger (†).

Table S5. Fitting parameters of *in situ* Mössbauer spectra obtained after exposure of Al-HM catalyst to gas mixtures of increased reducibility.

R	Phase	IS (mm s ⁻¹)	QS (mm s ⁻¹)	Hyperfine field (T)	Linewidth (mm s ⁻¹)	Spectral contribution (%)
1.48	Fe ₃ O ₄ (tet)	0.29	-0.01	48.4	0.37	33
	Fe ₃ O ₄ (oct)	0.65	-0.03	44.5	0.35	67
1.64	Fe ₃ O ₄ (tet)	0.28	-0.02	48.4	0.37	36
	Fe ₃ O ₄ (oct)	0.65	-0.02	44.6	0.35	64
1.84	Fe ₃ O ₄ (tet)	0.28	-0.01	48.4	0.36	34
	Fe ₃ O ₄ (oct)	0.64	-0.03	44.7	0.33	62
	α-Fe	0.00	0.00	33.3	0.5	4
2.09	Fe ₃ O ₄ (tet)	0.28	-0.02	48.4	0.37	32
	Fe ₃ O ₄ (oct)	0.65	-0.02	44.7	0.35	61
	α-Fe	0.00	0.00	33.0	0.5	4
	Fe ₃ C	0.17	0.02	20.6	0.5	3
2.42	Fe ₃ O ₄ (tet)	0.28	-0.01	48.5	0.35	31
	Fe ₃ O ₄ (oct)	0.64	-0.03	44.7	0.34	59
	α-Fe	0.00	0.00	33.0	0.5	4
	Fe ₃ C	0.17	0.04	20.9	0.5	6

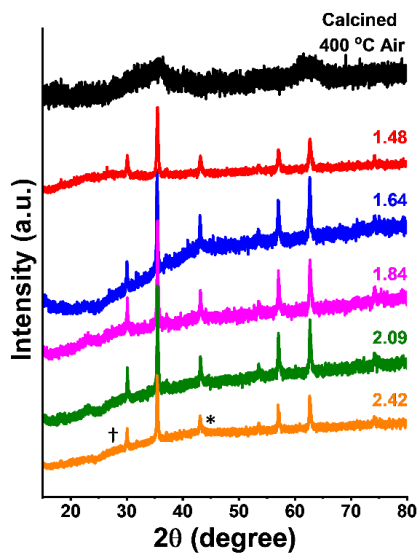


Figure S5. *Ex situ* XRD patterns of AlCu-HM catalyst recorded before (calcined) and after *in situ* Mössbauer measurements. The position of the main cementite reflection is marked with an asterisk (*), the reflection of residual graphite is indicated with a dagger (†).

Table S6. Fitting parameters of *in situ* Mössbauer spectra obtained after exposure of AlCu-HM catalyst to gas mixtures of increased reducibility.

R	Phase	IS (mm s ⁻¹)	QS (mm s ⁻¹)	Hyperfine field (T)	Linewidth (mm s ⁻¹)	Spectral contribution (%)
1.48	Fe ₃ O ₄ (tet)	0.28	-0.02	48.6	0.32	32
	Fe ₃ O ₄ (oct)	0.65	-0.02	44.8	0.32	68
1.64	Fe ₃ O ₄ (tet)	0.29	-0.03	48.5	0.35	34
	Fe ₃ O ₄ (oct)	0.65	-0.04	44.5	0.34	66
1.84	Fe ₃ O ₄ (tet)	0.29	-0.01	48.5	0.35	35
	Fe ₃ O ₄ (oct)	0.65	-0.03	44.7	0.33	65
2.09	Fe ₃ O ₄ (tet)	0.28	0.03	48.5	0.34	34
	Fe ₃ O ₄ (oct)	0.65	-0.03	44.7	0.33	64
	Fe ₃ C	0.18	0.09	20.5	0.50	2
2.42	Fe ₃ O ₄ (tet)	0.28	-0.01	48.5	0.34	33
	Fe ₃ O ₄ (oct)	0.65	-0.03	44.8	0.33	64
	α-Fe	0.00	0.00	33.0	0.50	1
	Fe ₃ C	0.18	0.00	21.0	0.50	2

6

SUMMARY & SAMENVATTING

SUMMARY AND OUTLOOK

Hydrogen gas is an essential reagent in numerous industrial processes including ammonia synthesis. Ammonia is a key intermediate in the synthesis of nitrogen-based fertilisers, e.g. nitrates and urea. According to recent estimates (2008), approximately half of the world population is fed by nitrogen-based fertilisers of synthetic origin. Therefore, statistically speaking, every other person reading this sentence owes their existence to ammonia synthesis. Nowadays, most hydrogen gas is produced from natural gas via steam reforming followed by a dual stage water-gas shift reaction. The catalyst used in high-temperature water-gas shift (HTS) is chromium/copper promoted iron oxide. Chromium is known to stabilise the active iron-oxide phase magnetite (Fe_3O_4) from sintering and over-reduction to α -Fe and Fe-carbides, while copper enhances the activity by providing additional active sites. The chromium stabiliser has been used for over a century, because it provides excellent stability and its low cost. Chromium is added to the catalyst precursor via a co-precipitation/calcination route. An unintended side effect of calcination is that some of the chromium can oxidise to chromium-6, which is

prone to strict handling and partial bans. The active magnetite phase has an inverse spinel structure composed of a 1:1:1 mixture of; tetrahedral Fe^{3+} , octahedral Fe^{3+} , and octahedral Fe^{2+} , resulting in an octahedral $\text{Fe}^{3+}/\text{Fe}^{2+}$ redox couple. The active sites of the bulk magnetite catalyst are the surface octahedral $\text{Fe}^{3+}/\text{Fe}^{2+}$ redox couple. Rational design of catalysts with alternative dopants to chromium is severely hindered because of a poor understanding of chromium incorporation into the inverse spinel magnetite structure. Accordingly, the position of chromium and its effect on the magnetite structure and the octahedral $\text{Fe}^{3+}/\text{Fe}^{2+}$ redox couple was investigated in detail.

In **chapter 2**, a suite of chromium-doped iron-oxide catalysts was prepared via a co-precipitation/calcination route. The freshly calcined catalysts consisted of chromium doped hematite ($\alpha\text{-Fe}_{2-x}\text{Cr}_x\text{O}_3$). The reduction of the hematite precursor, and over-reduction of the active magnetite catalyst to $\alpha\text{-Fe}$ occur at higher temperatures in chromium-doped catalysts. Chromium incorporated into the magnetite structure after exposure of calcined catalysts to industrially relevant water-gas shift conditions. The presence of chromium resulted in higher CO conversion, irrespective of the reaction pressure (2 or 25 bar). XRD analysis showed that chromium doping resulted in smaller crystallite sizes, confirming its role as a structural promoter. Mössbauer spectra showed that chromium incorporates in octahedral sites of magnetite. The incorporation of chromium prevented the reduction of Fe^{3+} ions during magnetite formation, resulting in a higher $\text{Fe}^{3+}/\text{Fe}^{2+}$ ratio in the inverse spinel structure. These variations in the $\text{Fe}^{3+}/\text{Fe}^{2+}$ ratio compared to bulk magnetite had no measurable effect on the high CO conversion typically associated with chromium-doping. The interpretation of Mössbauer data was supported by DFT calculation of hyperfine parameters of various chromium and Fe-vacancy doped magnetite structures. These results show that the active magnetite phase under industrially relevant water-gas shift conditions is best described by $\text{Fe}_{3-x(1-\delta)}\text{Cr}_x\text{O}_4$ structure. In the $\text{Fe}_{3-x(1-\delta)}\text{Cr}_x\text{O}_4$ structure, Cr^{3+} is incorporated in the octahedral sites where its presence during the formation of the active phase by partial reduction of $\alpha\text{-Fe}_{2-x}\text{Cr}_x\text{O}_3$ hinders Fe^{2+} formation. The $\text{Fe}_{3-x(1-\delta)}\text{Cr}_x\text{O}_4$ structure is partially oxidised compared to stoichiometric magnetite where the octahedral $\text{Fe}^{3+}/\text{Fe}^{2+}$ ratio is unity. With the exact position of chromium in the magnetite structure now understood, the position of copper was investigated, because it is a typical promoter used in HTS catalysts.

In **chapter 3**, a suite of chromium/copper co-doped catalysts was prepared via a co-precipitation/calcination route and investigated to gain understanding

into the position of copper on the used $\text{Fe}_{3-x(1-\delta)}\text{Cr}_x\text{O}_4$ bulk catalyst. In contrast to calcined chromium-doped iron-oxide catalysts, which consisted of a hematite phase, chromium/copper co-doped catalysts consist of a mixture of hematite and ferrihydrite. It was shown by Mössbauer spectroscopy that copper inhibits the formation of hematite during calcination as the amount of ferrihydrite increased with the copper content. The hematite and ferrihydrite precursors convert completely to magnetite under industrially relevant water-gas shift conditions at 2 and 25 bar. Mössbauer spectra confirmed the results of chapter 2 that chromium forms a solid solution with magnetite, resulting in a partially oxidised structure ($\text{Fe}_{3-x(1-\delta)}\text{Cr}_x\text{O}_4$). The addition of copper showed no significant effect on the hyperfine parameters in Mössbauer spectra, indicating that it is not likely that copper is incorporated in the bulk magnetite structure. NAP-XPS experiments showed copper exists as metallic copper at the catalyst surface under water-gas shift conditions. *Ex situ* XPS experiments of catalysts exposed to industrially relevant water-gas conditions showed that a catalyst exposed to 25 bar had a more ferrous like surface than catalysts treated at 2 bar due to the more reducing nature of the gas mixture at elevated pressure. No effect of the reaction pressure on the bulk structure was observed. In chromium/copper co-doped catalysts, chromium stabilises the high surface area of the catalyst irrespective of pressure, leading to a higher CO conversion. Copper doping results in increased CO conversion at ambient and industrially relevant pressure via the formation of new active surface sites.

With a good understanding of the chromium and copper dopants, a suite of catalysts with alternative dopants was investigated in **chapter 4**. M-doped and M/Cu-doped (M = Fe, Cr, Al, Ga, In, Mn, Zn, Nb) catalysts were prepared to investigate the effect of alternative dopants on the active magnetite catalyst. The catalysts were prepared via a co-precipitation/calcination route and investigated by Mössbauer spectroscopy. Aluminium, gallium, and indium were chosen to investigate the effect of (trivalent) dopant size while manganese, zinc, and niobium were chosen to investigate the effect of different oxidation states. Similar to the non-doped and chromium-doped precursors investigated in chapter 2, gallium yielded hematite as the main phase after calcination. Calcined catalysts doped with aluminium, indium, manganese, zinc, and niobium contained a mixture of hematite and ferrihydrite, the latter in the form of relatively small crystallites. All copper-doped catalysts contained mainly ferrihydrite. Activity testing under industrially relevant water-gas shift conditions for 4 days at 25 bar showed that aluminium is the

most suitable substituent for chromium in terms of CO conversion. Comparing the CO conversion of M/Cu-doped catalysts, it was shown that aluminium doping provides very similar catalytic performance to chromium doping. The other dopants result in a significantly lower CO conversion after prolonged testing, decreasing in the order gallium > indium > manganese > zinc > niobium. Mössbauer spectroscopy showed that aluminium was incorporated in both tetrahedral and octahedral sites of magnetite. This is in contrast to chromium, which was shown in chapter 2 to exclusively substitute octahedral iron. Additionally, aluminium doping did not affect the $\text{Fe}^{3+}/\text{Fe}^{2+}$ ratio, which was observed in chromium doping during activation. Other dopants incorporated in varying ways into the magnetite structure. Segregated M-Fe-oxide and M-oxide phases were observed in addition to magnetite in case of niobium and indium.

Combining the results of chapter 2-4, four generalisations (copied from chapter 4) can be made about the rational design of chromium-free iron-based water-gas shift catalysts:

- (1) The incorporation of trivalent ions of similar size to octahedral trivalent iron, such as aluminium, chromium, and gallium into the magnetite structure results in high to moderate CO conversion, irrespective of dopant incorporation in tetrahedral or octahedral positions. Aluminium doping leads to comparable activity and stability as chromium doping in a four-day test under HTS conditions at 25 bar.
- (2) Large trivalent ions, such as indium, do not remain in the iron oxide structure upon reduction of the Fe^{3+} -oxide precursor to magnetite, resulting in segregated promoter oxide phases. Elements that can form separate iron-M-oxide phases under reducing conditions, such as niobium, are also unsuited to replace chromium in HTS catalysts.
- (3) The incorporation of divalent ions with a tetrahedral site preference, such as zinc, results in complex structures where the charge imbalance is compensated by partial oxidation of Fe^{2+} in octahedral sites. No beneficial effect on CO conversion was observed for the Zn-promoted catalysts.

- (4) The incorporation of divalent ions with an octahedral site preference, such as Mn^{2+} , leads to a distortion of the octahedral $\text{Fe}^{3+}/\text{Fe}^{2+}$ redox couple because of the replacement of Fe^{2+} by Mn^{2+} . Unlike substitution with trivalent ions with an octahedral site preference, Mn^{2+} substitution has a detrimental effect on HTS catalytic activity.

The aluminium/copper-doped catalyst showed a similar performance to a chromium/copper-doped catalyst due to stabilisation of the surface area. The second major deactivation mechanism of iron-based water-gas shift catalysts, i.e. over-reduction, was investigated in **chapter 5** for the promising aluminium/copper-doped catalyst. The reducibility of metal oxides is typically investigated by TPR techniques. Over-reduction in industrially relevant HTS conditions is a delicate balance between reducing (H_2 , CO) and oxidising (H_2O , CO_2) gasses often expressed as *R*-factor ($R = [\text{CO}] \cdot [\text{H}_2] / [\text{CO}_2] \cdot [\text{H}_2\text{O}]$). Therefore, the influence of chromium and aluminium doping on iron-oxide based water-gas shift catalysts was for the first time investigated using *in situ* Mössbauer spectroscopy. Catalysts were exposed to an industrially relevant ageing protocol, where the *R*-factor was increased by gradually replacing steam by He. It was shown that in a non-doped iron-oxide catalyst, α -Fe and cementite formation occurred at $R = 2.09$. In the chromium doped reference catalyst, over-reduction was observed at $R = 6.57$ confirming the stabilizing effect of chromium on the active magnetite structure. The presence of copper in a chromium/copper co-doped catalyst slightly enhanced the reducibility of the active magnetite phase to an *R* factor of 2.88. It should be noted here that *R*-factors do not scale linear with steam concentration and that $R = 2.88$ is only 6% higher in steam than $R = 6.57$. An aluminium-doped catalyst showed over-reduction of magnetite to α -Fe at $R = 1.64$ while cementite was observed at $R = 2.09$. The stabilisation of α -Fe from carburisation was not observed in chromium-doped catalysts. This effect was not observed in the aluminium/copper co-doped catalyst where cementite formation occurred at $R = 2.09$, which is the same as in a non-doped catalyst. The enhanced reducibility of the aluminium-doped catalyst occurs below industrially relevant HTS conditions at $R = 1.48$ (27% steam) compared to typical industrial operating conditions of 33% H_2O . It was shown in chapter 4 that the aluminium/copper-doped catalysts are stable for 4 days under industrially relevant HTS conditions at 25 bar. Enhanced reducibility, observed only in the aluminium-doped catalyst, is highly undesirable for long term operation.

Because of the promising stability of the aluminium- and aluminium/copper-doped catalysts in chapter 4, the unexpected difference between the reducibility of aluminium-doped and an aluminium/copper-doped catalyst deserves further research into these structures. It was proposed in literature that aluminium doping can result in the formation of separate aluminium-oxide phases, although no evidence of alumina was found in XRD patterns. The absence of XRD reflections however does not exclude the possibility of small crystallite or amorphous aluminium-oxide phases. Furthermore, it is known that the precipitation pH has a significant influence on the catalyst structure. The precipitation pH of 11, used in this thesis, was chosen based on earlier optimisation of the synthesis of chromium-doped catalysts. This could be optimised with respect to the use of aluminium instead of chromium, because the amphoteric aluminium dopant can leach from the catalyst precursor during ageing at elevated pH. After establishing an optimum co-precipitation/calcination route, the doping level of aluminium can be further optimised for which hardly any data are currently available in literature. Finally, a long-term *in situ* Mössbauer spectroscopy study of the optimised aluminium/copper-doped catalyst can be performed. Mössbauer spectra can be recorded at regular intervals to study the structure of aluminium/copper-doped catalysts under industrially relevant conditions without exposing the catalyst to air.

SAMENVATTING EN VOORUITZICHTEN

Waterstofgas is een essentieel reagens in vele industriële processen waaronder ammonia synthese. Ammonia is een belangrijk tussenproduct in de synthese van stikstofhoudende kunstmest als nitraten en ureum. Volgens recente schattingen (2008) zijn gesynthetiseerde stikstofhoudende kunstmest verantwoordelijk voor het voeden van ongeveer de helft van de wereldbevolking. Statistisch gezien dankt dus de helft van iedereen die deze zin leest zijn bestaan aan ammonia synthese. Tegenwoordig vind het overgrote deel van het gesynthetiseerde waterstofgas zijn oorsprong in methaan, dat via stoomreforming gevolgd door een twee-stap water-gas shift reactie omgezet wordt in waterstofgas. De hoge temperatuur water-gas shift reactie (HTS) maakt gebruik van een met chroom en koper gedoteerde ijzeroxide katalysator. Chroom wordt toegevoegd om de actieve ijzeroxide fase magnetiet (Fe_3O_4) te beschermen tegen sinteren en over-reductie naar $\alpha\text{-Fe}$ en Fe -carbiden. Koper wordt toegevoegd om de activiteit te vergroten doormiddel van het leveren van extra actieve sites. De chroom stabilisator wordt al meer dan een eeuw gebruikt vanwege zijn lage kosten en omdat deze uitstekende stabiliteit brengt. Chroom wordt toegevoegd aan de voorganger van de actieve katalysator via een co-precipitatie/calcinerings route. Een onopzettelijke bijkomstigheid van calcineren is dat een deel van het chroom kan oxideren naar chroom-6. Voor het werken met chroom-6 gelden strenge voorwaarden en het is in bepaalde sectoren al volledig uitgefaseerd. De actieve magnetiet fase is een inverse spinelstructuur bestaande uit een 1:1:1 verhouding van; tetraëdrisch Fe^{3+} , octaëdrisch Fe^{3+} en octaëdrisch Fe^{2+} , hetgeen resulteert in een octaëdrisch $\text{Fe}^{3+}/\text{Fe}^{2+}$ redox koppel. De actieve sites van de magnetiet katalysator zijn de octaëdrisch $\text{Fe}^{3+}/\text{Fe}^{2+}$ redox koppel sites aan het oppervlak van de bulk katalysator. Het ontwerpen van een katalysator met een alternatief doteermiddel voor chroom wordt ernstig belemmert door de beperkte kennis over chroom dotering in de inverse spinelstructuur van magnetiet. Zodoende is de positie van chroom en zijn effect op de magnetietstructuur en zijn $\text{Fe}^{3+}/\text{Fe}^{2+}$ redox koppel zorgvuldig in kaart gebracht.

In **hoofdstuk 2** is een serie chroom gedoteerde ijzeroxide katalysatoren gesynthetiseerd via een co-precipitatie/calcinerings route. De vers gecalceerde katalysatoren bestonden uit chroom gedoteerd hematiet ($\alpha\text{-Fe}_{2-x}\text{Cr}_x\text{O}_3$). De reductie van de hematiet voorganger, en de over-reductie van de actieve magnetietkatalysator naar $\alpha\text{-Fe}$ vinden bij hogere temperaturen plaats in de chroom gedoteerde katalysatoren. Chroom is opgenomen in de magnetiet

structuur na blootstelling van de gecalcineerde katalysator aan industrieel relevante water-gas shift condities. De aanwezigheid van chroom resulteerde in verhoogde CO conversie onafhankelijk van de reactie druk (2 of 25 bar). Röntgendiffractiepatronen toonden dat chroom dotering resulteerde in kleinere kristalietgroottes, wat de rol van chroom als structurele stabilisator bevestigde. Uit Mössbauer spectra bleek dat chroom in de octaëdrische posities van magnetiet was ingelijfd. De inlijving van chroom voorkwam deels de reductie van Fe^{3+} tijdens de formatie van magnetiet, met als resultaat een hogere $\text{Fe}^{3+}/\text{Fe}^{2+}$ ratio in de inverse spinel structuur. Deze variaties in de $\text{Fe}^{3+}/\text{Fe}^{2+}$ ratio in vergelijking met stoichiometrisch magnetiet hadden geen meetbaar effect op de hoge CO conversie waar chroom dotering doorgaans mee geassocieerd wordt. De interpretatie van de Mössbauer data werd ondersteund door uit DFT berekeningen verkregen hyperfijn parameters van verschillende chroom en Fe-vacature gedoteerde magnetiet structuren. Uit deze resultaten bleek dat de actieve magnetiet fase onder industrieel relevante water-gas shift condities het best omschreven kan worden als $\text{Fe}_{3-x(1-\delta)}\text{Cr}_x\text{O}_4$. In de $\text{Fe}_{3-x(1-\delta)}\text{Cr}_x\text{O}_4$ structuur is Cr^{3+} ingelijfd in octaëdrische posities waar zijn aanwezigheid tijdens de vorming van de actieve fase door partiele reductie van $\alpha\text{-Fe}_{2-x}\text{Cr}_x\text{O}_3$ de vorming van Fe^{2+} hindert. De $\text{Fe}_{3-x(1-\delta)}\text{Cr}_x\text{O}_4$ structuur is deels geoxideerd in vergelijking met stoichiometrisch magnetiet waar de ratio octaëdrische $\text{Fe}^{3+}/\text{Fe}^{2+}$ ratio gelijk is aan 1:1. Met de exacte positie van chroom in de magnetiet structuur voorhanden is de positie van koper vervolgens onderzocht, omdat ook dit een gangbaar doteermiddel is voor HTS katalysatoren.

In **hoofdstuk 3** is een serie chroom/koper gedoteerde katalysatoren gesynthetiseerd via een co-precipitatie/calcinerings route, en onderzocht om inzicht te krijgen in de positie van koper in de $\text{Fe}_{3-x(1-\delta)}\text{Cr}_x\text{O}_4$ katalysator. In tegenstelling tot de gecalcineerde chroom gedoteerde ijzeroxide katalysatoren, die uit een hematiet fase bestonden, bestonden de chroom/koper gedoteerde katalysatoren uit een mengsel van hematiet en ferrihydriet. Uit Mössbauer spectra bleek dat koper de vorming van hematiet belemmerde tijdens het calcineren sinds de hoeveelheid ferrihydriet toenam met toenemend kopergehalte. De hematiet en ferrihydriet voorgangers converteerden volledig naar magnetiet onder industrieel relevante water-gas shift condities bij 2 en 25 bar. Mössbauer spectra bevestigden de resultaten uit hoofdstuk 2 dat chroom een vaste oplossing met magnetiet vormt, resulterend in een deels geoxideerde magnetietstructuur ($\text{Fe}_{3-x(1-\delta)}\text{Cr}_x\text{O}_4$). De toevoeging van koper had

geen significante invloed op de hyperfijn parameters in Mössbauer spectra, wat erop wijst dat het waarschijnlijk niet in de bulk structuur is ingelijfd. NAP-XPS experimenten bewezen dat koper als metallisch koper bestaat op het oppervlak van de katalysator onder water-gas shift condities. *Ex situ* XPS experimenten van katalysatoren blootgesteld aan industrieel relevante water-gas shift condities lieten zien dat een katalysator blootgesteld aan 25 bar een meer Fe²⁺ achtig oppervlak heeft dan een katalysator blootgesteld aan 2 bar vanwege de meer reducerende natuur van het gasmengsel bij hoge druk. Er is geen drukeffect op de bulkstructuur ontdekt. In de chroom/koper gedoteerde katalysator stabiliseert chroom het grote oppervlak van de katalysator ongeacht de druk, hetgeen leidt tot hoge CO conversie. Koper dotering resulteert in hogere CO conversie ongeacht de druk via de vorming van additionele actieve sites.

Met een goed begrip van chroom en koper is een serie katalysatoren gesynthetiseerd met alternatieve doteermiddelen. Deze serie katalysatoren is onderzocht in **hoofdstuk 4**. M-gedoteerde en M/Cu-gedoteerde (M = Fe, Cr, Al, Ga, In, Mn, Zn, Nb) katalysatoren zijn gesynthetiseerd om het effect van alternatieve doteermiddelen op de actieve magnetiet katalysator te onderzoeken. De katalysatoren zijn gesynthetiseerd via een co-precipitatie/calcinering route en onderzocht met Mössbauer spectroscopie. Aluminium, gallium en indium zijn gekozen om het effect van de grootte van het (trivalente) doteermiddel te onderzoeken. Mangaan, zink en niobium zijn gekozen om het effect van verschillende oxidatietoestanden te onderzoeken. De gecalcineerde gallium gedoteerde katalysator bestond uit hematiet, net als de niet gedoteerde en chroom gedoteerde katalysatoren onderzocht in hoofdstuk 2. Gecalcineerde katalysatoren gedoteerd met aluminium, indium, mangaan, zink en niobium bestonden uit een mengsel van hematiet en ferrihydriet, de laatste in de vorm van relatief kleine kristallieten. Alle met koper gedoteerde katalysatoren bestonden voornamelijk uit ferrihydriet. Activiteitstesten onder industrieel relevante water-gas shift condities voor 4 dagen bij 25 bar bewezen dat aluminium de meest geschikte vervanger is voor chroom op basis van CO conversie. Wanneer de CO conversie van de M/Cu-gedoteerde katalysatoren vergeleken worden geeft aluminiumdotering een vergelijkbare katalytische activiteit als chroomdotering. De andere doteermiddelen resulteren in een significant lagere CO conversie na langdurig testen, afnemend in de volgorde gallium > indium > mangaan > zink > niobium. Mössbauer spectroscopie liet zien dat aluminium in zowel tetraëdrische als

octaëdrische posities van magnetiet is ingelijfd. Dit in contrast met chroom dat enkel in octaëdrische posities ingelijfd was. Aluminiumdotering had daarnaast geen effect op de $\text{Fe}^{3+}/\text{Fe}^{2+}$ ratio, hetgeen geobserveerd was voor chroomdotering tijdens activering. De resterende doteermiddelen waren op verschillende wijze ingelijfd in de magnetiet structuur. Gesegregeerde M-Fe-oxide en M-oxide fasen waren gevormd naast magnetiet in de niobium en indium gedoteerde katalysatoren.

Op basis van de resultaten uit hoofdstuk 2-4 kunnen er 4 generalisaties gemaakt worden over het ontwerp van chroomvrije op ijzer gebaseerde water-gas shift katalysatoren:

- (1) De inlijving van trivalente ionen van vergelijkbare grootte aan octaëdrisch trivalent ijzer, zoals aluminium, chroom en gallium, in de magnetietstructuur resulteert in hoge tot middelmatige CO conversie, onafhankelijk van de inlijving in tetraëdrische of octaëdrische posities. Aluminiumdotering leidt tot vergelijkbare activiteit en stabiliteit als chroomdotering in een vier dagen durende test onder HTS condities bij 25 bar.
- (2) Grote trivalente ionen als indium verlaten de ijzeroxide structuur tijdens reductie van de gecalcineerde Fe^{3+} -voorganger, wat resulteert in een gesegregeerde doteermiddeloxide fase. Elementen die een aparte ijzer-M-oxide fase kunnen vormen onder reducerende condities als niobium zijn ook ongeschikt om chroom te vervangen in HTS katalysatoren.
- (3) De inlijving van divalente ionen met een voorkeur voor tetraëdrische posities zoals zink resulteert in complexe structuren waar de lading disbalans gecompenseerd wordt door gedeeltelijke oxidatie van octaëdrisch Fe^{2+} . Er is geen gunstig effect van zinkdotering op CO conversie geobserveerd in de zink gedoteerde katalysatoren.
- (4) De inlijving van divalente ionen met een voorkeur voor octaëdrische posities zoals Mn^{2+} leidt tot een verstoring van de octaëdrische $\text{Fe}^{3+}/\text{Fe}^{2+}$ ratio vanwege de vervanging van Fe^{2+} door Mn^{2+} . In tegenstelling tot substitutie met trivalente ionen met een octaëdrische voorkeur heeft Mn^{2+} een nadelig effect op de katalytische activiteit.

De aluminium/koper gedoteerde katalysator had een vergelijkbare activiteit met een chroom/koper gedoteerde katalysator vanwege de stabilisatie van zijn grote oppervlak. Het tweede belangrijke deactiveringsmechanisme van op ijzer gebaseerde water-gas shift katalysatoren, over-reductie, was onderzocht in **hoofdstuk 5** voor de veelbelovende aluminium/koper gedoteerde katalysator. De reduceerbaarheid van metaaloxides wordt doorgaans onderzocht met TPR technieken. Over-reductie in onder industrieel relevante HTS condities is echter een delicate balans tussen reducerende (H_2 , CO) en oxiderende (H_2O , CO_2) gassen. Deze balans wordt doorgaans uitgedrukt als *R*-factor ($R = [CO] \cdot [H_2] / [CO_2] \cdot [H_2O]$). Derhalve is de invloed van chroom en aluminium dotering op ijzeroxide gebaseerde water-gas shift katalysatoren, voor het eerst, onderzocht met *in situ* Mössbauer spectroscopie. Katalysatoren zijn blootgesteld aan een industrieel relevant rijpingsprotocol, waar de *R*-factor stapsgewijs verhoogd werd door stoom te vervangen door He. In de niet gedoteerde ijzeroxidekatalysator werden α -Fe en cementiet vorming geobserveerd bij $R = 2.09$. In de met chroom gedoteerde referentiekatalysator vond over-reductie plaats bij $R = 6.57$, wat de stabiliserende rol van chroom in de actieve magnetietstructuur bevestigd. De aanwezigheid van koper in de chroom/koper gedoteerde katalysator deed de reduceerbaarheid van de actieve magnetiet fase iets toenemen naar een *R* waarde van 2.88. Het is belangrijk hier in acht te nemen dat de *R*-factor niet lineair schaalte met stoomconcentratie en dat een *R* factor van 2.88 maar een 6% hogere stoomconcentratie betreft dan een *R* factor van 6.57. De met aluminium gedoteerde katalysator liet over-reductie van magnetiet naar α -Fe zien bij $R = 1.64$ terwijl cementiet pas vormde bij $R = 2.09$. De stabilisering van α -Fe voor cementiet formatie wijkt af voor de met chroom gedoteerde katalysatoren. Dit effect was afwezig in de aluminium/koper gedoteerde katalysator waar cementietvorming geobserveerd werd bij $R = 2.09$, gelijk aan een niet gedoteerde katalysator. De toegenomen reduceerbaarheid van de aluminium gedoteerde katalysator vind plaats bij een lagere stoomconcentratie dan industrieel relevante HTS condities bij $R = 1.48$ (27% stoom) in vergelijking met gangbare industriële condities (33% stoom). In hoofdstuk 4 was bewezen dat een aluminium/koper gedoteerde katalysator stabiel was voor 4 dagen onder industriële HTS condities bij 25 bar. De toegenomen reduceerbaarheid geobserveerd in de aluminium gedoteerde katalysator is zeer onwenselijk voor lange termijn exploitatie. Desalniettemin is verder onderzoek naar deze katalysatoren wenselijk vanwege de veelbelovende stabiliteit van de aluminium en aluminium/koper gedoteerde katalysatoren beschreven in

hoofdstuk 4. In de vakliteratuur wordt geopperd dat aluminiumdotering kan leiden tot de vorming van losse aluminiumoxides, ondanks de afwezigheid van bewijs in röntgendiffractiepatronen. De afwezigheid van reflecties in röntgendiffractiepatronen sluit echter het bestaan van amorfe aluminiumoxide fasen of aluminiumoxides bestaande uit zeer kleine kristallieten niet uit. Daarnaast is het alom bekend dat de precipitatie pH een grote invloed heeft op de structuur van de katalysator. De precipitatie pH van 11, gekozen in deze thesis, was gebaseerd op eerdere optimalisaties van de synthese van met chroom gedoteerde katalysatoren. Dit zou verder geoptimaliseerd kunnen worden voor het gebruik van aluminium in plaats van chroom. Dit is nodig vanwege het amfotere karakter van aluminium, dat uitlogen tijdens de rijping van de katalysator bij pH 11 mogelijk kan maken. Na het vastleggen van een optimale co-precipitatie/calcinerings route voor aluminium gedoteerde katalysatoren, kan de mate van aluminiumdotering onderzocht worden waarover in de huidige vakliteratuur nauwelijks data bestaat. Tot slot kan er een lange termijn *in situ* Mössbauer spectroscopie studie van de geoptimaliseerde aluminium/koper gedoteerde katalysator uitgevoerd worden. Mössbauer spectra kunnen opgenomen worden op regelmatige intervallen om zo de structuur van de aluminium/koper gedoteerde katalysator te onderzoeken onder industrieel relevante condities zonder deze aan de atmosfeer bloot te stellen.

ACKNOWLEDGEMENTS

The job is done and I am proud of it. Scientific research is not without difficulties and so is writing (especially when combined with a fulltime job). Nevertheless, I can say that it is one of the most fulfilling things one can undertake. In the past years I have grown significantly as a scientist and as a person. As the saying goes: diamonds are formed under pressure. In the following pages I would like to express my gratitude to everyone who has contributed to this thesis over the past years and helped to make this project happen.

First and foremost I would like to express my gratitude to my promoters and copromotor for giving me the opportunity to work on this project and helping developing myself as a scientist. Emiel, bedankt voor je adviezen en inzichten tijdens meetings en de (vele) comments tijdens het schrijfproces. De laatste loodjes wegen het zwaarst en ik ben je zeer dankbaar voor al je hulp bij het afronden. Het is indrukwekkend om te zien hoe je zo een grote onderzoeksgroep leidt en toch altijd exact op de hoogte bent van waar iedereen mee bezig is. Ekkes, dankjewel voor alle comments en begeleiding door de jaren heen. Ook bedankt voor je interesse in katalysatoren, ondanks dat het geen magnetocalorische materialen zijn had je altijd interesse in wat ik te vertellen had. Iulian, you have granted me almost complete freedom in conducting my research which I appreciate a lot. Your comments and advice over the past years have helped me significantly in taking the most effective route towards my goals. Thank you for introducing me to Mössbauer spectroscopy, it is a true form of art and I will propagate it as such during the rest of my career!

Leon, jouw naam kan ook zeker niet ontbreken als het op supervisie aankomt. Bedankt voor alle hulp tijdens mijn bezoeken aan Johnson Matthey (JM) in Billingham, en ook alle begeleiding en comments tussendoor. Je hebt me veel geleerd over katalysatoren en misschien nog wel belangrijker het gebruik van industriële tegenover “academische” condities. Daarnaast waardeer ik het enorm dat ik altijd met open armen ontvangen ben in Billingham, tijdens werktijd en ook in de weekenden. I would also like to express my gratitude to all other colleagues from JM who helped me either during the visits or gave their advice via online meetings. Tugce, thanks for showing me the ropes on NAP-XPS during our visit to the synchrotron in Berlin and the useful

discussions later on. It was a fun experience working almost one hundred hours in a single week surviving solely on bulgur salad and energy drinks. Liliana, thanks for the advice you gave on XPS and the helpful comments during meetings and teams calls. Deborah, thank you for teaching me about large scale catalyst preparation. Zina, thanks for the helpful discussions overall. Alkis and Tom, although we did not really work together I really enjoyed going to the pub on the weekends.

I would also like to express my gratitude to Vojtech and Pavel, without whom the computational modelling in chapter 2 would not have been possible. Vojtech, it was a lot of fun visiting Prague and learning about modelling. You are a very modest person for someone that knows so much!

I would also like to thank my colleagues from the reactor institute Delft and IMC at TU Eindhoven for the good times on the lab. Prasad, I admire your perseverance in the writing process. Luke, het is indrukwekkend om te zien dat er mensen zijn die chemische reacties met radioactieve materialen uit durven te voeren. Carlo, it was a lot of fun showing you the ropes on the lab, especially the “religious” aspects of MB15. Jouke, bedankt voor alle hulp bij het in gebruik nemen van de Wien2k software, ik zal nooit meer normaal naar een muffin tin kunnen kijken. Giulia en Wilbert, ik ben jullie eeuwig dankbaar voor alle hulp tijdens het begin van mijn PhD. Het was fijn om als externe met open armen ontvangen te worden bij IMC. Ik zal nooit vergeten dat met stoom werken vooral op papier goed te doen is. Arno, bedankt voor het tolereren van de ladingen TEM samples die ik af en toe in Eindhoven langs kwam brengen. Valery, thanks for the help with the NAP-XPS measurements and the useful discussions on data interpretation. Freddy, I would also like to thank you for all the help in XPS and data interpretation. Wei and Jiachun, thanks for helping with the TPR setup. And Sasha for the thermodynamic modelling. Maarten, Giacomo, Hanan, Remco, Beien, en Evert, het was een mooie ervaring om met jullie in de PhD commissie te zitten. Ik hoop dat toekomstige generaties het stokje over nemen en de pizza er in houden! Maarten het was altijd lachen om samen de pub-quiz voor het reactor instituut te organiseren, zoals je al zei: we zouden een bv kunnen beginnen. I would also like to thank all of my office mates for all the good times. Casper, Fengjiao, Geert, Fenqi, Ivan, Qi, and all others who I have shared the guest office with in Eindhoven.

Er is geen wetenschap mogelijk zonder goede technici. Het zou een mooie stelling zijn geweest. Michel je hebt me de afgelopen jaren veel praktische kennis bijgebracht en je was altijd beschikbaar voor hulp op het lab. Ik kan me nog goed herinneren dat ik voor het eerst met zweet op mijn voorhoofd een radioactieve bron aan het vervangen was en via een spiegel achter een door jouw gebouwde loodmuur aan het werk was. Ook Kees wil ik graag bedanken voor alle hulp en advies omtrent röntgendiffractie. Frans, bedankt voor het tolereren van de grote hoeveelheid samples die ik in de glovebox bewaarde. Ook zou ik Tiny en Johan willen bedanken voor de hulp op het lab in Eindhoven. Naast goede technici kan een universiteit ook niet functioneren zonder logistieke ondersteuning. Isle en Nicole, bedankt voor alle hulp door de jaren heen. Ook Emma bedankt voor alle ondersteuning en de leuke praatjes tussendoor, wanneer ik van het kastje naar de muur gestuurd werd was een belletje van jou naar de verantwoordelijke voldoende om het geregeld te krijgen.

Ook zou ik iedereen van DEMO graag willen bedanken voor de hulp bij het vervaardigen van de *in situ* Mössbauer cell. Het ging niet zonder slag of stoot maar uiteindelijk heeft het mooie resultaten opgeleverd. Ernst bedankt voor de hulp bij het organiseren van de aanpassingen die nodig waren. William, ik ben je zeer dankbaar voor het maken van de benodigde aanpassingen aan de cell en de reparaties tussendoor, zonder jou was hoofdstuk 5 een stuk korter geweest! Ook Jeroen zou ik graag willen bedanken voor het vervaardigen van de cell.

Ook zou ik mijn vrienden en familie graag willen bedanken voor alle mooie weekenden en avonden die de nodige ontspanning in het leven brengen.

Arie, Jelle, en Huib, het was me een waar genoegen om met jullie in Crooswijk te wonen tijdens een groot deel van mijn promotietraject. We waren toch de enige yuppen die tot op zekere hoogte geaccepteerd werden door de locals. Ik zou zo een aantal pagina's aan nostalgie kunnen vullen over onze tijd daar maar dat zijn meer verhalen voor tijdens het promotiefeest.

Ook de avonden met oud studiegenoten van de VU en de UVA blijven mooi. Pim, Thomas, Jordy, John, Sjaak en iedereen van de SyBorCh groep die ik nog af en toe op conferenties tref, het blijft toch altijd als vanouds ondanks dat we inmiddels door het hele land verspreid wonen.

Rick, we kennen elkaar nu al sinds de brugklas en ik kan me niet anders voorstellen dan dat we ooit ergens in een bejaardenhuis naast elkaar gezet worden. Arie, het is altijd lachen om met je op avontuur te gaan of het nou naar de Brouwmarkt is of zonder enige voorbereiding richting zuid Frankrijk rijden. De weekendjes Antwerpen met zijn drieën blijven legendarisch.

Robin, het is altijd een feest om oude Scifi series voor de 10^e keer terug te kijken. Ade, we hebben altijd goede gesprekken samen en een avondje hangen eindigt steevast in een weekendje. Dario en Niels, we hebben mooie reizen gemaakt van Japan tot aan Normandië, laten we het erin houden nu het weer kan. Sebastiaan, het was een mooie tijd om een zomer lang bij jou en Ade te logeren. Ook waardeer ik de etentjes met zijn allen zeer.

Raoul, we maken mooie reizen samen en dat houd ik er graag in! We hebben dezelfde interesses als het op reizen aankomt en ook exact dezelfde concentratiespan tijdens een rondleiding door het Colosseum. Guido, het zijn altijd leuke avonden uit met de neven. Het is een goede ontwikkeling dat je richting Rotterdam bent verhuisd, nu moeten we alleen de rest van de familie nog overhalen.

Arthur, we hebben altijd een hoop lol samen. Je bent er eigenlijk bij alle bovenstaande gelegenheden zo ongeveer wel bij en ik vind het mooi dat we zoveel vrienden delen. Ook de borrelavonden met Rick, Ade, en Daan zijn altijd mooi. Ayten, bedankt voor al je kalmte en rust tijdens het afronden van mijn thesis, nu ben ik in ieder geval weer beschikbaar in de avonden en weekenden. Als laatst wil ik mijn ouders graag bedanken voor alle steun tijdens mijn studie scheikunde tot en met het behalen van mijn doctoraat.

Allen bedankt!

Maxim

LIST OF PUBLICATIONS

Within the scope of this thesis

M.I. Ariëns, L.G.A. van de Water, A.I. Dugulan, E. Brück, E.J.M. Hensen, Substituting Chromium in Iron-Based Catalysts for the High-Temperature Water–Gas Shift Reaction, *ACS Catalysis*, **2022**, 12, 22, 13838-13852.

M.I. Ariëns, L.G.A. van de Water, A.I. Dugulan, E. Brück, E.J.M. Hensen, Copper promotion of chromium-doped iron oxide water-gas shift catalysts under industrially relevant conditions, *Journal of Catalysis*, **2022**, 405, 391-403.

M.I. Ariëns, V. Chlan, P. Novák, L.G.A. van de Water, A.I. Dugulan, E. Brück, E.J.M. Hensen, The role of chromium in iron-based high-temperature water-gas shift catalysts under industrial conditions, *Applied Catalysis B: Environmental*, **2021**, 297, 120465.

Outside the scope of this thesis

J. Braun, M.I. Ariëns, B.T. Matsuo, S. de Vries, E.D.H. van Wordragen, B.D. Ellenbroek, C.M.L. van de Velde, R.V.A. Orru, and E. Ruijter, Stereoselective Synthesis of Fused Vinylcyclopropanes by Intramolecular Tsuji–Trost Cascade Cyclization. *Organic Letters*, **2018**, 20, 21, 6611-6615.

S.A.W. Hollak, M.I. Ariëns, K.P. de Jong, D.S. van Es, Hydrothermal Deoxygenation of Triglycerides over Pd/C aided by In Situ Hydrogen Production from Glycerol Reforming. *ChemSusChem*, **2014**, 7.5, 1057-1062.

Posters

M.I. Ariëns, E.J.M. Hensen, E. Brück, A.I. Dugulan, D. Dodds, L.G.A. van de Water, In-Situ Mössbauer spectroscopy study on the role of chromium and alternative dopants in iron based High-Temperature Water-Gas-Shift catalysts, *NCCC*, March 2020, **Noordwijkerhout, The Netherlands**.

M.I. Ariëns, E.J.M. Hensen, E. Brück, A.I. Dugulan, D. Dodds, L.G.A. van de Water, Towards the development of a chromium free high temperature water gas shift catalyst, *JMAC19*, April 2019, **Warwick, United Kingdom**.

M.I. Ariëns, E.J.M. Hensen, E. Brück, A.I. Dugulan, D. Dodds, L.G.A. van de Water, Towards the development of a chromium free high temperature water gas shift catalyst, *NCCC*, March 2019, **Noordwijkerhout, The Netherlands**.

M.I. Ariëns, E.J.M. Hensen, E. Brück, A.I. Dugulan, D. Dodds, L.G.A. van de Water, Investigating the role of chromium in the High Temperature Water Gas Shift Reaction, *JMAC18*, April 2018, **Loughborough, United Kingdom**.

M.I. Ariëns, E.J.M. Hensen, E. Brück, A.I. Dugulan, D. Dodds, L.G.A. van de Water, Understanding the role of chromium in industrial high temperature water-gas-shift catalysts, *JMAC17*, April 2017, **Loughborough, United Kingdom**.

Oral presentations

M.I. Ariëns, L.G.A. van de Water, A.I. Dugulan, E. Brück, E.J.M. Hensen, In-situ Mössbauer spectroscopy study on the high temperature water gas shift catalyst, *JMAC20*, June 2020, **Warwick, United Kingdom** (online).

M.I. Ariëns, L.G.A. van de Water, A.I. Dugulan, E. Brück, E.J.M. Hensen, Towards the development of a chromium free high temperature water gas shift catalyst, *ICAME 2019*, September 2019, **Dalian, China**.

M.I. Ariëns, L.G.A. van de Water, A.I. Dugulan, E. Brück, E.J.M. Hensen, Investigating the role of Chromium in the high temperature water gas shift catalyst, *NCCC*, March 2018, **Noordwijkerhout, The Netherlands**.

CURRICULUM VITAE

Maxim was born on the 10th of February 1989 in Utrecht, the Netherlands. He obtained his high school degree at the Leidsche Rijn College there. After a brief detour studying applied physics, he obtained his bachelor of applied sciences in chemistry from the HU University of Applied Sciences Utrecht in 2013. During this study he enrolled in two internships at the Wageningen University & Research centre motivating him to continue his studies. The study of chemistry continued in Amsterdam where he obtained his master's degree in 2016 at the Vrije Universiteit Amsterdam. In the same year he started his PhD research at Delft University of Technology in a collaboration with Eindhoven University of Technology and Johnson Matthey in the field of heterogeneous catalysis. The results of his research are summarized in this thesis. Since Januari 2021 he is employed as a scientist in the renewable energy sector.